

Spring 2001

# Generation of oxygen microbubbles in a microchannel with crosscurrent liquid flow

Sung Sam Kim  
*Louisiana Tech University*

Follow this and additional works at: <https://digitalcommons.latech.edu/dissertations>



Part of the [Biomedical Engineering and Bioengineering Commons](#)

---

## Recommended Citation

Kim, Sung Sam, "" (2001). *Dissertation*. 712.  
<https://digitalcommons.latech.edu/dissertations/712>

This Dissertation is brought to you for free and open access by the Graduate School at Louisiana Tech Digital Commons. It has been accepted for inclusion in Doctoral Dissertations by an authorized administrator of Louisiana Tech Digital Commons. For more information, please contact [digitalcommons@latech.edu](mailto:digitalcommons@latech.edu).

## INFORMATION TO USERS

This manuscript has been reproduced from the microfilm master. UMI films the text directly from the original or copy submitted. Thus, some thesis and dissertation copies are in typewriter face, while others may be from any type of computer printer.

**The quality of this reproduction is dependent upon the quality of the copy submitted.** Broken or indistinct print, colored or poor quality illustrations and photographs, print bleedthrough, substandard margins, and improper alignment can adversely affect reproduction.

In the unlikely event that the author did not send UMI a complete manuscript and there are missing pages, these will be noted. Also, if unauthorized copyright material had to be removed, a note will indicate the deletion.

Oversize materials (e.g., maps, drawings, charts) are reproduced by sectioning the original, beginning at the upper left-hand corner and continuing from left to right in equal sections with small overlaps.

Photographs included in the original manuscript have been reproduced xerographically in this copy. Higher quality 6" x 9" black and white photographic prints are available for any photographs or illustrations appearing in this copy for an additional charge. Contact UMI directly to order.

Bell & Howell Information and Learning  
300 North Zeeb Road, Ann Arbor, MI 48106-1346 USA  
800-521-0600

UMI<sup>®</sup>



**GENERATION OF OXYGEN MICROBUBBLES IN A  
MICROCHANNEL WITH CROSSCURRENT LIQUID FLOW**

by

**Sung Sam Kim, M.S.**

**A Dissertation Presented in Partial Fulfillment  
Of the Requirements for the Degree  
Doctor of Philosophy**

**COLLEGE OF ENGINEERING AND SCIENCE  
LOUISIANA TECH UNIVERSITY**

**May 2001**

UMI Number: 3003083

UMI<sup>®</sup>

---

UMI Microform 3003083

Copyright 2001 by Bell & Howell Information and Learning Company.

All rights reserved. This microform edition is protected against  
unauthorized copying under Title 17, United States Code.

---

Bell & Howell Information and Learning Company  
300 North Zeeb Road  
P.O. Box 1346  
Ann Arbor, MI 48106-1346

LOUISIANA TECH UNIVERSITY

THE GRADUATE SCHOOL

May 11, 2001

Date

We hereby recommend that the thesis prepared under our supervision  
by Sung Sam Kim

entitled Generation of Oxygen Microbubbles in a Microchannel with Crosscurrent  
Liquid Flow

be accepted in partial fulfillment of the requirements for the Degree of  
Doctor of Philosophy

Ryszard Schubert

Supervisor of Thesis Research

Stan Napper

Head of Department

Department

Recommendation concurred in:

M. J. G. G. G.  
G. G. G.

Stan Napper  
John Hill

Advisory Committee

Approved: [Signature]  
Director of Graduate Studies

Approved: [Signature]  
Dean of the Graduate School

[Signature]  
Dean of the College

## ABSTRACT

An alternative way of blood oxygenation is proposed by introducing small bubbles directly into the blood stream. To be used for blood oxygenation, the bubble should be small enough to pass through the capillary beds. To explore the feasibility of producing small bubbles, bubble formation phenomena in a crosscurrent liquid flow in a silicon microchannel were studied. Small orifices with 4  $\mu\text{m}$ , 4.2  $\mu\text{m}$ , and 6.6  $\mu\text{m}$  hydraulic diameter were machined in a direction perpendicular to a trapezoidal channel that has a hydraulic diameter of 42 micrometers. These orifices were connected to three different chambers of  $2.5 \times 10^{-7} \text{ cm}^3$ ,  $5 \times 10^{-7} \text{ cm}^3$ , and  $10 \times 10^{-7} \text{ cm}^3$  in volume. The glass plate was anodically bonded to the silicon. Water and oxygen were supplied to the channel and orifice through the chamber, respectively.

Between the liquid flow rate of 1 to 3 ml/hr and gas flow rate of 0.036 to 0.072 ml/hr very uniform bubbles, sizes of about 45 micrometer in diameter, were produced from the orifice with smallest chamber volume. In these ranges, the regression model shows that the bubble size has a weak relation to the gas and liquid flow rate. As the chamber volume gets bigger, the bubble sizes are increased and eventually become non-uniform.

From the experimental results, it is concluded that the chamber volume plays a significant role in determining bubble size. A mathematical model of appropriate

phenomena was validated by comparison to experimental data. The data and the validated model suggest a simpler design and model. This model, with no chamber volume suggests that the bubble size can be decreased further if the orifice and crosscurrent liquid flow channel diameter can be decreased without causing pressure increase in the channel. This model predicts it is possible to produce bubbles of 16 micrometer in diameter at a rate of about 10,000 Hertz.

## APPROVAL FOR SCHOLARLY DISSEMINATION

The author grants to the Prescott Memorial Library of Louisiana Tech University the right to reproduce, by appropriate methods, upon request, any or all portions of this Dissertation. It is understood that "proper request" consists of the agreement, on the part of the requesting party, that said reproduction is for his personal use and that subsequent reproduction will not occur without written approval of the author of this Dissertation. Further, any portions of the Dissertation used in books, papers, and other works must be appropriately referenced to this Dissertation.

Finally, the author of this Dissertation reserves the right to publish freely, in the literature, at any time, any or all portions of this Dissertation.

Author *Aermyan Ki*  
Date May 17, 2001

## TABLE OF CONTENTS

|   | Page |
|---|------|
| ABSTRACT .....  | iii  |
| LIST OF TABLES .....  | xi   |
| LIST OF FIGURES .....   | xii  |
| ACKNOWLEDGEMENTS .....  | xvi  |
| CHAPTER 1 – INTRODUCTION .....                                  | 1    |
| 1.1 The problem .....   | 1    |
| 1.2 The history .....   | 2    |
| 1.3 The hypothesis .....  | 4    |
| CHAPTER 2 – LITERATURE REVIEW .....                             | 5    |
| 2.1 Mechanical ventilator .....                                 | 5    |
| 2.2 Oxygenator .....  | 5    |
| 2.2.1 Bubble oxygenator .....                                   | 6    |
| 2.2.2 Film oxygenator .....                                     | 6    |
| 2.2.3 Membrane oxygenator .....                                 | 7    |
| 2.2.4 Intravascular oxygenator (IVOX) .....                     | 7    |
| 2.3 Bubble formation in quiescent liquid .....                  | 8    |
| 2.3.1 Bubble formation under constant flow conditions .....     | 10   |
| 2.3.2 Bubble formation under constant pressure conditions ..... | 15   |

|  |               |
|--|---------------|
| 2.3.3 Bubble formation under variable chamber pressure ..... | 16            |
| 2.4 Bubble formation in flowing liquid .....                 | 24            |
| 2.4.1 Cocurrent flow .....                                   | 24            |
| 2.4.2 Crosscurrent flow .....                                | 26            |
| <br><b>CHAPTER 3 – MATHEMATICAL MODELING OF</b>              |               |
| <b>BUBBLE FORMATION IN MICROCHANNELS .....</b>               | <b>33</b>     |
| 3.1 The growth model and assumptions .....                   | 33            |
| 3.2 Pressure inside the chamber .....                        | 34            |
| 3.3 Gas flow through orifice .....                           | 36            |
| 3.4 Bubble growth .....                                      | 37            |
| 3.5 Pressure at the bubble surface .....                     | 39            |
| 3.6 Pressure in the crosscurrent liquid flowing channel..... | 43            |
| 3.7 Bubble detachment .....                                  | 44            |
| 3.8 Bubble generation modeling .....                         | 46            |
| 3.9 Modified model of bubble detachment condition .....      | 49            |
| 3.10 New model of bubble detachment condition .....          | 50            |
| <br><b>CHAPTER 4 – EXPERIMENTAL APPARATUS .....</b>          | <br><b>52</b> |
| 4.1 Apparatus design .....                                   | 52            |
| 4.2 Microchannel fabrication .....                           | 53            |
| 4.2.1 Mask generation .....                                  | 54            |
| 4.2.2 Resist .....   | 55            |
| 4.2.3 Mask exposure and printing .....                       | 55            |
| 4.2.4 Developing .....                                       | 56            |

|  |    |
|--|----|
| 4.2.5 Etching oxide layer .....  | 56 |
| 4.2.6 Photoresist removal .....  | 56 |
| 4.2.7 Si etching .....   | 57 |
| 4.2.8 Removal of oxide layer .....                                       | 58 |
| 4.2.9 Orifice .....  | 58 |
| 4.2.10 Glass cover .....   | 59 |
| 4.3 Anodic bonding .....   | 59 |
| 4.3.1 Cleaning .....   | 60 |
| 4.3.2 Mate .....   | 60 |
| 4.3.3 Bonding .....  | 60 |
| 4.3.4 Examination of bonding.....  | 61 |
| 4.4 Liquid flow in the channel .....                                     | 62 |
| 4.5 Photograph and measurement system .....                              | 62 |
| 4.6 Liquid channel modification .....                                    | 63 |
| CHAPTER 5 – RESULTS .....  | 65 |
| 5.1 General description of bubble formation .....                        | 65 |
| 5.2 Bubble size measurements .....                                       | 71 |
| 5.3 Comparison of experimental data with theoretical model .....         | 80 |
| 5.3.1 Original prediction model for experimental bubble production ..... | 83 |
| 5.3.2 Modified prediction model .....                                    | 87 |
| 5.3.3 Gas momentum change .....  | 91 |
| CHAPTER 6 – DISCUSSION .....   | 95 |
| 6.1 Design .....   | 95 |

|   |     |
|---|-----|
| 6.2 Measurements .....  | 96  |
| 6.3 Model .....   | 96  |
| 6.4 Validation of model trend .....                             | 97  |
| 6.4.1 Orifice diameter .....                                    | 97  |
| 6.4.2 Gas flow rate .....                                       | 97  |
| 6.4.3 Chamber volume .....                                      | 98  |
| 6.4.4 Velocity of cross-flowing liquid .....                    | 99  |
| 6.4.5 Discharge coefficient .....                               | 101 |
| 6.5 Suggested model for further reduction in bubble size .....  | 102 |
| 6.5.1 New model .....   | 102 |
| 6.5.2 New model predictions .....                               | 103 |
| 6.5.3 A practical device .....                                  | 105 |
| CHAPTER 7 CONCLUSIONS AND RECOMMENDATIONS .....                 | 106 |
| APPENDIX A – PRESSURE FLUCTUATION IN THE CHAMBER .....          | 108 |
| APPENDIX B – EQUATION FOR BUBBLE GROWTH .....                   | 111 |
| APPENDIX C – SIMULINK PROGRAM FOR ORIGINAL MODEL .....          | 114 |
| 1 Simulink program for prediction model .....                   | 115 |
| 2 Simulink program for equation 1 in prediction model .....     | 116 |
| 3 Simulink program for equation 2 in prediction model .....     | 116 |
| 4 Simulink program for equation 3 in prediction model .....     | 117 |
| 5 Simulink program for equation 4 in prediction model .....     | 118 |
| 6 Simulink program for inertia force in prediction model .....  | 119 |
| 7 Simulink program for momentum force in prediction model ..... | 119 |

|   |     |
|---|-----|
| 8 Simulink program for drag force in prediction model ..... | 119 |
| APPENDIX D – SIMULINK PROGRAM FOR MODIFIED MODEL .....      | 120 |
| APPENDIX E – SIMULINK PROGRAM FOR NEW MODEL .....           | 122 |
| APPENDIX F – NOMENCLATURE .....                             | 124 |
| BIBLIOGRAPHY .....  | 129 |

## LIST OF TABLES

|   |     |
|---|-----|
| Table 4.1 Dimensions of chambers and orifices used in experiments<br>for microbubble production .....   | 64  |
| Table 5.1 Bubble size measurements with apparatus 1A for<br>different liquid and gas flow rates<br>( $2.5 \times 10^{-7} \mu m^3$ of chamber volume ) ..... | 71  |
| Table 5.2 Bubble size measurements with apparatus 2A for<br>different liquid and gas flow rates<br>( $2.5 \times 10^{-7} \mu m^3$ of chamber volume ) ..... | 72  |
| Table 5.3 Bubble size measurements with apparatus 2B for<br>different liquid and gas flow rates<br>( $5 \times 10^{-7} \mu m^3$ of chamber volume ) .....   | 73  |
| Table 5.4 Bubble size measurements with apparatus 2C for<br>Different liquid and gas flow rates<br>( $10 \times 10^{-7} \mu m^3$ of chamber volume ) .....  | 76  |
| Table 5.5 The sensitivity of bubble diameter to chamber volume, orifice diameter,<br>liquid flow rate, and gas flow rate to the, based on regression .....  | 75  |
| Table 5.6 Additional chamber pressures required with different gas flow rates .....   | 81  |
| Table 6.1 Sensitivity of bubble diameter to the parameters<br>in prediction model without chamber .....   | 104 |

## LIST OF FIGURES

|  | Page |
|--|------|
| Figure 2.1 Bubble formation conditions:<br>(a) constant flow, (b) constant pressure, and (c) intermediate condition  | 9    |
| Figure 2.2 Mechanism of bubble formation<br>(Adapted from Ramakrishnan et al., 1969)   | 11   |
| Figure 2.3 Pressure variation in the chamber (adapted from Park, 1977)<br>$V_c=11.7\text{ cm}^3$ , $D_i=0.12\text{ cm}$ , $V_b=0.05\text{ cm}^3$ (radius = 0.23 cm)  | 17   |
| Figure 2.4 Bubble formation in the intermediate condition<br>(adapted from Park, 1977)   | 17   |
| Figure 2.5 Theoretical curves for bubble volume ( $\text{cm}^3$ ), instantaneous flow rate, $\dot{V}$ ( $\text{cm}^3/\text{sec}$ ), and liquid inertia for the case of orifice diameter=0.167cm, $P=877$ ( $\text{gm}/\text{cm sec}^2$ ), $h=10$ (cm) (adapted from La Nauze and Harris, 1972) | 22   |
| Figure 2.6 Theoretical curves for radius with time for orifice radius of 0.167 cm<br>(modified from La Nauze and Harris, 1972)   | 23   |
| Figure 2.7 Model of bubble formation in a flowing fluid<br>(modified from Kawase, 1981)  | 28   |
| Figure 3.1 Bubble formation diagram  | 34   |
| Figure 3.2 Schematic of bubble growth in uniform flow  | 39   |
| Figure 3.3 Schematic diagram of forces acting on a bubble  | 45   |
| Figure 4.1 Schematic diagram of the microchannel device and identification<br>of bubble formation and observation sites  | 53   |
| Figure 4.2 Alignment of patterns   | 54   |
| Figure 4.3 Cross sectional dimension of the etched trench (units in $\mu\text{m}$ )  | 58   |

|  |    |
|--|----|
| Figure 4.4 Scanning electromicroscopy picture of orifice with 5 $\mu m$ width and 4.5 $\mu m$ depth which is micromachined by Focused Ion Beam (950X magnification) .....  | 59 |
| Figure 4.5 Apparatus used for anodic bonding .....   | 61 |
| Figure 4.6 Experimental set up for bubble formation and imaging system .....   | 63 |
| Figure 5.1 (a) Bubble formation at two different gas flow rates with $2.5 \times 10^{-7} cm^3$ of chamber volume. $Q_i = 10 \times 10^{-5} cm^3/sec$ , $Q_L = 1 ml/hr$ , and $D_o = 4.2 \mu m$ (bubble diameter = 45 $\mu m$ ) .....               | 67 |
| Figure 5.1 (b) Bubble formation at two different gas flow rates with $2.5 \times 10^{-7} cm^3$ of chamber volume. $Q_i = 1.5 \times 10^{-5} cm^3/sec$ , $Q_L = 1 ml/hr$ , and $D_o = 4.2 \mu m$ (bubble diameter = 43 $\mu m$ ) .....              | 67 |
| Figure 5.2 Bubble formation at $Q_i = 1.4 \times 10^{-5} cm^3/sec$ , $Q_L = 2 ml/hr$ , and $D_o = 4.2 \mu m$ with $2.5 \times 10^{-7} cm^3$ of chamber volume (bubble diameter = 43 $\mu m$ ) .....  | 68 |
| Figure 5.3 Bubble formation at $Q_i = 4 \times 10^{-5} cm^3/sec$ , $Q_L = 2 ml/hr$ , and $D_o = 4.2 \mu m$ with $2.5 \times 10^{-7} cm^3$ of chamber volume ( bubble diameter = 52, 42 $\mu m$ ) .....   | 68 |
| Figure 5.4 Bubble formation at $Q_i = 1.4 \times 10^{-5} cm^3/sec$ , $Q_L = 4 ml/hr$ , and $D_o = 4.2 \mu m$ with $2.5 \times 10^{-7} cm^3$ of chamber volume ( bubble diameter = 41 $\mu m$ + 30 $\mu m$ ) .....                                  | 69 |
| Figure 5.5 Bubble formation at $Q_i = 1.8 \times 10^{-5} cm^3/sec$ , $Q_L = 4 ml/hr$ , and $D_o = 4.2 \mu m$ with $2.5 \times 10^{-7} \mu m^3$ of chamber volume (bubble diameter = 58, 57.6, 58, 46, 46, 46, 45 $\mu m$ from left to right) ..... | 69 |
| Figure 5.6 Bubble formation at $Q_i = 2.5 \times 10^{-5} cm^3/sec$ , $Q_L = 1 ml/hr$ , $D_o = 4 \mu m$ , with $10 \times 10^{-7} \mu m^3$ of chamber volume ( bubble diameter = 67, 68, 68, 74, 68 $\mu m$ from the left to right ) .....          | 70 |
| Figure 5.7 Bubble formation at $Q_i = 2.4 \times 10^{-5} cm^3/sec$ , $Q_L = 3 ml/hr$ , $D_o = 4 \mu m$ , with $10 \times 10^{-7} \mu m^3$ of chamber volume ( bubble diameter = 36 + 66 $\mu m$ ) .....  | 70 |

|   |    |
|---|----|
| Figure 5.8 Residual plot of regression model .....  | 74 |
| Figure 5.9 Bubble diameter generated from apparatus 1A in different<br>gas and liquid flow rate with multiple regression results .....  | 76 |
| Figure 5.10 Bubble diameter generated from apparatus 2A in different<br>gas and liquid flow rate with multiple regression results .....   | 77 |
| Figure 5.11 Bubble diameter generated from apparatus 2B in different<br>gas and liquid flow rate with multiple regression results .....   | 78 |
| Figure 5.12 Bubble diameter generated from apparatus 2C in different<br>gas and liquid flow rate with multiple regression results .....   | 79 |
| Figure 5.13 Bubble growth and force balance at the orifice of 4.2 $\mu m$ diameter with<br>$2.5 \times 10^{-7} cm^3$ of chamber volume, 0.5 ml/hr liquid flow<br>and $1 \times 10^{-5} ml / sec$ gas flow ..... | 82 |
| Figure 5.14 Comparison between the experimental data in Table 5.1 and<br>the original prediction model .....  | 83 |
| Figure 5.15 Comparison between the experimental data in Table 5.2 and<br>the original prediction model .....  | 84 |
| Figure 5.16 Comparison between the experimental data in Table 5.3 and<br>the original prediction model .....  | 85 |
| Figure 5.17 Comparison between the experimental data in Table 5.4 and<br>the original prediction model .....  | 86 |
| Figure 5.18 Comparison between the experimental data in Table 5.1 and<br>the modified prediction model .....  | 88 |
| Figure 5.19 Comparison between the experimental data in Table 5.2 and<br>the modified prediction model .....  | 89 |
| Figure 5.20 Comparison between the experimental data in Table 5.3 and<br>the modified prediction model .....  | 90 |
| Figure 5.21 Comparison between the experimental data in Table 5.4 and<br>the modified prediction model .....  | 91 |

|  |     |
|--|-----|
| Figure 5.22 Model prediction of gas momentum change at the orifice with different chamber volumes during bubble formation<br>(orifice diameter = $4.2 \mu m$ , chamber volume (a) = $2.5 \times 10^{-7} cm^3$ ,<br>(b) = $5 \times 10^{-7} cm^3$ , (c) = $10 \times 10^{-7} cm^3$ , and (d) = $20 \times 10^{-7} cm^3$ ,<br>gas flow rate into the chamber = $1 \times 10^{-5} ml / sec$ ) ..... | 92  |
| Figure 5.23 Changes in gas momentum at the orifice with different liquid flow rate across the orifice of $4.2 \mu m$ in diameter with the chamber volume of $2.5 \times 10^{-7} cm^3$ at three different gas flow rates .....  | 93  |
| Figure 5.24 Changes in gas momentum at the orifice of $4.2 \mu m$ in diameter with different gas flow rate into the chamber volume of $2.5 \times 10^{-7} cm^3$ at three different liquid flow rates across the orifice .....  | 94  |
| Figure 6.1 Change in maximum gas momentum with different liquid velocity (orifice of $4.2 \mu m$ in diameter and $2.5 \times 10^{-7} cm^3$ of chamber volume with discharge coefficient of 0.1) .....  | 101 |
| Figure 6.2 Bubble diameter change with different liquid velocities in channel from the $4.2 \mu m$ orifice with no chamber volume underneath .....   | 104 |

## ACKNOWLEDGMENTS

The success of my study is due to the help of many people. I would like to acknowledge my parents for their financial and spiritual support. I also would like to acknowledge my wife and children for their support and devotion.

Many thanks are due to my advisor, Dr. Roy Schubert, and my committee members, Dr. Stan Napper, Dr. Bruce Gale, Dr. Mike Vasile, and Dr. Steven Conrad for their continuous encouragement. The financial support from the department of biomedical engineering during my study is also greatly acknowledged.

# CHAPTER 1

## INTRODUCTION

### 1.1 The problem

Severe respiratory failure in most cases is due to acute lung injury and acute respiratory distress syndrome (ARDS). ARDS is a pulmonary edemic condition arising from a variety of different insults to the lung tissue, which affects approximately 150,000 people per year in the United States (Fazzalari et al., 1994).

During ARDS, lung volume first is reduced by the primary injury, increasing vascular permeability, filling the lung with plasma and cells, and consolidating and increasing lung weight by 1 or 2 kg (Zapol, 1992). For management of ARDS, partial or total mechanical ventilator and/or extracorporeal membrane oxygenation has been used. The positive airway pressures and volume excursions associated with mechanical ventilation can result in further damage to lung tissue, including barotrauma, volutrauma and parenchymal damage from the toxic levels of oxygen required for effective mechanical ventilation (Weinberger, 1992). The alternative use of an extracorporeal membrane oxygenator is complicated and expensive, requiring extensive blood contact with biomaterials in extracorporeal circuits, systemic anticoagulation, and labor-intensive patient monitoring.

Therefore, an artificial device for blood oxygenation characterized by small size,

low maintenance costs, and single use without any further lung injury is necessary. A separate carbon dioxide removal device is in development (Conrad, personal communication) and would be used in conjunction with an oxygenation device.

## 1.2 The history

The primary function of lung is gas exchange. When there is inadequate gas exchange, it requires hospitalization and may need a device for supplemental oxygenation of blood. There are four basic types of oxygenators which have been used to take the place of the lung: the bubble oxygenator, membrane oxygenator, rotating disc oxygenator, and membrane oxygenator (Guyton, 1991). Among these, the bubble oxygenator is the most commonly used device because of ease of production, handling, sterilization, and dependability (Bowley *et al.*, 1978). This device is capable of total extracorporeal support of oxygen and carbon dioxide exchange. However, it requires the large extracorporeal blood flow rate (2 - 4 Liter/minute) and systemic heparinization. The risks of this technique are thrombocytopenia, hemorrhage, and mechanical failure (Zapol, 1992).

Recently another type of blood oxygenator was introduced which uses intracorporeal hollow fiber membranes. This device is placed in the superior and inferior vena cava. Oxygenation and carbon dioxide exchange in the blood occur through the bundle of fiber membranes. It has been tested for the management of advanced respiratory failure (Conrad *et al.*, 1993). However, the low oxygen and carbon dioxide transfer rate of this device require the simultaneous use of a mechanical ventilator. Another problem is that the device may obstruct the vena cava, raising caval pressure and

increasing venous congestion of organs such as liver or kidney (Zapol, 1992).

An alternative method of blood oxygenation may be possible by introducing small oxygen bubbles directly into the blood stream with a separate carbon dioxide removal device. Reductions in mechanical ventilatory support are possible, allowing mechanical ventilation with a much lower risk for secondary pulmonary injury or elimination of mechanical ventilation. To be used for blood oxygenation, the bubble should not obstruct blood flow. Vasculature arrest occurs in arterioles when bubbles of 40  $\mu\text{m}$  in diameter (Gorman et al., 1986). Bubbles from 10 to 20  $\mu\text{m}$  in diameter are known to escape pulmonary filtration (Butler et al., 1988). Therefore, it is desirable to produce bubbles smaller than 20  $\mu\text{m}$  in diameter. Micropipettes with small tip diameters attached with syringes can produce microbubbles. Oxygen bubbles about 15  $\mu\text{m}$  in diameter were produced through 1.5  $\mu\text{m}$  diameter micropipette. However, the bubble productions have large variations in size and require a high impulse of oxygen pressure. Once produced, an oxygen microbubble with about 15  $\mu\text{m}$  in diameter dissolves into the saline solution within 15 seconds (Unkel, 1991). Therefore, it can be deduced that once the oxygen microbubbles with diameters less than 20  $\mu\text{m}$  are introduced directly into the blood stream, they would dissolve within a short time without disturbing blood flow. Blood would be able to be oxygenated if the bubbles are made in this size range and in enough quantity to supply the amount of oxygen required by the body.

Therefore, the principal objective of this study is to produce microbubbles 10 to 20  $\mu\text{m}$  in diameter continuously. The method to be studied in this dissertation has liquid flow introduced perpendicular to the gas flow to provide an additional detaching force for the bubble. Both the gas and the liquid are introduced into separate microchannels. Two

channels are combined into one in a perpendicular fashion to provide a crosscurrent liquid flow to the gas flow. The possibility and limitation of producing microbubble within a microchannel in continuous manner will be examined. Furthermore, the relationship between gas flow rate through the microchannel and the size of microbubble generated will be investigated. In addition, different rate of liquid flow will be introduced in the microchannel to find its role on bubble size and density.

### 1.3 The hypothesis

It is hypothesized that the size of the bubble will be affected by (1) the size of the orifice, (2) the space between orifice for gas outlet and the point of gas inlet from the channel, and (3) the drag caused by crosscurrent of flow of liquid. Therefore, the specific aims of this work are

- (1) Design and fabrication of a microchannel such that microbubbles can be produced
- (2) Measure bubble size produced by variations in design parameters
- (3) Develop a mathematical model of this experiment that predicts bubble size and frequency
- (4) Validate model trends using experimental data and estimate the effect of gas and liquid flow rates on bubble size from experimental data and model
- (5) Determine the effect of orifice diameter, chamber volume, and crosscurrent liquid flow rate on the bubble size
- (6) Use validated model to develop criteria for an implantable device and an extra corporal device.

## CHAPTER 2

### LITERATURE REVIEW

#### 2.1 Mechanical ventilator

The mechanical ventilator can sustain gas exchange in the lungs when the lungs are unable to perform their function. Oxygen is forced into the patient's lungs with positive gas pressure through the trachea. Carbon dioxide is exhaled when the pressure of the ventilator is relaxed. However, positive expiratory pressure used by the ventilation may produce further damage to the lung. The ideal condition for recovery from ARDS would be a near normal rate of oxygen and carbon dioxide gas concentration in the blood while the lungs are in a resting condition.

#### 2.2 Oxygenator

Artificial lung devices for oxygenation of blood outside of the body have been developed, and their primary application has been in cardiac surgery where it is advantageous to bypass blood not only around the heart but the lungs as well. Gas exchange in an artificial lung relies mainly on the creation of a large interfacial blood-gas contact area. This area can be generated by dispersing the gas phase as bubbles in a pool of blood, by spreading blood in a thin film on a stationary or moving solid plate, or screen, by dispersion of blood into a gas phase via foaming or spraying, by flowing blood

and gas on opposite side of a large semipermeable membrane. Blood side mixing, which promotes gas transfer, is achieved by various means: direct mechanical stirring, turbulent gas flow, or moving or rotating the solid surfaces on which the blood films are created.

### 2.2.1 Bubble oxygenator

Bubble oxygenators usually consist of a column where the oxygen gas is mixed with venous blood and a defoaming settling chamber where separation of gas from blood takes place. In a bubble oxygenator, oxygen gas bubbles are broken into a great number of small ones to provide an extensive interfacial transfer area. However, the small bubbles produced, though possessing a great surface area per unit volume, must be removed to prevent small blood vessels from being blocked by these bubbles. Thus, in practical operation, bubbles of moderate size (1 to 4 mm) are found to optimize both area and ease of removal (Bethune, 1986).

### 2.2.2 Film oxygenator

Film oxygenators usually have a solid vertical stationary support over which venous blood is spread in a thin film and then runs down into a settling chamber region. Films have been produced by using a hanging plate, a cloth curtain, a metal screen, and a pile of glass beads. Films can also be formed by spreading the blood over cylinders of discs that spin. This device is called the rotating disc oxygenator. As the shaft is rotated, films of blood are formed on the discs and are exposed to the gas phase in the upper part of the device. The first type of film oxygenator, the Kay-Cross oxygenator, was developed in 1957 and consisted of a pyrex cylinder 33 cm long by 13.3 cm in diameter.

Fifty-nine stainless steel siliconized or Teflon-coated discs 0.4 mm thick and 12.2 cm in diameter were mounted 0.5 cm apart using spacers on the shaft. When filled with 1.4 liters of blood, the blood level is about 1/3 from the bottom to the top. At 120 rpm, a film of roughly 0.8 square meters is generated. This film is sufficient to fully arterialize 2 liters of blood per minute. The newer models of this oxygenator are quite similar to the original one, and are among the most widely used oxygenators in clinical practice (Galletti *et al.*, 1962).

### 2.2.3 Membrane oxygenators

To avoid blood trauma caused by direct contact of blood with oxygen, devices were proposed in which a membrane separates the two phases. The membranes, silicon rubber and teflon, are essentially permeable to gases only and not to liquids. Transport of oxygen and carbon dioxide depend on the nature of the membrane, particularly the solubility of oxygen and carbon dioxide in the membrane. The driving force for oxygen transport in this device is about 670 mmHg inlet partial pressure of oxygen.

### 2.2.4 Intravascular oxygenator (IVOX)

Intravascular oxygenators provide oxygen and removes carbon dioxide from the blood returning to the heart. It is composed of a bundle of membranes. IVOX, developed by Cardiopulmonics, Inc., has been used in clinical trials since 1990 (Jurmann *et al.*, 1992). It is composed of 1,200 hollow fibers, each with 270  $\mu\text{m}$  in inner diameter and 380  $\mu\text{m}$  in outer diameter. The provided surface area is 9,318 square cm with oxygen transport capacity of 325 ml/min and carbon dioxide transfer capacity of 490 ml/min

(Mortenson et al., 1989). Because the size is large (10.8 mm in diameter and 650 mm in length), it can be placed only in a large vein through venotomy. Furthermore it is capable of exchanging only a fraction of adult resting metabolic requirement.

As described, a mechanical ventilator requires the positive airway pressures which can cause further damage to lung tissue. Oxygenators use mechanical pumps to transport blood in the body. The IVOX uses bunches of hollow fibers for gas exchange. All these devices, however, suffer from low gas transfer rates and require a large blood-contact area. An extensive interfacial transfer area would be possible for the bubble oxygenator because the smaller bubbles provide larger surface area per unit volume if the oxygen bubble removal is not required.

### 2.3 Bubble formation in quiescent liquid

Among the various bubble-forming methods, the method of dispersion through submerged orifices or holes is the simplest and common. As the gas flows to the orifice, the gas pressure at the gas liquid interface rises. To maintain pressure equilibrium at the interface, the interface bulges, forming a dome of steadily decreasing radius of curvature. When the bubble radius becomes equal to the radius of the orifice, the gas liquid interface has become a hemisphere with its radius equal to that of the orifice. More gas through the orifice will force the interface to expand, causing a further increase of the radius of the curvature. Because the increased radius of curvature of the interface means a reduced pressure inside the bubble, more gas will flow into the bubble, causing a further increase of the radius of bubble and consequently reducing the pressure of gas coming from

orifice. At this moment, the bubble is separated from the orifice if the detaching forces become sufficiently strong or keeps growing until an imbalance of forces exists for bubble detachment.

Much work has been done for bubble formation from a submerged orifice to a fluid. Since the bubble formation is strongly influenced by the conditions of the gas supply to the bubble generating mechanism, they may be classified into three conditions: constant flow, constant pressure, and intermediate conditions as illustrated in Figure 2.1.

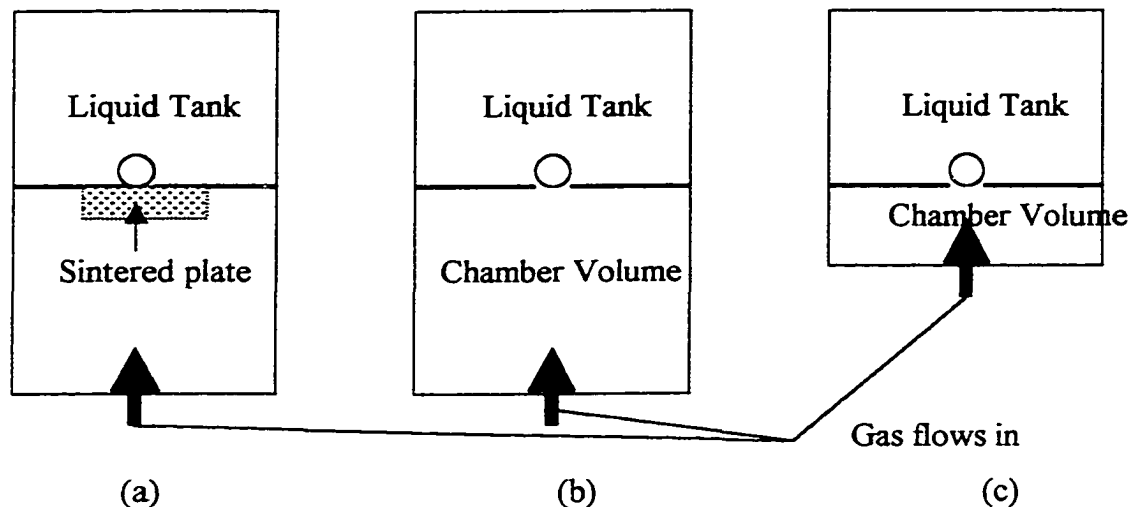


Figure 2.1 Bubble formation conditions: (a) constant flow, (b) constant pressure, and (c) intermediate condition

The pressure difference between the orifice and the gas stream is closely related to the effect of chamber volume, defined as the volume between the orifice and the gas inlet to the chamber. When the pressure drop across the orifice is large and the pressure variations below the orifice during bubble formation are small, the bubbles form under constant flow conditions. Davidson and Schuler have used a sintered plate to obtain a

high pressure drop near the orifice. This condition is illustrated in the Figure 2.1 (a). The constant flow condition can be achieved from a long, thin capillary that causes a high pressure drop between orifice and gas inlet before the capillary normally at the control valve. The constant flow condition is thus assumed that the rate of bubble growth is equal to the flow rate of the gas entering the system.

If the pressure on the air supply side of the orifice is maintained constant during bubble formation, instantaneous gas flow rate through the orifice to the bubble increases. The chamber pressure at the moment of bubble detachment remains virtually the same as the maximum chamber pressure and the pressure fluctuations in this situation can be neglected. The constant pressure arrangement is in Figure 2.1 (b). Therefore, there is no more constant flow conditions, and the bubble growth rate varies. This condition is obtained by using large chamber volume. Between these two conditions, both the chamber pressure and the flow rate are time dependent (Figure 2.1 (c)).

### 2.3.1 Bubble formation under constant flow conditions

Under constant flow conditions, the gas flow rate into the bubble through a nozzle is considered constant. Therefore, the forces acting on the bubble are considered independently. The quasi-static force balance for the bubble at the detaching state has been used to predict bubble formation in this case. The following assumptions are commonly used to develop models: (i) the pressure inside bubble is uniform, and (ii) the bubble remains spherical at all times. Ramakrishnan, Kumar and Kuloor (1969) have introduced static balance of various forces to model the bubble formation. The bubble is assumed to grow spherically in two stages: expansion and detaching . During the first

stage, the bubble is assumed to stay at the orifice, whereas in the detachment stage the bubble moves away from the nozzle while its base remains fixed until it detaches. The two stages of bubble formation are shown in Figure 2.2.

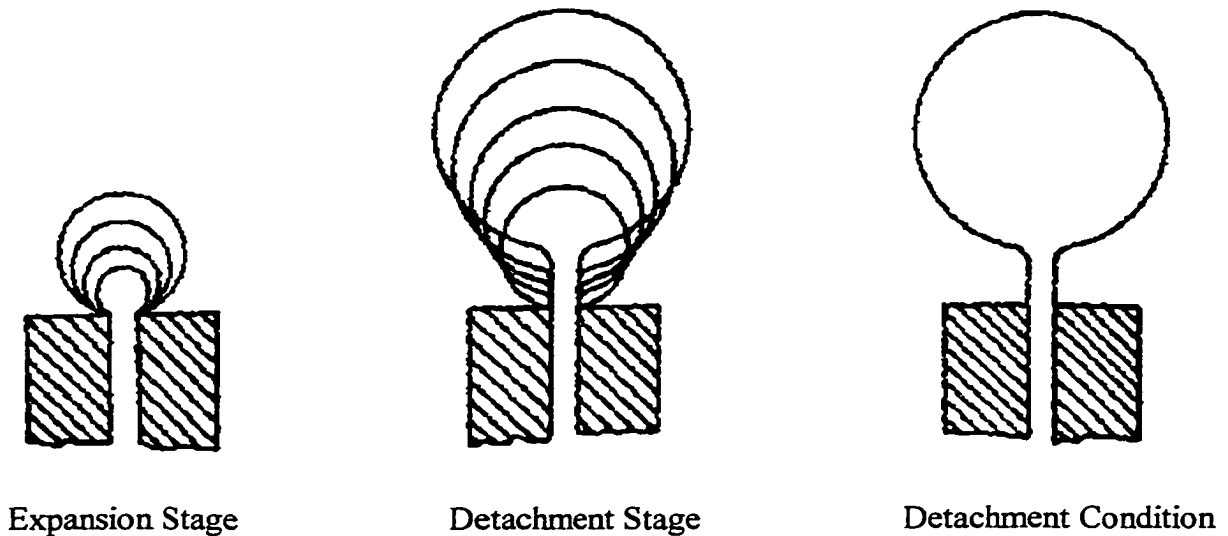


Figure 2.2 Mechanism of bubble formation (Adapted from Ramakrishnan et al., 1969)

When the flow rate of the gas into the bubble is very small, the surface tension and the buoyancy force - - the main forces - - act downward and upward, respectively. The bubble base remains fixed to the nozzle until the buoyancy force exceeds the surface tension force. Blanchard and Syzdek (1977) have introduced the bubble formation at the end of glass capillary tip in water. Bubbles with the radius of 200 to 2000  $\mu\text{m}$  are produced from the capillaries with the tip radius of 0.8 to 1000  $\mu\text{m}$ . The static force balance between buoyancy and surface tension is used. In addition, production of bubbles with 100  $\mu\text{m}$  requires a tip radius of 0.1  $\mu\text{m}$  and  $14.4 \times 10^5$  Pascal according to their prediction.

In an experimental study of microbubbles, Unkel (1991) produced bubbles with radius ranges from 7.3 to 21  $\mu m$ . These sizes of bubble production were made possible by introducing an pulse of undetermined pressure into the micropipette by punching the syringe attached to the pipette. Therefore, it is suspected that the bubble is attached at the tip until gas is sucked out from the bubble when the syringe is released. This gas flow back into the syringe may cause a pressure decrease at the tip and would assist the detachment of bubbles as the neck collapses in addition to the gas momentum.

When the gas flow rate is increased, the drag force due the expansion influences bubble formation. The inertial force due to the upward mass acceleration of fluid surrounding the bubble is also included and can be computed from the rate of change of momentum of the forming bubble. The quantitative expressions for the various forces are listed as follows:

$$\text{Buoyancy force} = F_B = V_b(\rho_L - \rho_g)g \quad (2.1)$$

$$\text{Viscous drag} = F_D = 6\pi r_e \mu v_e \quad (2.2)$$

$$\text{Surface tension force} = F_\sigma = \pi D \sigma (\cos \theta) \quad (2.3)$$

$$\text{Inertial force} = F_I = \frac{d}{dt_e}(Mv_e) = \frac{Q^2(\rho_g + \frac{11}{16}\rho_L)V^{-2/3}}{12\pi(3/4\pi)^{2/3}} \quad (2.4)$$

Where  $V_b$  is volume of the bubble,  $D$  is inner diameter of the nozzle,  $\sigma$  is surface tension

for the bubble,  $\rho_L$  and  $\rho_g$  are density of liquid and gas respectively, and  $\theta$  is the contact angle. The term  $M$  is the virtual mass of the bubble, is taken to be  $11/16^{\text{th}}$  of its volume of liquid surrounding it (Ramakrishnan *et al.*, 1969; Terasaka *et al.*, 1993).  $v_e$  and  $t_e$  is the velocity and time of expansion of the bubble respectively. The volume of this stage is obtained by assuming that the downward forces are equal to the upward forces as below.

$$F_B = F_D + F_\sigma + F_I \quad (2.5)$$

The volume of bubble at this stage is obtained by making a force balance of equations from (2.1) to (2.4) as follows (Ramakrishnan *et al.*, 1969):

$$(V_E)^{\frac{5}{3}} = \frac{11}{192\pi \left(\frac{3}{4\pi}\right)^{\frac{2}{3}} g} Q^2 + \frac{3}{2\left(\frac{3}{4}\pi\right)^{\frac{1}{3}} g} \frac{\mu}{\rho_L} Q(V_E)^{\frac{1}{3}} + \pi D \frac{\sigma}{\rho_L} (V_E)^{\frac{2}{3}} \quad (2.6)$$

During the detachment stage, the upward forces are larger than the downward forces. The bubble is assumed to detach when its base has covered a distance equal to the radius of the bubble at the end of expansion stage. At this stage, the force balance is assumed as follows:

$$\frac{d}{dt}(Mv') = (V_E + Qt)\rho_L g - 6\pi\mu v' - \pi D\sigma \cos \theta \quad (2.7)$$

where  $v'$  is the velocity of center of bubble, which is the addition of the velocity of the

center of the bubble and the velocity of the center due to expansion and expressed as  $v + \frac{dr}{dt}$ . The velocity of the center of the bubble is replaced by  $v = Q \frac{dx}{dt}$  and solved for  $x$ . The bubble is assumed to detach when  $x = r_E$ . The final bubble volume  $V_F$  is calculated with the following equation by iteration (Ramakrishnan *et al.*, 1962).

$$r_E = \frac{B}{2Q(A+1)} [(V_F)^2 - (V_E)^2] - \left(\frac{C}{AQ}\right)(V_F - V_E) - \frac{3G}{2Q(A - \frac{1}{3})} [(V_F)^{\frac{2}{3}} - (V_E)^{\frac{2}{3}}] \quad (2.8)$$

where  $A = 1 + 96\pi (1.25)r_E \frac{\mu}{11\rho_L Q}$ ,  $B = \frac{16g}{11Q}$ ,  $C = \frac{16\pi D\sigma \cos\theta}{11\rho_L Q}$ ,  $E = \frac{Q}{12\pi \left(\frac{3}{4\pi}\right)^{\frac{2}{3}}}$ ,

and  $G = \frac{24\mu}{11\left(\frac{3}{4\pi}\right)^{\frac{1}{3}}\rho_L}$

This model predicts the bubble formation from an orifice diameter of 0.1378 to 0.7042 cm with gas flow rate of 1 to 80  $cm^3 / sec$ . The produced bubble volumes are varied from 0.1 to 2  $cm^3$ . However, the gas momentum is neglected in this model. The equations of bubble formation are not continuous and have to be solved separately. The detachment condition is not realistic, either. Lastly, buoyancy force is the main detaching force. However, smaller bubbles have much less buoyancy force, and other forces need to be considered for bubbles of radius smaller than 40  $\mu m$ .

### 2.3.2. Bubble formation under constant pressure conditions

In the bubble formation under constant pressure condition, the pressure below the orifice is maintained nearly constant throughout the formation of bubble by using an infinite gas chamber. In this situation, flow rate of gas through the nozzle into the bubble varies, and the bubble growth rate is not constant. The one stage model proposed by Davidson and Schuler is to allow the change in gas flow rate. The gas flow rate into the growing bubble through an orifice is expressed by the orifice equation (Davidson and Schuler, 1960). It is derived by applying conservation of mass and energy balance over the control volume of chamber and bubble.

$$Q_0 = \frac{dV_b}{dt} = K(P_c - P_{atm} - \rho_L gh - \frac{2\sigma}{R} + \rho_L gs)^{0.5} \quad (2.9)$$

Where  $P_c$  is the pressure in the gas chamber,  $P_{atm}$  is atmospheric pressure,  $s$  is a distance of center of the bubble from the nozzle, and  $K$  is the orifice constant. For a large gas flow rate, the equation of bubble motion is set by balancing upward buoyancy force with downward inertia and drag forces.

$$\rho_L V_b g = \rho_L \frac{11}{16} \frac{d(V_b v)}{dt} + C_D \frac{\pi D_b^2}{4} \frac{\rho_L v^2}{2} \quad (2.10)$$

Bubbles with 3.9 to 5.8  $cm^3$  in volume are produced through orifice with radius of 0.975 mm in Glycerol solution. However, the influences of gas momentum and surface tension force are neglected in their modeling.

A two stage model is assumed by Satyanarayan and his coworkers to model the bubble formation in a constant pressure condition. The variation of flow rate through the nozzle during the first stage is expressed by the orifice equation (2.1) introduced above. At the end of the expansion stage, the same force balance used for constant flow condition in equation (2.5) is applied. During the detachment stage, the bubble is assumed to detach when the base is stretched a distance equal to the radius of the bubble at the end of expansion stage. The flow rate at this stage is assumed to be constant and equal to the flow rate at the end of the expansion stage. The force balance equation of the detachment stage, the equation (2.7), in the constant flow conditions is used. Bubbles with 0.1 to 0.9  $cm^3$  in volume are produced through the orifice diameter of 0.5 to 0.9 mm with gas flow rate of 2 to 40  $cm^3/sec$  in their experiments. The two-stage model used in this study is not applicable continuously, and the models for two different stages have to be solved separately. In addition, the assumption of bubble detachment is not realistic because detachment is a dynamic process.

### 2.3.3 Bubble formation under variable chamber pressure

In this case, just before bubble detachment the pressure inside the bubble is minimal, and the chamber pressure is at its lowest. After the bubble detachment, there exists a weeping time in which the bubble is not forming. During this period, the chamber pressure builds up sufficiently to provide the excess pressure needed to generate the bubble. Therefore, the pressure inside the chamber and flow rate into the bubble are time dependent. A typical pressure variation and a bubble formation condition are in Figure 2.3 and 2.4, respectively.

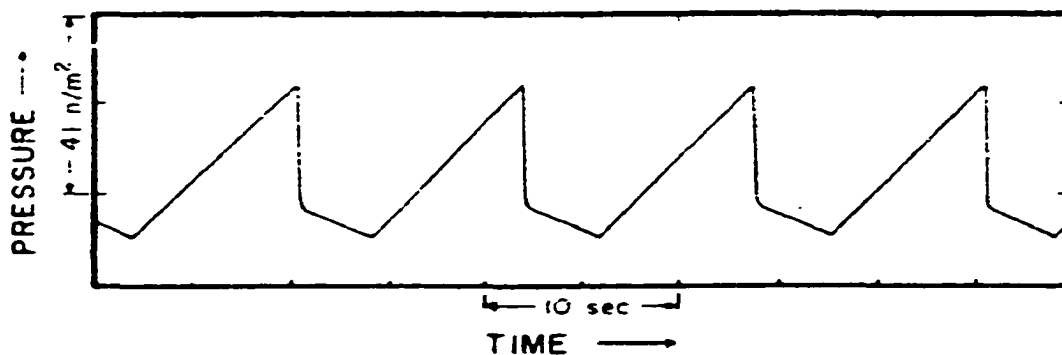


Figure 2.3 Pressure variation in the chamber (adapted from Park, 1977)  
 $V_c = 11.7 \text{ cm}^3$ ,  $D_i = 0.12 \text{ cm}$ ,  $V_b = 0.05 \text{ cm}^3$  (radius = 0.23 cm)

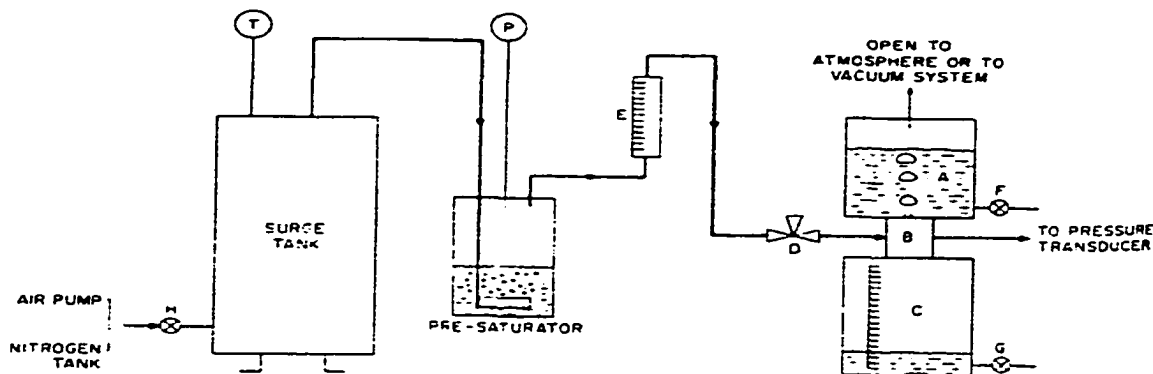


Figure 2.4 Bubble formation in the intermediate condition  
 (adapted from Park, 1977)

Khurana and Kumar (1969) introduce the gas flow rate into the bubble as a function of time as follows:

$$Q_t = \frac{E_1 - R_1 Q_L - E_2}{R_V} + \frac{E_0}{R_D} e^{-\frac{t}{R_D C \alpha}} \quad (2.11)$$

where  $E_1$  is pressure at source and has internal resistance  $R_1$  which comprises the pipeline resistances.  $E_2$  is hydrostatic pressure due to submergence of orifice,  $R_v$  is resistance at the valve,  $R_D$  is the addition of tip and bubble resistance,  $E_0$  is the pressure just before the bubble forms.  $Q_L$  is constant volumetric flow rate caused by pressure difference between orifice and source. Chamber capacitance  $C_{ch}$  is introduced to express the time varying flow rate of gas with the chamber volume (Khurana et al., 1969).

A dynamic interaction between chamber volume and gas flow through the orifice has developed by Park (1977). The conservation of mass within the chamber volume provides

$$V_C \left( \frac{d\rho_C}{dt} \right) = \dot{m}_i - \dot{m}_o = Q_i \rho_i - Q_o \rho_o \quad (2.12)$$

Applying ideal gas law after dividing the above equation by  $\rho_i$  and set  $\rho_o$  is equal to  $\rho_C$  is expressed as

$$V_C \frac{T_i}{P_i} d \left( \frac{P_c}{T_c} \right) / dt = Q_i - \frac{P_c T_i}{T_c P_i} Q_o \quad (2.13)$$

If the pressure fluctuations in the chamber are so rapid as to be adiabatic, the equation becomes

$$\frac{V_C}{k} \frac{T_i}{P_i T_c} \frac{dP_c}{dt} = Q_i - \frac{P_c T_i}{T_c P_i} Q_o \quad (2.14)$$

During the depressurization of the chamber, the flow rate through orifice  $Q_o$  is assumed to be much larger than  $Q_i$  and  $P_c T_i / T_c P_i$  is close enough to be 1. With these simplifications, the volume change at the depressurization step is expressed as

$$Q_o = -\frac{V_c}{kP_c} \frac{dP_c}{dt} \quad (2.15)$$

Since the volumetric flow rate through the nozzle is equal to the volumetric rate of the growing a bubble, the bubble volume is obtained by integrating above equation with respect to time as

$$V_b = \frac{V_c}{kP_{avg}} (P_{max} - P_{min}) \quad (2.16)$$

Unlike the models described above, potential flow theory is applied to derive an equation of motion of a bubble (McCann *et al.*, 1969, Tsuge *et al.*, 1993, Dong-Hyun Yoo *et al.*, 1998). By assuming that the pressure inside the bubble to be constant around its surface, the potential flow solution is substituted into the Bernoulli's equation to yield the relation between radial expansion of the bubble to the pressure within it. McCann and Prince (1969) applied potential flow theory to drive an equation of motion of the bubble as

$$V_b g = \frac{1}{2} \frac{d}{dt} \left( V_b \frac{ds}{dt} \right) \quad (2.17)$$

where  $s$  is distance of bubble center from orifice plate during bubble formation. This equation is the same equation found by Davidson and Schuler by applying the balance between the buoyancy force and the upward mass acceleration of the fluid surrounding the bubble. The pressure inside the bubble is assumed to be the average pressure in the liquid at the bubble boundary plus the pressure due to surface tension force. By substituting a potential flow solution to Bernoulli's equation, the pressure inside the bubble is expressed as

$$\bar{P} = \frac{\rho_L}{g_c} (1.5 \dot{R}^2 + R \ddot{R} - gs) - \frac{\rho_L U^2 R}{4g_c(S+R)} \left[ 1 + \frac{5s}{2R} - \frac{3}{2} \left( \frac{s}{R} \right)^3 \right] + P_\infty + \frac{2\sigma}{R} \quad (2.18)$$

where  $\bar{P}$  is the pressure inside bubble and  $R$  is the radius of the bubble. The relation between volumetric gas flow rate, and the pressure drop across the nozzle is considered by steady state orifice equation.

$$\frac{dV_b}{dt} = k(P_c - \bar{P} - P_{wake})^{\frac{1}{2}} \quad (2.19)$$

In the above equation, the pressure field in the wake of a preceding bubble is accounted for and represented by the last term on the right hand side of the equation.

La Nauze and Harris (1977) account for density difference between gas and liquid in setting up the equation of motion and introduce a modified orifice equation from Davidson and Schuler to express gas flow in the bubble as follows:

$$V_b(\rho_L - \rho_g)g = \frac{d(M\dot{S})}{dt} = (\rho_g - \frac{11}{16}\rho_L)(\dot{V}\dot{S} + V\ddot{S}) \quad (2.20)$$

and

$$Q = k(P_C - \rho gh + \rho gS - \frac{2\sigma}{R})^{\frac{1}{2}} \quad (2.21)$$

The pressure variation in the bubble is developed from a force balance as

$$P_C - \rho gh + \rho gS - \Delta P_\sigma - \frac{1}{k^2}\dot{V}^2 = \frac{\rho h\ddot{V}}{A} + \rho(R\ddot{R} + \frac{3}{2}\dot{R}^2) \quad (2.22)$$

The first and second terms on the right-hand side represent the inertia of the liquid due to bubble translation and the inertia of liquid surrounding the bubble due to expansion, respectively. These equations above are solved numerically, and the results are represented on the Figure 2.5 and Figure 2.6.

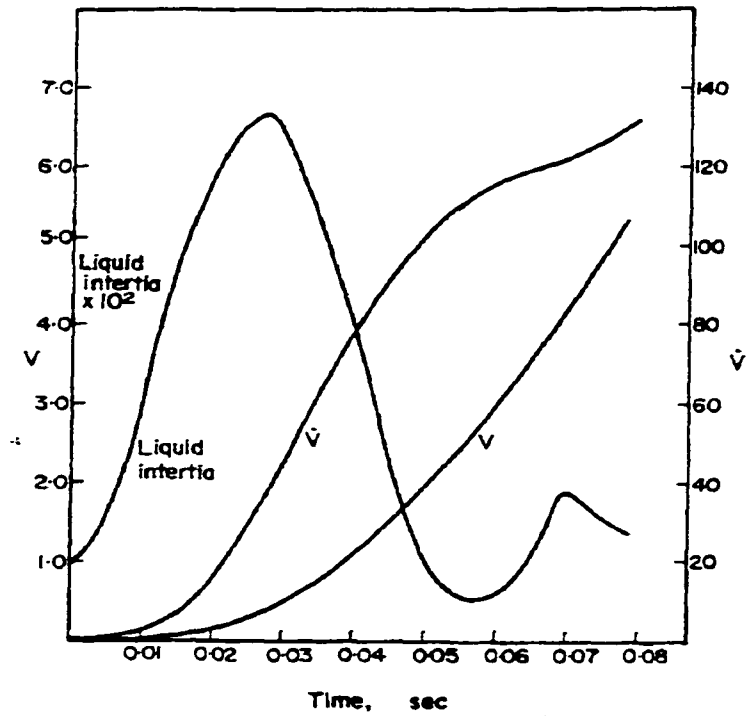


Figure 2.5 Theoretical curves for bubble volume ( $cm^3$ ), instantaneous flow rate,  $\dot{V}$  ( $cm^3/sec$ ), and liquid inertia for the case of orifice diameter=0.167cm,  $P=877$  ( $gm/cm^2$ ),  $h=10$  (cm) (adapted from La Nauze and Harris, 1972)

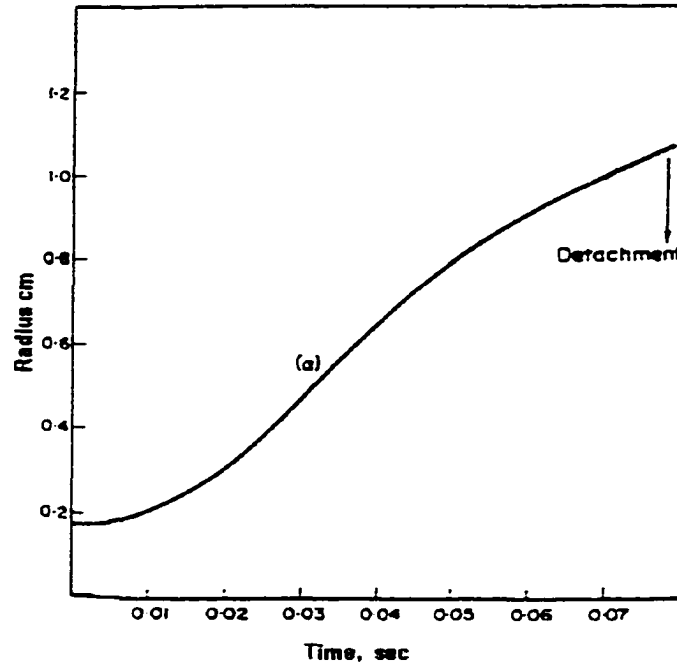


Figure 2.6 Theoretical curves for radius with time for orifice radius of 0.167 cm (modified from La Nauze and Harris, 1972)

From this Figure, the liquid inertia plays an important role in bubble formation. The force required to accelerate the liquid initially is very high, which represents the slow initial rate of bubble growth. The theoretical bubble growth curve represented as (a) in Figure 2.6 also matches well with the experimental data that the bubble radius at detachment is about 1.08 cm.

The modified Rayleigh equation is used to express the pressure balance of the bubble under low gravity of 0.17g and 0.05g as follows (Tsuge et al., 1997):

$$P_b - P_h = \rho_L \left[ R \frac{d^2 R}{dt^2} + 1.5 \left( \frac{dR}{dt} \right)^2 \right] + \frac{2\sigma}{R} + \left( \frac{4\mu}{R} \right) \frac{dR}{dt} \quad (2.23)$$

To express the pressure balance under elevated pressure, a gas momentum rate term is added on the equation (2.23) above (Dong-Hyun Yoo et al., 1998).

$$P_b - P_h = \rho_L \left[ R \frac{d^2 R}{dt^2} + 1.5 \left( \frac{dR}{dt} \right)^2 \right] + \frac{2\sigma}{R} + \left( \frac{4\mu}{R} \right) \frac{dR}{dt} - \frac{1}{2} \rho_g U_o^2 \cos \theta \quad (2.24)$$

where,  $U_o$  is gas velocity through orifice and  $\theta$  is the angle between vertical axis to bubble surface at any element. This equation is solved numerically with the equation of motion of rising bubble and orifice equation simultaneously.

## 2.4 Bubble formation in flowing liquid

### 2.4.1 Cocurrent flow

Chuang and Goldschmidt developed a model for bubble formation from submerged capillaries in coflowing as well as quiescent streams. One stage model of bubble formation is used to describe bubble production with a constant gas flow up to  $85.8 \text{ cm}^3/\text{sec}$  through the smaller nozzles in the order of  $0.0014 \text{ cm}$  in diameter while generating bubbles from  $40$  to  $700 \text{ }\mu\text{m}$  in diameter. Momentum flux of the gas phase and the wake effect of the previous bubble are added to the abovementioned model. Therefore, the upward forces can be buoyancy force, momentum flux, and drag force. The downward forces arise from the surface tension and inertial force. The force balance at the bubble detachment in this model is as follows:

$$\frac{\pi (D_b)^3 \rho_w g}{6} + \frac{C_D \pi (D_b^2 - D_o^2)}{4} \left( V - \frac{dS}{dt} \right)^2 \frac{\rho_w}{2} = \pi D_o \sigma + \frac{1}{2} \frac{d}{dt} \left( M \frac{dS}{dt} \right) \quad (2.25)$$

where  $C_D$  is viscous drag coefficient,  $D_b$  the bubble diameter,  $D_o$  nozzle outside diameter,  $M$  the virtual mass of the bubble,  $S$  the distance from the center of the bubble to the orifice,  $V$  velocity of the coflowing liquid stream. The differential terms in this equation are then transformed into a nonlinear equation in terms of bubbling frequency and wake velocity as well as bubble and orifice diameter. It is concluded that when the coflowing velocity is greater than 1 ft/sec the resulting drag force becomes a predominant factor. Therefore, the dependence of the gas flow rate to the bubble volume become negligible (Chuang et al., 1970).

Sada and his co-workers observed that the bubble size formed in flowing liquid decreased as the coflowing liquid velocity increased by using two nozzles of 0.086 cm and 0.305 cm in diameter. The gas flow rate varied from 0.33  $cm^3/sec$  to 36.2  $cm^3/sec$  and the coflowing liquid velocities varied from 0 cm/sec to 154.9 cm/sec. In addition, three different types of bubble formation: single bubbles, coalescent bubbles and gas jets are observed depending on the gas flow rate and the liquid flow rate. The size of the bubble produced in single bubble formation ranges about 0.5 to 0.2 cm in diameter. The effect of the nozzle diameter and the gas flow rate in the formation of single bubbles and coalescent bubbles are correlated empirically by the modified Froud number ( $N_{Fr}$ ) as follows (Sada et al., 1978):

$$N_{Fr} = \frac{u^2}{gd + 0.33U_L^2} \quad (2.26)$$

(i) for single bubbles

$$\frac{d}{D_i} = 155 N_{Fr}^{0.2} \quad (2.27)$$

(ii) for coalescence of bubbles

$$\frac{d}{D_i} = 2.5 N_{Fr}^{0.2} \left( \frac{D_i}{0.086} \right)^{0.1} - 3.5 \quad (2.28)$$

Where  $D_i$  is the nozzle diameter,  $d$  the diameter of initial bubble,  $u$  the gas velocity through nozzle, and  $U_L$  coflowing liquid velocity.

#### 2.4.2. Crosscurrent flow

Tsuge et al. (1981) investigated the effect of the crosscurrent flow on the bubble formation mechanism as the gas chamber pressure is varied. The chamber with  $63.1 \text{ cm}^3$  in volume with gas flow rate of  $0.689$  and  $0.696 \text{ cm}^3/\text{sec}$  and crosscurrent liquid velocity of  $0$  to  $12.8 \text{ cm/sec}$  produces bubbles with the volume of  $0.14$  to  $0.167 \text{ cm}^3$  from orifice of  $0.145 \text{ cm}$  in diameter. Two stages of bubble formation (expansion and detachment stage) are assumed. The velocity potential is expressed as the sum of the potential for flow around a translating sphere, the potential associated with the expansion and contraction of the bubble. By substituting the potential equation to the Bernoulli's equation, the pressure balance in expansion stage is expressed as

$$P_b - P_s = \rho_L \left[ R \left( \frac{d^2 R}{dt^2} \right) + 1.5 \left( \frac{dR}{dt} \right)^2 \right] + \frac{2\sigma}{R} \quad (2.29)$$

The bubble was assumed to be detached when the length of the neck of the bubble reached the length determined by following empirical function.

$$L_n / D_o = 1 - 0.02U_L \quad (2.30)$$

where  $L_n$  is the length of the bubble neck and  $U_L$  is liquid velocity.

Kawase et al. (1981) used the two-stage bubble formation concept from the Kumar and Kuloor model to describe the bubble formation in crosscurrent flow of liquid. In the case of low flow rate, volumetric flow rate of air  $Q$  during the expansion stage is assumed to be very small and set at zero. The volume of bubble at this stage is obtained as

$$V_b = \frac{\pi D_i \sigma \cos \Phi}{\Delta \rho g} \varphi \quad (2.31)$$

where  $D_i$  is nozzle diameter and  $\varphi$  is a correction factor. The angle  $\Phi$  is introduced to accommodate the drag force of the moving liquid and expressed as

$$\Phi = \arctan\left(\frac{F_3}{F_1}\right) \quad (2.32)$$

where the  $F_1$  is upward buoyant force and the  $F_3$  is the force due to a flow normal to the axis of the nozzle. The angle  $\Phi$  represents a virtual inclination which is equivalent to the bubble production from an inclined nozzle in quiescent fluid which represented by the

broken line in Figure 2.7.

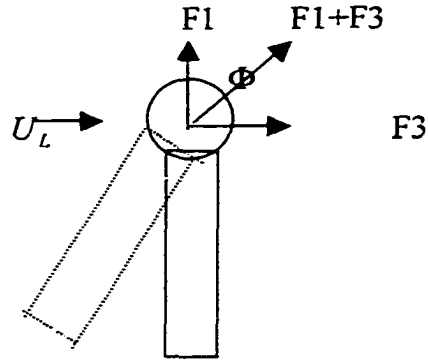


Figure 2.7 Model of bubble formation in a flowing fluid (modified from Kawase, 1981)

Alternately, when the gas flow rate is high, the surface tension force is neglected, and the forces due to inertia and buoyancy are considered only. The final volume of the bubble is calculated as

$$V_b = 1.378 \frac{Q^{6/5}}{g^{3/5}} \quad (2.33)$$

This model works well with experimental data for  $4 \text{ cm}^3 / \text{sec} < Q < 20 \text{ cm}^3 / \text{sec}$ . At a very high rate of continuous phase velocity, it is assumed that the bubble formed at the nozzle tip is displaced horizontally at the speed  $u$ , which is the velocity of flow. The detachment take place when the center of bubble is displaced by a distance  $uV_b / Q$  in the horizontal direction. The virtual inclination in this high flow rate case is

$$\Phi = \arctan\left(\frac{u_L V_b / Q_o}{D/2}\right) \quad (2.34)$$

The final volume of bubble is expressed as

$$V_b = 0.489 Q_o^{\frac{3}{2}} u_L^{-\frac{3}{2}} \quad (2.35)$$

Johnson et al. (1982) used static force balance equation to predict the size of bubbles formed at a frit surface with a cross flow of water through 150  $\mu\text{m}$  space between wall and frit surface. The frit consists of pore size of 4 to 8  $\mu\text{m}$  in diameter. The gas flows into the frit with the rate of 6  $\text{cm}^3/\text{min}$  and the bubble population ranges from 44 to 134  $\mu\text{m}$  in radius. The drag force is set equal to the surface tension force as follows:

$$C_D \frac{\rho_L U_L^2 A_p}{2} = \pi D \sigma \quad (2.36)$$

Where D is pore diameter of the frit. Since the liquid velocity varies with the position of the frit, the series of bubble diameters can be predicted. This force balance model provides a very good prediction of the observed bubble population, and this suggests the force balance approach is satisfactory for modeling the detachment condition for the crosscurrent flow condition.

They also studied bubble generation in the circular frit with sea water (Jounson et al., 1982). The circular frit with pore size of 4 to 5.5  $\mu\text{m}$  in diameter are used for bubble production with gas flow rate of 8  $\text{cm}^3/\text{min}$ . They used a disc on the top of frit separated

by liquid flow between them. With the liquid flow rates from 243 cm<sup>3</sup> /min. to 776 cm<sup>3</sup> /min., they produced bubbles ranges from 32.4 μm to 129.6 μm with sea water as a liquid flow. The median value of bubble diameter was about 49 μm. The wide variation of bubble size was reduced as liquid flow rate was increased. However, the median bubble diameter was unchanged. Faster liquid flow only reduced the size variation of bubbles, and the median value of the bubble size was the same.

Gosh et al. (1989) investigated bubble formations in crosscurrent flow conditions both experimentally and theoretically. In modeling this condition, the force due to flowing liquid velocity is added to the model for the bubble formation in stagnant liquid. The equation of motion is obtained by the balance of the resultant force due to the vertical buoyant force ( $F_B$ ) and the horizontal liquid drag force of crosscurrent flow ( $F_D$ ), the inertial force( $F_I$ ), drag force due to bubble motion ( $F_{bm}$ ) and surface tension force ( $F_\sigma$ ) as

$$\sqrt{F_B^2 + F_D^2} = F_I + F_{bm} + F_\sigma \quad (2.37)$$

For the experiments, air flow rates between 2.0 and 20.0 cm<sup>3</sup> /sec and liquid velocities ranging from 5 to 20 cm/sec are controlled by adjusting the rotation speed of the tank that holds liquid. Generally, bubble volume increases with increasing gas flow rates and decreases with shear flow around the orifice. The size of the bubble produced from orifice diameter of 0.145 cm and liquid velocity of 17.2 cm/sec ranges from 0.288 to 0.415 cm in radius with gas flow rate of 5 to 15 cm<sup>3</sup>/sec. Due to the liquid velocity, the bubble experiences an additional drag force, and the bubble is swept away from the

orifice at a smaller size than in the case of the stagnant liquid.

Kim et al. (1994) proposed a model for bubble and drop formation in crosscurrent liquid flow in microgravity. The bubble diameter at the detachment is predicted by the force balance of buoyancy force ( $F_B$ ) which acts vertically upward, momentum flux ( $F_M$ ) which is associated with the momentum of the injected fluid and acts in the injection direction, surface tension force at the nozzle ( $F_s$ ), inertia of bubble ( $F_I$ ) which is associated with the momentum of the surrounding liquid motion induced by the bubble and opposes the bubble penetration, and liquid drag force ( $F_D$ ) which acts in the downstream direction as follows.

$$F_B + F_M + F_s + F_D + F_I = 0 \quad (2.38)$$

Predictions of bubble size of this model show good agreement with experimental results from Kawase (1981) where the bubble diameter varies from 0.5 to 0.2 cm with liquid velocity of 0 to 23 cm/sec from 0.102 cm diameter orifice. In their model, drag coefficient for a solid sphere is used for different Reynolds numbers, and it is concluded that the drag coefficient and the effective cross sectional area of bubble are very important in the modeling.

The formation of gas bubble at a single orifice submerged in liquid involves complicated phenomena because many factors influence the size and shape of the forming bubbles. It may be concluded that the most important factors affecting bubble size at an orifice submerged in quiescent fluid are the gas flow rate, orifice radius, and dynamic bubble growth influenced by inertia of the liquid surrounding bubble. The other

factors are buoyancy force, hydrostatic force, surface tension, viscous drag, inertia of bubbles, gas momentum flux, and wake from detaching bubbles. A number of experimental studies on the formation of gas bubble have been made at a single orifice in quiescent liquid as well as in flowing liquid as the pressure in the gas chamber is varied. The bubble formation behavior indicates the strong influence of the gas supply condition to the bubble generating mechanism. When the chamber volume exists, the bubbles grow in highly complex behavior. Dynamic interaction between chamber volume, bubble, and orifice leads to a variable rate of bubble growth. The dynamic gas flow will be influenced by the inertia of the liquid surrounding the bubble. This phenomenon requires a dynamic bubble growth model described in this section.

In this study, the dynamic bubble growth behavior in the crosscurrent liquid flow particularly in the microchannel is employed to analyze the microbubble formation.

## CHAPTER 3

### MATHEMATICAL MODELING OF BUBBLE FORMATION IN MICROCHANNELS

Dynamic interaction between chamber volume, bubble, and orifice is explained with potential flow theory and successfully demonstrates the dynamic bubble formation behavior (Tsuge *et al.*, 1981). Energy balance for gas flow through the orifice during bubble formation has been successfully used (Davidson *et al.*, 1960). Conservation of mass to express dynamics between chamber volume and mass flow through the orifice is also used successfully (Park *et al.*, 1977). In this chapter a bubble formation model under crosscurrent liquid flow conditions in microchannel is developed based on thermodynamic equations for the gas, and a potential flow theory.

#### 3.1 The growth model and assumptions

The physical description of the bubbling situation is described in Figure 3.1. Gas flows into the chamber through the thin channel with average flow rate of  $Q_i$ . The chamber with volume  $V_c$ , pressure  $P_c$ , and temperature  $T_c$ , is opened to the orifice with surface area of  $S_o$ . The gas flows through the orifice with rate of  $Q_o$  into the channel of liquid flow of  $Q_L$ .

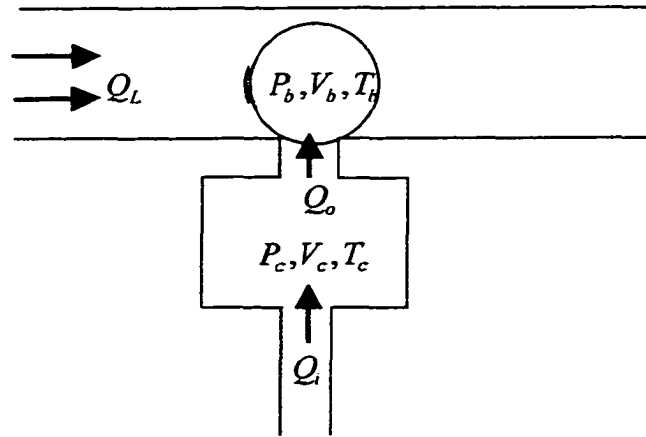


Figure 3.1 Bubble formation diagram

The following assumptions are made for modeling this system: (1) pressure and temperature inside the bubble and the chamber are uniform; (2) the gas is ideal; (3) a pressure difference exists across the orifice ( $P_c - P_b$ ) and determines the rate of gas flow into the bubble; (4) the cross flowing liquid is isothermal, uniform, inviscid and irrotational; (5) there is no energy exchange or mass transfer across gas liquid interface; (6) buoyancy force is negligible; (7) the bubble remains spherical throughout the formation; (8) the bubble is connected to the orifice by a neck which has negligible volume compared with the spherical portion of bubble.

### 3.2 Pressure inside the chamber

The assumed condition of uniform temperature and pressure inside the chamber translates into the density of the flowing gas into and out of the chamber are the same. Apply the first law of thermodynamics, equation for conservation of energy, to the

chamber. Neglect changes in kinetic and potential energy between inlet and exit to have the unsteady state macroscopic energy balance as follows.

$$\frac{d}{dt}(V_c \rho_c U_c) = (\dot{m}_i - \dot{m}_o) \left( U_c + \frac{P_c}{\rho_c} \right) + Q - W \quad (3.1)^*$$

where  $U_c$  is the internal energy per unit mass of the gas in  $V_c$ ,  $Q$  is rate of external heat added and  $W$  the rate of external work. If the chamber is assumed to be adiabatic, then  $Q=0$ . The fixed volume does no external work and  $W=0$ . The material balance on the chamber yields

$$\frac{d}{dt}(V_c \rho_c) = \dot{m}_i - \dot{m}_o = (Q_i - Q_o) \rho_c \quad (3.2)^*$$

By substituting equation (3.2) to (3.1), the energy balance equation becomes (see the appendix A)

$$(V_c \rho_c) \frac{dU_c}{dt} = (Q_i - Q_o) P_c \quad (3.3)^*$$

From the ideal gas relations,  $dU = C_v dT$ ,  $\rho = \frac{PM}{RT}$ ,  $C_p - C_v = \frac{R}{M}$ , and  $k = \frac{C_p}{C_v}$ , the

internal energy change can be expressed as

$$V_c \rho_c \frac{dU_c}{dt} = \frac{1}{k-1} [V_c \frac{dP_c}{dt} - P_c (Q_i - Q_o)] \quad (3.4)^*$$

Substitute equation (3.4) into (3.3) to yield the following equation for chamber pressure.

$$V_c \frac{dP_c}{dt} = k(Q_i - Q_o)P_c \quad (3.5)$$

This equation can relate the chamber pressure fluctuation with the difference between flow of gas in and out of the chamber. The above equation is identical to that given by Tsuge(1981), Marshall(1993), Terasaka (1999).

### 3.3 Gas flow through orifice

For isothermal and constant density, the mass and mechanical energy balances across a orifice leads to the equation for determining the mass flow rate of a gas (Bird *et.al.*, 1960).

$$w = \rho_g \langle v \rangle A_c = C_d A_o \sqrt{\frac{2\rho (P_c - P_b)}{1 - (A_o / A_c)^2}} \quad (3.6)$$

Where  $w$  is mass rate of flow,  $A_c$  and  $A_o$  are cross sectional areas of chamber and orifice respectively. The discharge coefficient  $C_d$  is an experimental parameter. It depends on the geometry of orifice and Reynolds number. For a high Reynolds number, discharge coefficient approaches to constant value of 0.61. However, for laminar flow, it may vary

with Reynolds number and need to be determined with experimental data. Rearrangement of above equation gives the expression for chamber pressure as follows;

$$P_c = P_b + \frac{Q_o^2}{2C_d^2 A_o^2} \left[ 1 - \left( \frac{A_o}{A_c} \right)^2 \right] \rho_g \quad (3.7a)$$

Therefore, the gas flow rate from the orifice is

$$Q_o = CA_o (P_c - P_b)^{\frac{1}{2}} \quad (3.7b)$$

where C is experimental parameter that depends on the geometry of orifice and Re. For a high Re, it approaches to a constant value. However for laminar flow, it may vary with Re and needs to be determined from experimental data.

### 3.4 Bubble growth

Application of the first law of thermodynamics, similar to that used for the chamber pressure analysis, to the bubble yields

$$\frac{d}{dt}(V_b \rho_b U_b) = \dot{m}_o \left( U_b + \frac{P_b}{\rho_b} \right) + Q - W \quad (3.8)*$$

Assume the bubble behaves adiabatically. The rate of external work done by expanding bubble is given by

$$W = P_b \frac{dV_b}{dt} \quad (3.9)$$

From a mass balance

$$\frac{d}{dt}(V_b \rho_b) = \dot{m}_o = \rho_c Q_o \quad (3.10)^*$$

Application of ideal gas relationship as in the section 3.2 into equation (3.10) to yield

$$V_b \rho_b \frac{dU_b}{dt} = \frac{1}{k-1} \left( V_b \frac{dP_b}{dt} - \frac{\rho_c Q_o P_b}{\rho_b} + P_b \frac{dV_b}{dt} \right) \quad (3.11)^*$$

(see Appendix B)

By substituting the above equation into equation (3.8) becomes

$$\frac{1}{k-1} \left( V_b \frac{dP_b}{dt} - \frac{\rho_c Q_o P_b}{\rho_b} + P_b \frac{dV_b}{dt} \right) = \frac{P_b \rho_c Q_o}{\rho_b} - P_b \frac{dV_b}{dt} \quad (3.12)^*$$

In addition, from the ideal gas law

$$\frac{\rho_c}{\rho_b} = \frac{P_c T_b}{P_b T_c} \quad (3.13)$$

and assume  $T_b/T_c \cong 1$ , then the equation (3.12) becomes

$$V_b \frac{dP_b}{dt} + kP_b \frac{dV_b}{dt} = kP_c Q_o \quad (3.14)$$

which is the same expression used by Marmur and Rubin (1976). If the bubble is assumed incompressible and expand isothermally,  $Q_o$  is reduced to  $dV_b/dt$ . This expression of reduced  $Q_o$  is used by Park (1977), Terasaka (1993), Yoo (1998), and Tsuge (1997).

### 3.5 Pressure at the bubble surface

To describe bubble expansion behavior, it is assumed that the liquid is invicid, incompressible, and irrotational. This situation can be modeled by superposition of bubble expansion in fluid and uniform fluid stream. The idealized condition under consideration is in Figure 3.2.

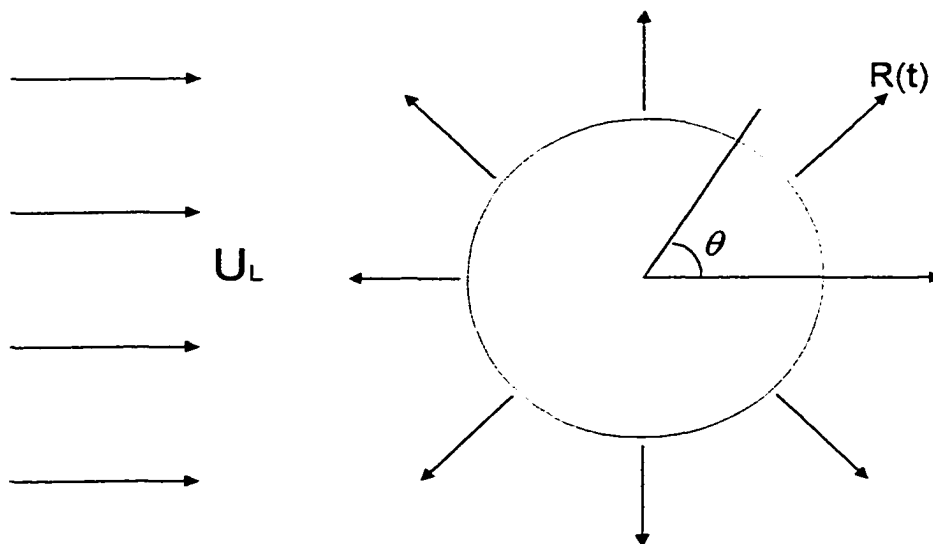


Figure 3.2 Schematic of bubble growth in uniform flow

The expansion of the bubble is assumed purely radial. In this case, the velocity can be related to the potential by

$$v_r = \frac{\partial \Phi_b}{\partial r} \quad (3.15)$$

where  $\Phi_b$  is the velocity potential of expanding bubble. The continuity equation in spherical coordinates gives

$$\nabla^2 \Phi_b = \frac{1}{r} \frac{\partial}{\partial r} \left( r^2 \frac{\partial \Phi_b}{\partial r} \right) = 0 \quad (3.16)$$

Assume that the fluid is stationary at infinity and that the bubble has pure radial expansion. These boundary conditions are described as follows:

$$v_r = \frac{\partial \Phi_b}{\partial r} = 0 \quad \text{at } r \rightarrow \infty \quad (3.17)$$

$$v_r = \frac{\partial \Phi_b}{\partial r} = \dot{R}(t) \quad \text{at } r=R \quad (3.18)$$

By solving the equation, the radial velocity of bubble growth and velocity potential are

$$v_r = \left( \frac{R}{r} \right)^2 \dot{R} \quad (3.19)^*$$

and

$$\Phi_b = -\frac{R^2 \dot{R}}{r} \quad (3.20)^*$$

The velocity potential of uniform flow in spherical coordinates is given by

$$\Phi_u = -U_L r \cos \theta \quad (3.21)^*$$

The velocity potential for expanding bubble in uniformly flowing fluid is expressed as

$$\Phi = \Phi_b + \Phi_u = -\frac{R^2 \dot{R}}{r} - U_L r \cos \theta \quad (3.22)^*$$

The unsteady Bernoulli equation for irrotational flow is

$$\frac{\partial \Phi}{\partial t} + \frac{1}{2} v^2 = \frac{p_\infty - p(R)}{\rho_L} \quad (3.23)^*$$

where

$$v^2 = \left( \frac{\partial \Phi}{\partial R} \right)^2 + \left( \frac{1}{R} \frac{\partial \Phi}{\partial \theta} \right)^2 \quad (3.24)$$

After plug the equation (3.22) into equation (3.23), and (3.24), the pressure at the bubble surface is expressed as

$$\frac{p(R) - p_\infty}{\rho_L} = R \ddot{R} + \frac{3}{2} \dot{R}^2 + \frac{1}{2} U_L^2 + \dot{R} U_L \cos \theta \quad (3.25)^*$$

In addition, the pressure at the bubble surface can be related with the pressure inside the bubble as

$$p(R) = p_b - \frac{2\sigma}{R} \quad (3.26)$$

The pressure of the bubble becomes

$$p_b = \alpha \rho_L \left( R \ddot{R} + \frac{3}{2} \dot{R}^2 + \frac{1}{2} U_L^2 + \dot{R} U_L \cos \theta \right) + \frac{2\sigma}{R} + p_\infty \quad (3.27)^*$$

where  $\alpha$  is a correction factor that compensate the difference between real and ideal liquid. It is assumed that pressure inside the bubble is uniform at every point of its surface and independent of  $\theta$ .

### 3.6 Pressure in the crosscurrent liquid flowing channel

Consider the steady laminar flow of a fluid of constant density in trapezoidal channel. Transport phenomena in microscale channel is expected to be quite different from those in customary situations (Flockhart et. al, 1998). To determine the flow characteristics of trapezoidal channel, Shah (1978) described the results in terms of aspect ratio and Poiseuille number ( $P_o$ ). The Poiseuille number describes the flow characteristics of an isothermal, Newtonian fluid with fully developed laminar flow in an arbitrary channel with constant cross section and is expressed by multiplication of Fanning friction factor

( $f = \frac{1}{2} \left( \frac{D}{L} \right) \left( \frac{\Delta P}{\rho \langle v \rangle^2} \right)$ ) and Reynolds number ( $Re = \frac{DU\rho}{\mu}$ ) as follows:

$$P_o = \frac{AD_h^2 \Delta p}{2\mu_L Q_L L} \quad (3.28a)$$

It is described by the pressure difference,  $\Delta p$ , channel length,  $L$ , volume flow rate,  $Q_L$ , fluid viscosity,  $\mu_L$ , channel cross sectional area,  $A$ , and hydraulic diameter,  $D_h$ . Flockhart and Dhariwal (1998) calculated the flow rate numerically and determined  $P_o$  with various aspect ratio of trapezoidal channel. In this study, the  $P_o$  with aspect ratio of 0.5 is adopted from their results. Once the  $P_o$  is known the pressure difference of the channel can be calculated readily and applied to the model as

$$P_b = \alpha \rho_L \left( R \ddot{R} + \frac{3}{2} \dot{R}^2 + \frac{1}{2} U_L^2 + \dot{R} U_L \cos \theta \right) + \frac{2\sigma}{R} + \frac{2\mu_L Q_L L P_o}{AD_h^2} + P_{am} \quad (3.28b)^*$$

### 3.7 Bubble detachment

The forces acting on a bubble at a submerged orifice are as follows: the surface tension force,  $F_\sigma$ , the inertia of the fluid surrounding the bubble,  $F_i$ , the gas momentum through an orifice,  $F_M$ , and the drag force,  $F_D$ . The surface tension force, acting along the rim of nozzle, acts as an attaching force. The contribution of buoyancy force to the force balance compared to the other forces especially to the surface tension force is very small and neglected in this modeling.

$$F_\sigma = \pi D_o \sigma \quad (3.29)$$

The inertia force, the upward mass acceleration of the fluid surrounding the bubble, acts as attaching force:

$$F_i = \frac{d}{dt} \left( M' \frac{ds}{dt} \right) \quad (3.30)$$

where  $M'$  is virtual mass of bubble,  $\frac{11}{16} \rho_g V_b$  (Davidson et. al, 1960), and,  $ds/dt$  is the velocity of bubble center away from the nozzle. The momentum flux acts in the direction of injection and acts as detaching force:

$$F_M = \rho_g \frac{Q_o^2}{\pi R_o^2} \quad (3.31)$$

The liquid drag force is acting in the downstream direction.

$$F_D = C_D \frac{1}{2} \rho_L U_L^2 A_{eff} \quad (3.32)$$

where  $C_D$  is the drag coefficient,  $U$  is the velocity of a cross flowing liquid,  $A_{eff}$  is the effective cross sectional area of the bubble over which the drag force acts.

The drag coefficient,  $C_D$ , adopted from White (1991) is a curve-fit formula for the wide range of Reynolds numbers.

$$C_D \approx \frac{24}{Re} + \frac{6}{1 + \sqrt{Re}} + 0.4 \quad 0 \leq Re \leq 2 \times 10^5 \quad (3.33)$$

This can be modified to include the effects on restricted channel flow. The modified drag coefficient is used in the modified model. With all the forces described above, the direction of each force is described in the Figure 3.3.

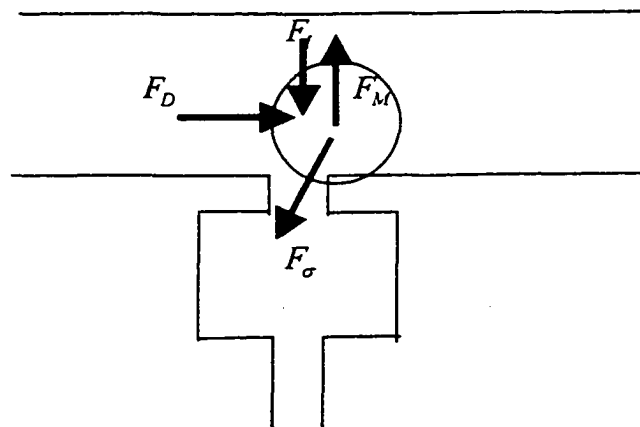


Figure 3.3 Schematic diagram of forces acting on a bubble

The bubble diameter at the detachment will be found from a force balance as

$$F_\sigma = \sqrt{(F_M - F_l)^2 + F_D^2} \quad (3.34)^*$$

### 3.8 Bubble generation modeling

Bubble generation can be modeled by solving equations (3.5), (3.7), (3.14), (3.27), and (3.34). In summary, those equations are described as follows:

(1) Chamber pressure

$$V_c \frac{dP_c}{dt} = k(Q_i - Q_o)P_c \quad (3.5)$$

(2) Gas flow through orifice

$$Q_o = CS_o(P_c - P_b)^{\frac{1}{2}} \quad (3.7b)$$

(3) Bubble growth

$$V_b \frac{dP_b}{dt} + kP_b \frac{dV_b}{dt} = kP_c Q_o \quad (3.14)$$

(4) Pressure balance in the bubble

$$P_b = \alpha \rho_L (R \ddot{R} + \frac{3}{2} \dot{R}^2 + \frac{1}{2} U_L^2 + R U_L \dot{\cos \theta}) + \frac{2\sigma}{R} + P_\infty \quad (3.27)^*$$

In this equation,  $P_\infty$  is the pressure in the liquid channel at the position where the orifice is located and the equation (3.28b) is the final form after the equation (3.28a) is plugged into equation (3.27). These equations contain unknown variables  $P_c$ ,  $P_b$ ,  $R$ ,  $\frac{dR}{dt}$ , and  $\frac{d^2R}{dt^2}$  and the initial conditions must be specified. In this model, the initial conditions are assumed so that the bubble is motionless at time  $t=0$  as follows:

$$P_c = P_b = P_\infty + \frac{2\sigma}{R_0}, \quad R = R_0, \quad \frac{dR}{dt} = \frac{d^2R}{dt^2} = 0 \quad (3.35)^*$$

To generalize the solution, the following non-dimensional variables are chosen as dimensionless chamber pressure  $P_c^* = P_c / P_{ref}$ ; dimensionless bubble pressure  $P_b^* = P_b / P_{ref}$ ; dimensionless pressure around bubble  $P_\infty^* = P_\infty / P_{ref}$ ; dimensionless chamber volume  $V_c^* = V_c / V_{ref}$ ; dimensionless bubble volume  $V_b^* = V_b / V_{ref}$ ; dimensionless gas flow rate into the chamber  $Q_i^* = Q_i / Q_{ref}$ ; dimensionless gas flow rate out through the nozzle  $Q_o^* = Q_o / Q_{ref}$ ; dimensionless surface tension  $\sigma^* = \sigma_L / \sigma_w$ ; dimensionless liquid density  $\rho_L^* = \rho_L / \rho_w$ ; dimensionless gas density  $\rho_g^* = \rho_g / \rho_w$ ; dimensionless time  $t^* = t / T_{ref}$ ; dimensionless radius of bubble  $r^* = r / R_{ref}$ ; dimensionless cross sectional area of nozzle  $S_o^* = S_o / \pi R_{ref}^2$ ; dimensionless liquid flow rate  $U_L^* = U_L / U_{ref}$ . The above equations are rearranged in non-dimensional form as follows:

$$\frac{dP_c^*}{dt^*} = C_1 \frac{kP_c^*}{V_c^*} (Q_i^* - Q_o^*) \quad (3.36)$$

$$Q_o^* = C_2 C_d S_o^* (P_c^* - P_b^*)^{1/2} \quad (3.37)$$

$$\frac{dP_b^*}{dt^*} = k \left( C_3 \frac{P_c^* Q_o^*}{r^{*3}} - C_4 \frac{P_b^*}{r^*} \frac{dr^*}{dt^*} \right) \quad (3.38)$$

$$\frac{d^2 r^*}{dt^{*2}} = C_5 \frac{P_b^* - P_\infty^*}{\alpha \rho_L^* r^{*2}} - \frac{15}{r^*} \left( \frac{dr^*}{dt^*} \right)^2 - C_6 \frac{U_L^{*2}}{2r^*} - C_7 \frac{2\sigma^*}{\alpha r^{*2} \rho_L^*} \quad (3.39)$$

Where the constant terms (  $C_1$  through  $C_7$  ) are

$$C_1 = T_{ref} Q_{ref} / V_{ref}, \quad C_2 = \pi R_{ref}^2 P_{ref}^{1/2} / Q_{ref}, \quad C_3 = \frac{3T_{ref} Q_{ref}}{4\pi R_{ref}^3}, \quad C_4 = 3, \quad C_5 = \frac{T_{ref}^2 P_{ref}}{R_{ref}^2 \rho_w},$$

$$C_6 = \frac{T_{ref}^2 U_{ref}^2}{R_{ref}^2}, \quad C_7 = \frac{T_{ref}^2 \sigma_w}{R_{ref}^3 \rho_w},$$

When the bubble is detached from the nozzle, the force balance equation for the bubble motion is expressed as follows after replacing expressions of each force term in equation (3.34).

$$2\pi R_o \sigma = \sqrt{\left[ \frac{\rho_g Q_o^2}{\pi R_o^2} - \frac{d}{dt} \left( \frac{11}{16} \rho_L V_b \frac{dr}{dt} \right) \right]^2 + \left( \frac{C_D}{2} \rho_L U_L^2 A_{eff} \right)^2} \quad (3.40)$$

Rearrangement of above equation with dimensionless parameters gives

$$\frac{1}{We} = \left[ C_8 \frac{Q_o^{*2}}{U_L^{*2}} - C_9 \frac{1}{U_L^{*2}} \frac{d}{dt^*} \left( V_b^* \frac{dr^*}{dt^*} \right) \right]^2 + C_{10} C_D^2 r^{*4} \quad (3.41)$$

where  $We$  is Weber number ( $We = \rho_L U_L^2 D_{ch} / \sigma$ ) and  $D_{ch}$  is hydraulic diameter of liquid flowing channel.

$$C_8 = \frac{\rho_g Q^2}{2\pi^2 R_o^2 D_{ch} \rho_L U_{ref}^2}, \quad C_9 = \frac{11V_{ref} R_{ref}}{32\pi R_o D_{ch} U_{ref}^2 T_{ref}^2}, \quad C_{10} = \frac{R_{ref}^4}{16R_o^2 D_{ch}^2}$$

With given initial conditions, the equations are solved simultaneously to find the growth of the bubble. The size of the bubble detached from the nozzle is calculated by finding out the bubble size when the force balance equation is satisfied. All these coupled equations are calculated by using ‘Simulink’ by ‘Matlab’ software (The MATH WORKS INC.). The time step for the simulation was 0.01  $\mu$ sec. to minimize the calculation error.

### 3.9 Modified model of bubble detachment condition

To account for the fact that the forming bubble partly blocks the liquid flowing channel, the equations for the bubble detachment condition are modified. The diameter of growing bubble is substituted with effective diameter and the effect of confining wall of liquid channel is taken into consideration. The modified drag coefficient that can reflect this effect is expressed as follows.

$$C_{MD} = \frac{C_D}{1 - \frac{D_{eb}}{D_h}} \quad (3.42)$$

where  $C_{MD}$ ,  $D_{eb}$ , and  $D_h$  is modified drag coefficient, effective bubble diameter, and hydraulic diameter of liquid channel respectively. The only change from the detachment condition equations is that the drag coefficient in equation (3.32) is replaced with equation (3.42).

### 3.10 New model of bubble detachment condition

A new a model with no chamber volume is suggested by the experimental data and simulated with the above model for the smaller bubble production. It is included here for completeness. The same principles described in section 3.1 to 3.6 are used to simulate bubble generation. Instead of employing detachment condition equation (3.34) in 3.7, a new bubble detachment condition is applied as follows.

$$F_\sigma = \sqrt{F_M^2 + F_D^2} \quad (3.43)^*$$

However, an effective velocity (Bird et al., 1960) is introduced that can account for the liquid velocity that increases as the bubble grows because of liquid flow channel restriction. From a mass balance of the liquid as follows:

$$U_{eff} = \frac{U_L A_L}{A_L - A_b} \quad (3.44)$$

where  $U_{eff}$  is effective velocity of the liquid,  $U_L$  is liquid velocity in the channel without the bubble,  $A_L$  is cross sectional area of liquid channel, and  $A_b$  is cross sectional area of forming bubble. In addition, the drag force given by Stokes's law, which has following form, is used.

$$F_D = 6\pi R_b \mu U_{eff} \quad (3.45)$$

In addition, it is assumed as a first approximation that the gas in the bubble is incompressible and has the following relation with the gas flow rate out of the orifice into the bubble.

$$Q_o = V_B / t \quad (3.46)$$

Therefore, the new model equations are expressed as

$$\pi D_o \sigma = \left\{ \left( \frac{\rho_g Q_o^2}{\pi R_o^2} \right)^2 + \left[ \frac{1}{2} \rho_L \left( \frac{U_L A_L}{A_L - A_b} \right)^2 \frac{\pi D_b^2}{4} \frac{C_D}{1 - \frac{D_{eb}}{D_h}} \right]^2 \right\}^{\frac{1}{2}} \quad (3.47)*$$

This model is programmed with Simulink by Matlab and listed in appendix E.

## CHAPTER 4

### EXPERIMENTAL APPARATUS

Evaluation of a theoretical model requires comparison with experimental data. Therefore, the main object of this experiment is to acquire the smallest possible bubbles and their behaviors under controlled liquid and gas flow rates. Still photography was used to determine the mean bubble diameter and gain insight into the phenomena governing the bubble formation.

#### 4.1 Apparatus design

Experimental channels were designed with the primary objectives of generating bubbles in micrometer range with low liquid to bubble volume ratio for the potential use as a blood oxygenator that can be directly applied to the blood stream. The apparatus basically consists of two channels. A trapezoidal channel of 100  $\mu\text{m}$  width and 30  $\mu\text{m}$  in depth was designed for liquid flow. Perpendicular to this channel, a thin channel of 6  $\mu\text{m}$  width and 15 mm length is etched for gas flow. A small chamber at the end receives gas flow. The schematic diagram is in Figure 4.1.

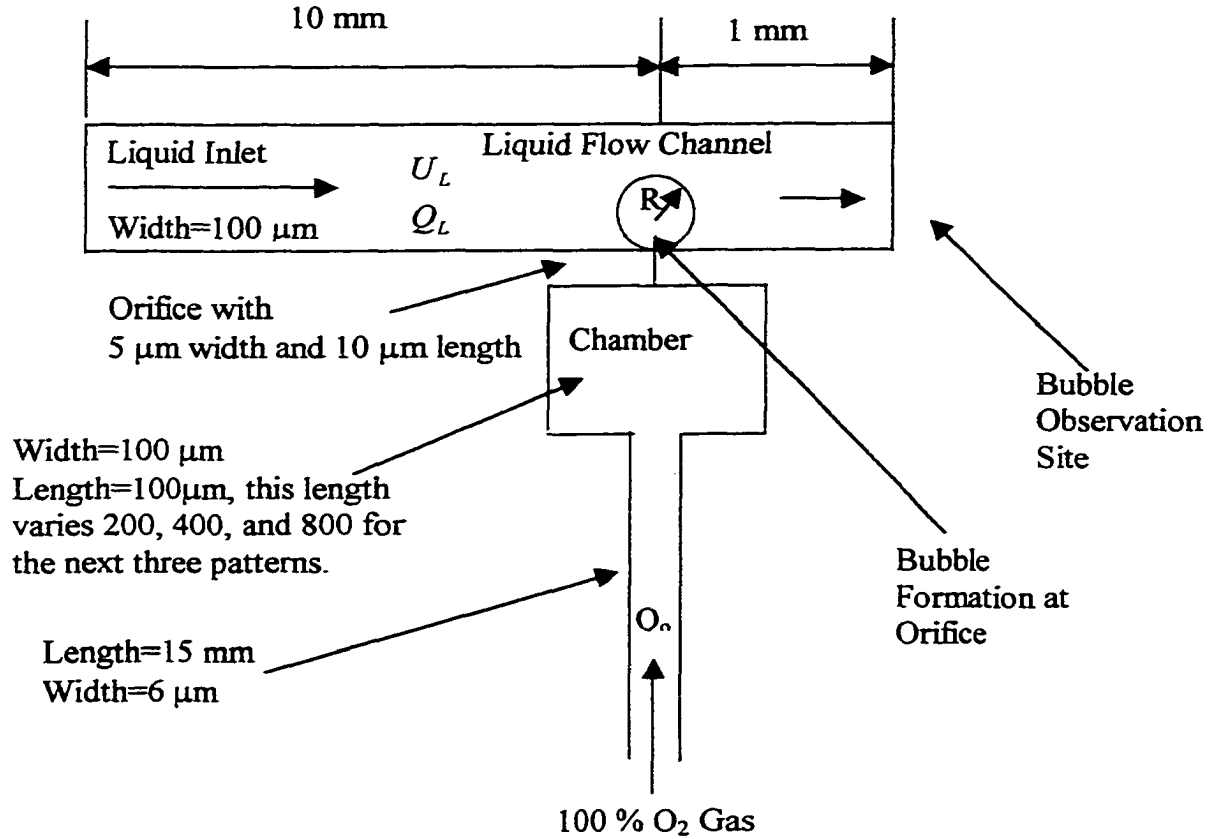


Figure 4.1 Schematic diagram of the final microchannel device and identification of bubble formation and observation sites

See section 4.6 for shortened liquid channel

#### 4.2 Microchannel fabrication

To produce microbubbles, the orifice and the channels were designed and fabricated on silicon wafer. This construction of the microchannel was made possible by photolithography process (Madou, 1997).

Eight sets of apparatus were prepared to be used as microbubbles generator. The small chambers have 100  $\mu\text{m}$  width, 30  $\mu\text{m}$  depth and 100, 200, 400, and 800  $\mu\text{m}$  in length. After the apparatus were etched, the orifices were machined by a focused ion beam (FIB) (Madou, 1997) and covered with Pyrex glass. This covered glass was

bonded by anodic bonding (Albaugh, 1992) on the top of each fabricated channel. Finally, PVC tubes were attached at each inlet of liquid and gas with epoxy resin.

#### 4.2.1. Mask Generation

In general, optical masks are made from glass plates covered with hard-surface materials such as chromium or iron oxide. In this experiment, patterns on chromium covered glass plate was made by University of Cincinnati and used as a mask for the optical lithography process. The area for the orifice was left without any pattern for the focused ion beam machining later.

The mask was printed on a 100 mm diameter silicon wafer. Each mask contains 4 patterns with different length of channels with various volumes. The alignment of the pattern is in Figure 4.2.

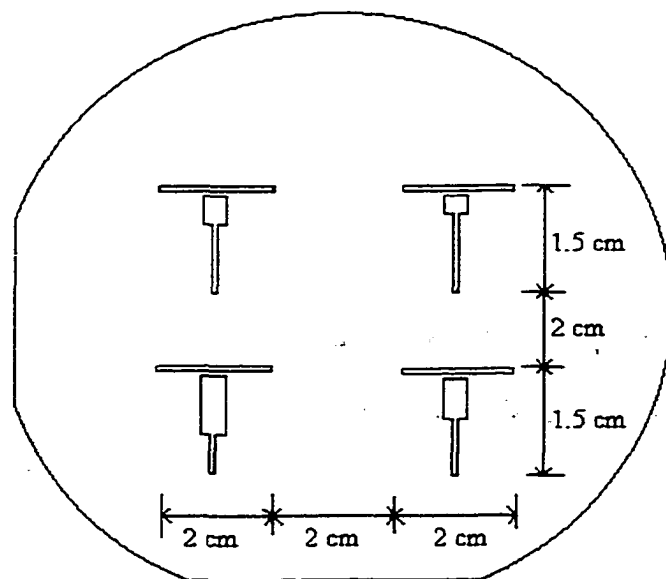


Figure 4.2 Alignment of patterns

#### 4.2.2. Resist

Photoresist is a chemical substance containing a light-sensitive material suspended in a solvent. There are two types of resists: positive and negative. In this experiment, positive photoresist (S1811) was used. It reacts with ultraviolet lights and becomes soluble in basic solutions. Therefore, the part of the film not shadowed is dissolved away, leaving only the shadowed part.

During the application of the photoresist, the wafer was held on a vacuum chuck. The photoresist was applied until  $\frac{2}{3}$  of the wafer surface area was covered. Then the wafer was spun with 20 seconds of acceleration period and a final speed of 3000 rpm for 40 seconds.

After coating, the wafer was soft baked to remove the solvent from the photoresist and improve adhesion of resist to the wafer. For this process, the wafer was put into the oven at 85 °C for 20 minutes.

#### 4.2.3. Mask exposure and printing

Optical resists are sensitive to light of 300 to 500 nm in wavelength, a range that includes visible violet and blue light. Therefore, the mask was exposed to a mercury vapor lamp (UV light), which produced the highest intensity near 365 nm where the sensitivity of positive photoresist is maximum. The UV light was warmed up about one hour before use.

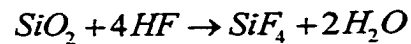
The contacting printing method was used for this exposure because it was the simplest way to transfer a mask image to a substrate which gives good resolution.

#### 4.2.4. Developing

After exposure, the wafer was put into the developer solution. Positive development was followed by a water rinse to remove the developer and spinning to remove the water. The wafer was hard baked after developing to harden the photoresist and improve adhesion at 130 °C for 20 minutes.

#### 4.2.5. Etching the oxide layer

To etch the oxide layer, the wafer was put into the hydrofluoric acid solution. The reaction is



Generally, the HF is buffered with NH<sub>4</sub>F, ammonium fluoride with the volume ratio of six or seven parts NH<sub>4</sub>F to one part HF. This mixture is called buffered oxide etch (BOE) and etches oxide selectively. In addition, BOE reduces the attack of HF on photoresist. The wafer was put into BOE with oxide side up using tweezers about 1 minute. Then the wafer was put into the stop bath that contains water, rinsed in running water and examined.

#### 4.2.6. Photoresist removal

The silicon dioxide pattern was obtained after etching since the BOE did not etch silicon and the photoresist pattern. Next, the photoresist that was covered on the wafer surface was removed. The 1165 remover was used to remove resist. Two baths of

removers were prepared. In the first bath the wafer was put in for 3 minutes and checked to remove the bulk of photoresist. This process was repeated until the bulk of resist was removed. Any remaining traces of photoresist were removed in the second bath.

#### 4.2.7. Si etching

After being rinsed in running water and dried, the wafer was inspected to check for an even, clear color for the oxide covered area as well as the clear and gray color for the silicon area. The wafer was then put into an anisotropic wet etching with KOH.

In this preparation, it is decided to use KOH etching on a  $\langle 100 \rangle$  wafer. A  $\langle 100 \rangle$  silicon wafer has four convergent self-limiting  $\langle 111 \rangle$  etch planes 54.74 degrees to the surface plane of the wafer. These  $\langle 111 \rangle$  low etch rate planes are 90 degree to each other and define the angular sidewalls of the anisotropically etched cavity.

With 100  $\mu\text{m}$  of  $\text{SiO}_2$  mask opening, it took about 30 minutes to etch 30  $\mu\text{m}$  depth trench on silicon at 50°C with KOH. The  $\langle 111 \rangle$  low etch plane made the trench converges to the bottom. This etching process resulted in the 57.58  $\mu\text{m}$  width at the bottom.  $\text{SiO}_2$  is also being etched with the rate of  $14 \text{ \AA} / \text{min}$ . Etching of oxide mask for 10 minutes would result in widening of opened is for 0.14  $\mu\text{m}$ . The final shape of the trench is shown in Figure 4.3.

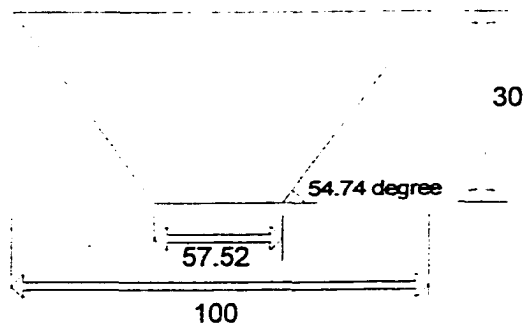


Figure 4.3. Cross sectional dimension of the etched trench (units in  $\mu\text{m}$ )

#### 4.2.8. Removal of oxide layer

After etching the trenches, the oxide layer was removed by using HF with the same manner as described above.

#### 4.2.9. Orifice

The spaces between the gas and the liquid channels were machined by a focused ion beam with  $5 \mu\text{m}$  in depth and width to make an orifice. A focused ion beam was applied directly to create structures by sputtering silicon from a surface. The typical shape of orifice machined on the channel is shown in Figure 4.4.

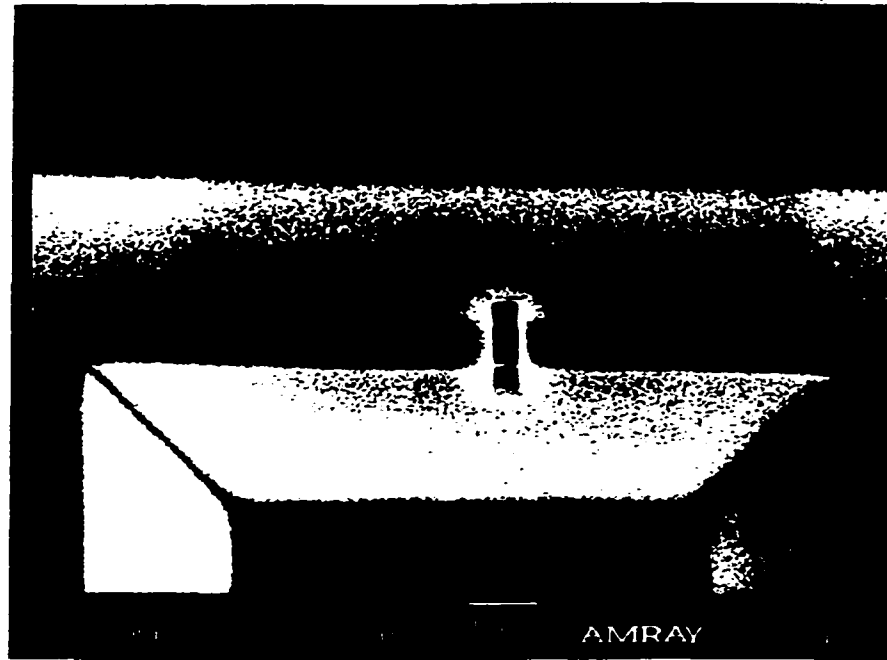


Figure 4.4 Scanning electron microscopy picture of orifice with  $5\ \mu\text{m}$  width and  $4.5\ \mu\text{m}$  depth which is micromachined by Focused Ion Beam (950X magnification)

#### 4.2.10 Glass cover

Square Pyrex windows with 2cm long and 0.5 cm thick were prepared to cover the channels. Each glass block was bonded anodically on the top of the channel.

### 4.3 Anodic bonding

Anodic bonding, also referred to as field-assisted glass silicon sealing is a process that permits the bonding of silicon to glass well below the softening temperature of the glass. The pieces to be bonded are assembled and heated on a oven in a room atmosphere to temperature about  $500\ ^\circ\text{C}$ . A D.C. voltage about 1000 volts is applied across the two electrodes.

The mechanism involved in the bonding process is attributed to mobile ions in the glass. At an elevated temperature the positive sodium ions in the glass have an increased mobility and are attracted to the negative electrode on the glass surface. After the sodium ions have moved toward the surface, a large potential drop occurs at the glass / anode interface. The resulting electric field between the surfaces pulls them into contact. A higher voltage is needed for a good bonding if lower temperatures are applied.

For this process, Pyrex pieces with thickness of 1 mm were purchased from Esco Products of Oak Ridge, NJ. A one inch square piece of Pyrex was cut into four half inch square pieces.

#### 4.3.1 Cleaning

It is critical to have clean pieces for successful bonding. The silicon and Pyrex were put into sulfuric / nitric acid bath for cleaning and rinsed with acetone and isopropyl alcohol repeatedly.

#### 4.3.2 Mate

They were put together under the clean hood with small drop of deionized water to help them hold together. Mated pieces then moved to the oven.

#### 4.3.3 Bonding

The pieces were put into the oven with two metal plates. The bottom plate, on the top of insulated ceramic lining of oven, was larger and connected to the positive

electrode. The top plate with smaller size was connected to the negative electrode. The setup was in the sequence as follows, starting from the bottom: metal plate with positive electrode, silicon, glass, and metal plate with negative electrode. The electrodes were connected to the high voltage D.C. power supply. The schematic set up is in Figure 4.5.

The oven temperature was increased to 500 ° C with the power supply of 1000 V. The pieces were left in the oven for 1 and 1/2 hours until the power and oven were turned off and left there to cool down

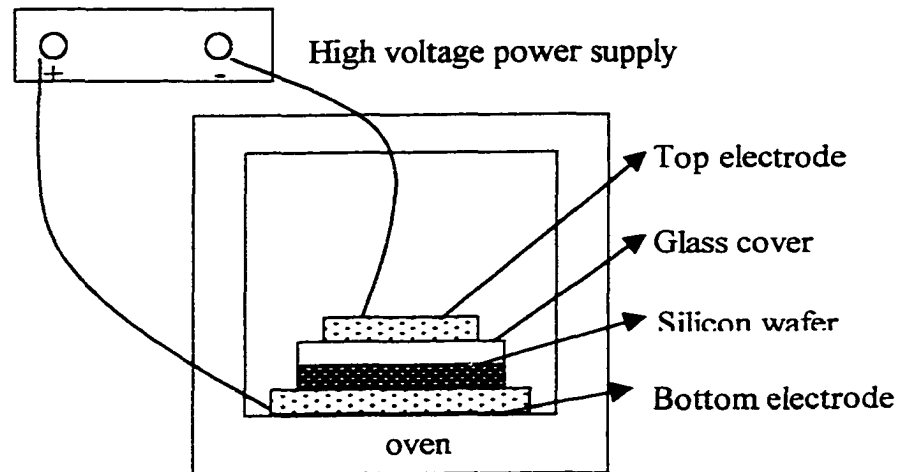


Figure 4.5 Apparatus used for anodic bonding

#### 4.3.4 Examination of bonding

After the oven cooled down, the wafer bonded with glass were pulled out and examined under microscope.

UNIVERSITY OF  
 SOUTH ALABAMA  
 LIBRARY

#### 4.4 Liquid flow in the channel

The fluid supply shown in Figure 4.1 provides a controlled flow rate of liquid into the channel. A 0.5  $\mu\text{m}$  filter was used to remove potentially clogging particles from the liquid before entering the channel. A range of liquid velocity is restricted from 0.5 ml to 3 ml per hour, and this small quantity of flow rates was controlled by syringe pump (KD Scientific Model 100 series). Distilled water was selected as the test fluid. Oxygen gas was used for gas flow into the channel to make bubbles and flow rates were controlled by pressure regulator. The pressure variation for gas flow rate is restricted from zero to 50 psi. The upper limit was selected to prevent a possible burst of gas through the tubing.

#### 4.5 Photograph and measurement system

Accurate bubble size measurements were possible by using an optical microscope (Leitz™ Laborlux D) with digital camera (Quantix™ by Photometrics) attached to it. The microscope was set to have 200 times magnification and the image was imported into a computer (Gateway 2000, Pentium pro 200). Then the image was measured by counting the number of pixels in the monitor. The calibration was done by using standard glass specimen with a scaled pattern of 1 mm in length with 100 spacings.

To illuminate bubbles forming in the liquid channel outlet, a stroboscopic light source (Mini Strobe / Flasher by Radio Shack, Cat. No. 42-3048) was installed at the opposite side of microscope to the bubbling site and illustrated in Figure 4.6. The exposure time for the camera to capture the bubbling image was set to 80 ns.

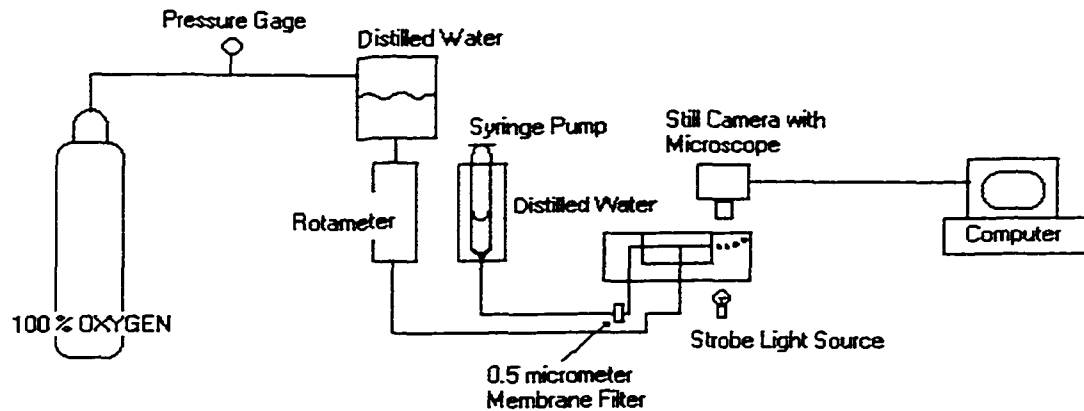


Figure 4.6 Experimental set up for bubble formation and imaging system

#### 4.6 Liquid channel modification

During the experiments, crosscurrent liquid flow channels 2 cm long produced high pressure and inhibited bubble formation. According to equation (3.29), the pressure at the orifice site reached up to  $6 \times 10^4 \text{ N/m}^2$  when liquid flow rate increased to 3 ml/hr. The liquid channel length needed to be reduced and was done by using silicon carbide grinding tip. The end part of liquid channel was ground off until the distance between the orifice and the outlet reached less than 1 mm. Consequently, the pressure at the orifice site reduced more than ten folds ( $5 \times 10^3 \text{ N/m}^2$ ). The final dimensions of these channels are listed in table 4.1.

Table 4.1 Dimensions of chambers and orifices used in experiments for microbubble production

| Apparatus | Orifice Dimension *<br>(micrometer) | Chamber Dimension **<br>(micrometer) | Distance***<br>(micrometer) |
|-----------|-------------------------------------|--------------------------------------|-----------------------------|
| 1A        | 5 X 13.4 X 10                       | 100 X 100 X 29                       | 0.8                         |
| 1B        | 5 X 13.4 X 10                       | 104 X 200 X 28                       | 0.75                        |
| 1C        | 5 X 13.4 X 6.3                      | 103 X 400 X 28                       | 0.79                        |
| 2A        | 5 X 16.6 X 4.5                      | 100 X 100 X 29                       | 0.8                         |
| 2B        | 5 X 16.6 X 3.2                      | 104 X 200 X 28                       | 0.75                        |
| 2C        | 5 X 16.6 X 3                        | 103 X 400 X 28                       | 0.79                        |
| 2D        | 5.3 X 15.4 X 4.8                    | 102 X 800 X 29.3                     | 0.8                         |

\* Orifice dimension represents width x length x depth

\*\* Channel dimension represents width x length x depth (with error of less than ! 1 %)

\*\*\*Distance from orifice to the channel exit

## CHAPTER 5

### RESULTS

#### 5.1 General description of bubble formation

Bubbles were observed at the observation site shown in Figure 4.1. Because the observation site is not the bubble formation site, the bubbles observed are 0.3 to 0.9 milliseconds old.

In all cases, there existed a minimum gas flow rate, below which the bubble formation was in an intermittent pattern. There was relatively long dormant period where there was no gas flow through the orifice. As the chamber pressures built up, the pressure became high enough to overcome surface tension and form the bubble. For a small chamber volume, a single bubble was formed. However, a group of bubbles with various sizes was formed for large chamber volume.

With the liquid flow rate below 0.5 ml/hr, the bubble formation was not uniform regardless of gas flow rate range applied in this experiment. At this condition, the formed bubble was not detached from the orifice or attached on the liquid channel and coalesced with the next forming bubble. This phenomenon became apparent as gas flow rate increased.

At liquid flow rate of 1 ml/hr to 3 ml/hr, the dormant period was decreased as the gas flow rate increased and bubble size became uniform for small chamber volume

Figure 5.1a shows bubble generation with uniform size of  $45\ \mu\text{m}$  diameter bubble in gas flow rate of  $1/100000\ \text{cm}^3/\text{sec}$  with liquid flow rate of  $1\ \text{ml/hr}$ . As the gas flow rate increased from  $1/100000$  to  $1.5/100000\ \text{cm}^3/\text{sec}$ , the bubbling frequency is increased without changing the bubble size (Figure 5.1b). As the liquid flow rate increased from  $1\ \text{ml/hr}$  (Figure 5.1b) to  $2\ \text{ml/hr}$ , the bubble size was independent of the liquid flow rate for a given gas flow rate. Figure 5.2 shows bubble generation at increased liquid flow rate. The bubbles formed singly; they were regularly spaced and very uniform in size for the small chamber volume. As the gas flow rate increased further from the condition in Figure 5.2, bubble formation became chaotic and various sizes of bubbles were formed (Figure 5.3). Transition to this non-uniform size bubble formation regime was difficult to quantify.

On further increasing the liquid flow rate above  $4\ \text{ml/hr}$ , the bubble formed in non-uniform manner. Double bubble was formed at low gas flow rate (Figure 5.4) compare to Figure 5.1b and became non-uniform as the gas flow rate increased (Figure 5.5) compare to Figure 5.4. Further increase of liquid flow rate made the liquid flow into the chamber through orifice.

For a large chamber volume, bubbles with uniform size could not be produced regardless of gas and liquid flow rate. Figure 5.6 shows typical un-uniform bubble formation from large chamber volume. At the increased liquid flow rate, double bubbles are formed at similar gas flow rate that produce un-uniform bubble (Figure 5.7). The bubble sizes become inhomogeneous as the gas flow rate increased further from the condition of Figure 5.7.

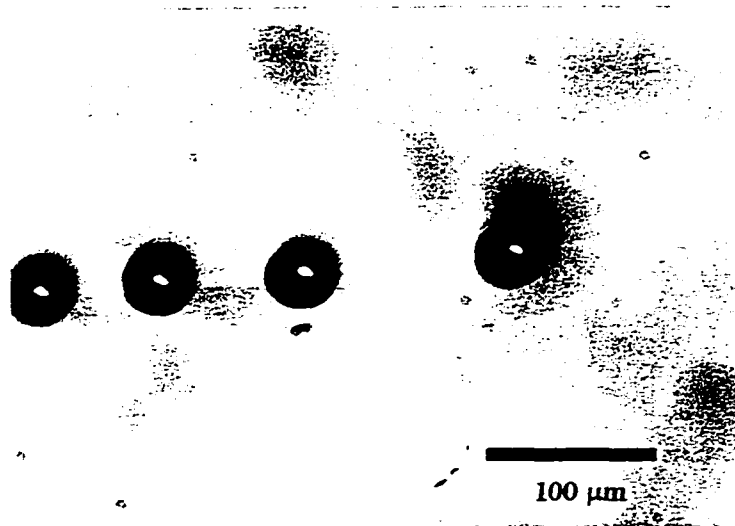


Figure 5.1 (a) Bubble formation at two different gas flow rates with  $2.5 \times 10^{-7} \text{ cm}^3$  of chamber volume.

$Q_i = 1.0 \times 10^{-5} \text{ cm}^3 / \text{sec}$ ,  $Q_L = 1 \text{ ml/hr}$ , and  $D_o = 4.2 \mu\text{m}$   
(bubble diameter =  $45 \mu\text{m}$ )

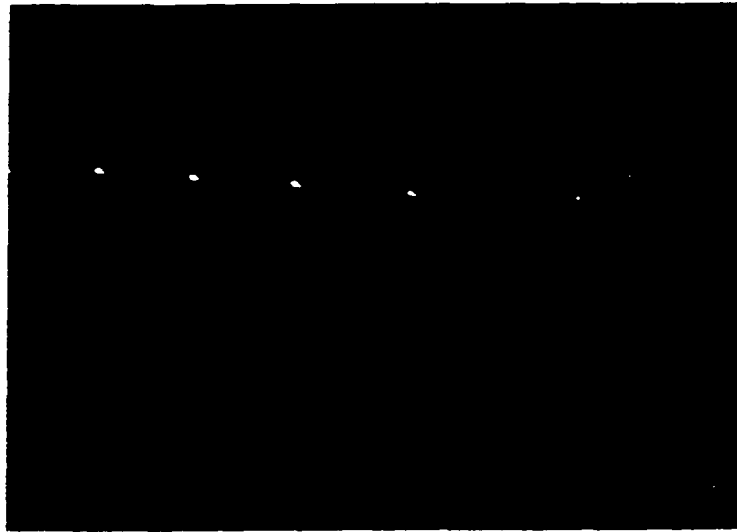


Figure 5.1 (b) Bubble formation at two different gas flow rates with  $2.5 \times 10^{-7} \text{ cm}^3$  of chamber volume.

$Q_i = 1.5 \times 10^{-5} \text{ cm}^3 / \text{sec}$ ,  $Q_L = 1 \text{ ml/hr}$ , and  $D_o = 4.2 \mu\text{m}$   
(bubble diameter =  $43 \mu\text{m}$ )

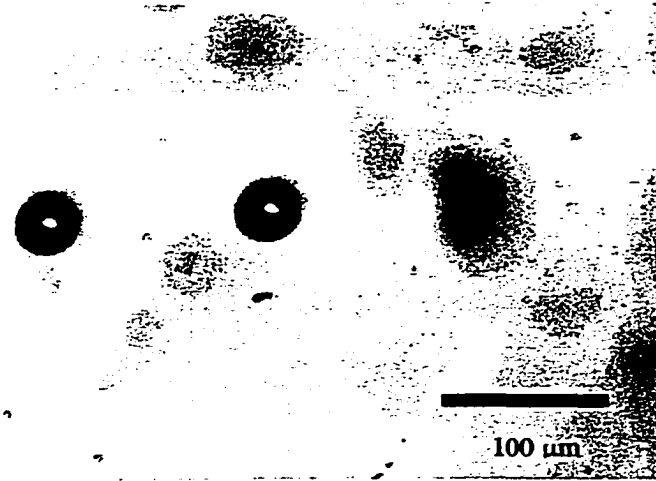


Figure 5.2 Bubble formation at  $Q_i = 1.4 \times 10^{-5} \text{ cm}^3 / \text{sec}$ ,  $Q_L = 2 \text{ ml/hr}$ , and  $D_o = 4.2 \mu\text{m}$  with  $2.5 \times 10^{-7} \text{ cm}^3$  of chamber volume (bubble diameter =  $43 \mu\text{m}$  )

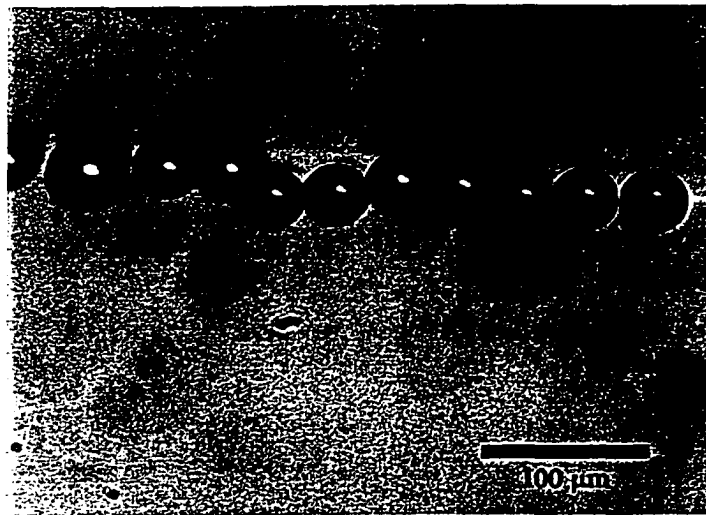


Figure 5.3 Bubble formation at  $Q_i = 4 \times 10^{-5} \text{ cm}^3 / \text{sec}$ ,  $Q_L = 2 \text{ ml/hr}$ , and  $D_o = 4.2 \mu\text{m}$  with  $2.5 \times 10^{-7} \text{ cm}^3$  of chamber volume ( bubble diameter =  $52, 42 \mu\text{m}$  )

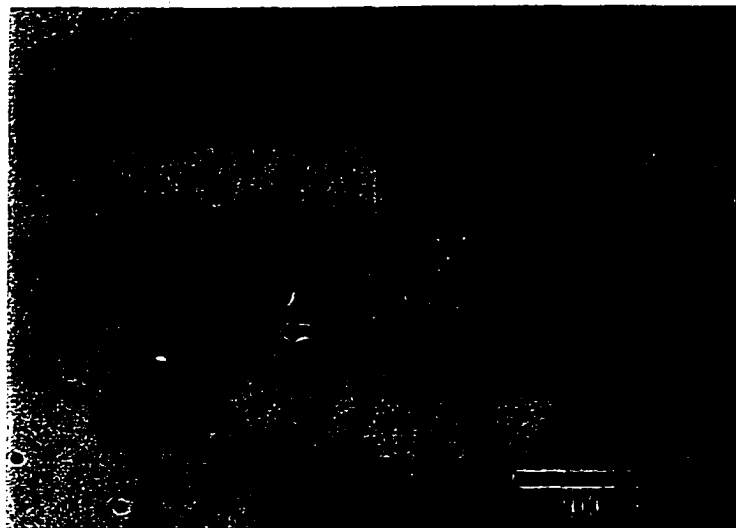


Figure 5.4 Bubble formation at  $Q_i = 1.4 \times 10^{-5} \text{ cm}^3 / \text{sec}$ ,  $Q_L = 4 \text{ ml/hr}$ , and  $D_o = 4.2 \mu\text{m}$   
with  $2.5 \times 10^{-7} \text{ cm}^3$  of chamber volume  
( bubble diameter =  $41 \mu\text{m} + 30 \mu\text{m}$  )

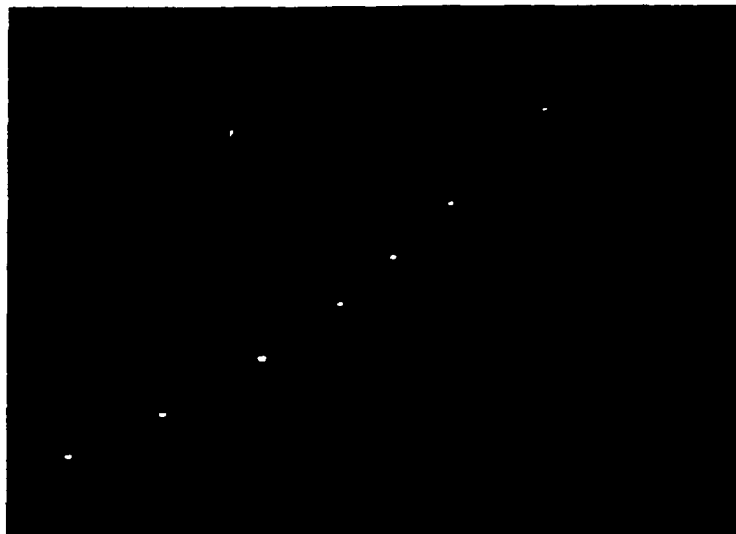


Figure 5.5 Bubble formation at  $Q_i = 1.8 \times 10^{-5} \text{ cm}^3 / \text{sec}$ ,  $Q_L = 4 \text{ ml/hr}$ , and  $D_o = 4.2 \mu\text{m}$   
with  $2.5 \times 10^{-7} \mu\text{m}^3$  of chamber volume  
( bubble diameter = 58, 57.6, 58, 46, 46, 46, 45  $\mu\text{m}$  from left to right )

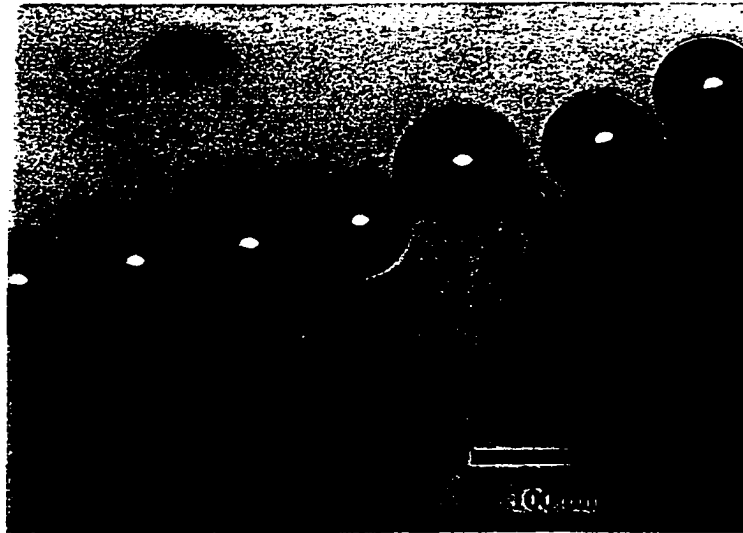


Figure 5.6 Bubble formation at  $Q_i = 2.5 \times 10^{-5} \text{ cm}^3 / \text{sec}$ ,  $Q_L = 1 \text{ ml/hr}$ ,  $D_o = 4 \text{ }\mu\text{m}$ , with  $10 \times 10^{-7} \text{ }\mu\text{m}^3$  of chamber volume  
( bubble diameter = 67, 68, 68, 74, 68  $\mu\text{m}$  from the left to right )

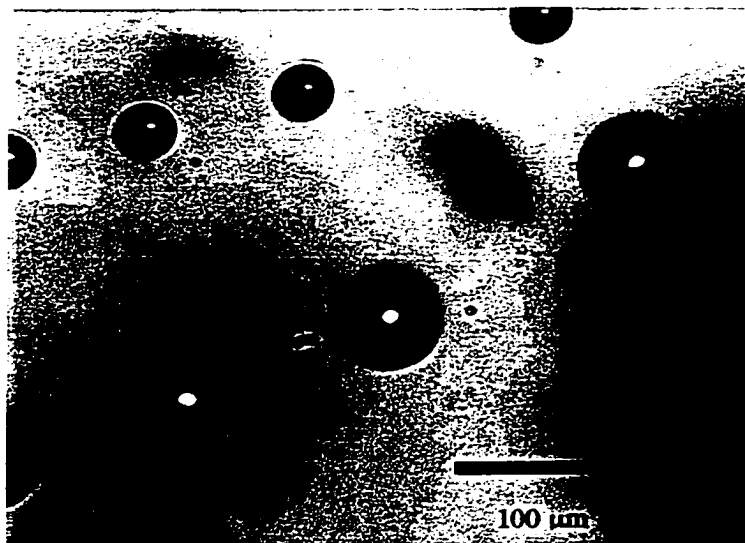


Figure 5.7 Bubble formation at  $Q_i = 2.4 \times 10^{-5} \text{ cm}^3 / \text{sec}$ ,  $Q_L = 3 \text{ ml/hr}$ ,  $D_o = 4 \text{ }\mu\text{m}$ , with  $10 \times 10^{-7} \text{ }\mu\text{m}^3$  of chamber volume  
( bubble diameter = 36 + 66  $\mu\text{m}$  )

As a result, there was a distinct influence of chamber volume. For small chamber volumes, there were no significant influences of orifice diameters to the bubble size.

## 5.2 Bubble size measurements

In Table 5.1, the mean bubble size and its standard deviation for different gas and liquid flow rate were examined with apparatus 1A, 2A, 2B, and 2C (Table 4.1). They have chambers with volumes of  $2.5 \times 10^{-7} \mu\text{m}^3$ ,  $2.5 \times 10^{-7} \mu\text{m}^3$ ,  $5 \times 10^{-7} \mu\text{m}^3$ , and  $10 \times 10^{-7} \mu\text{m}^3$  respectively. Hydraulic diameter of the orifice varies from  $4 \mu\text{m}$  to  $6.6 \mu\text{m}$  and specified in the Table. The formed bubbles were analyzed by digital camera with a computer and calibrating software described in previous chapter.

Table 5.1 Bubble size measurements with apparatus 1A for different liquid and gas flow rates ( $2.5 \times 10^{-7} \mu\text{m}^3$  of chamber volume)

| Experiment Number | Orifice Diameter $D_o$ | Liquid Flow Rate (ml/hr) $Q_L$ | Gas Flow Rate (ml/sec X 100000) $Q_i$ | Bubble Diameter ( $\mu\text{m}$ ) $D_b$ | Standard Deviation |
|-------------------|------------------------|--------------------------------|---------------------------------------|---|--------------------|
| 1A-1 (n=15)       | 6.6                    | 1                              | 1.2                                   | 45.37                                   | 0.39               |
| 1A-2 (n=14)       | 6.6                    | 1                              | 2.1                                   | 45.46                                   | 0.42               |
| 1A-3 (n=14)       | 6.6                    | 1                              | 1                                     | 50.65                                   | 4.65               |
| 1A-4 (n=7)        | 6.6                    | 1.5                            | 0.9                                   | 47.82                                   | 4.75               |
| 1A-5 (n=8)        | 6.6                    | 1.5                            | 1                                     | 54.17                                   | 0.26               |
| 1A-6 (n=13)       | 6.6                    | 2                              | 1.1                                   | 45.03                                   | 0.39               |
| 1A-7 (n=12)       | 6.6                    | 2                              | 1.3                                   | 45.63                                   | 0.46               |
| 1A-8 (n=12)       | 6.6                    | 2                              | 1.9                                   | 45.83                                   | 0.36               |
| 1A-9 (n=10)       | 6.6                    | 2                              | 1                                     | 49.24                                   | 5.55               |
| 1A-10 (n=12)      | 6.6                    | 3                              | 1                                     | 45.25                                   | 0.40               |
| 1A-11 (n=12)      | 6.6                    | 3                              | 1.5                                   | 46.21                                   | 0.58               |
| 1A-12 (n=9)       | 6.6                    | 3                              | 1.1                                   | 50.93                                   | 5.2                |

n = number of bubbles

Table 5.2 Bubble size measurements with apparatus 2A for  
different liquid and gas flow rates  
(  $2.5 \times 10^{-7} \mu\text{m}^3$  of chamber volume )

| Experiment Number | Orifice Diameter | Liquid Flow Rate (ml/hr) | Gas Flow Rate (ml/sec X 100000) | Bubble Diameter ( $\mu\text{m}$ ) | Standard Deviation |
|-------------------|------------------|--------------------------|---------------------------------|-----------------------------------|--------------------|
| 2A-1 (n=11)       | 4.2              | 0.5                      | 1.6                             | 45.49                             | 0.31               |
| 2A-2 (n=9)        | 4.2              | 0.5                      | 0.9                             | 47.22                             | 0.23               |
| 2A-3 (n=12)       | 4.2              | 0.5                      | 1.7                             | 45.2                              | 0.44               |
| 2A-4 (n=12)       | 4.2              | 0.5                      | 1.2                             | 65.42                             | 14.23              |
| 2A-5 (n=12)       | 4.2              | 0.5                      | 1.4                             | 56.6                              | 0.26               |
| 2A-6 (n=12)       | 4.2              | 1                        | 0.7                             | 45.23                             | 0.34               |
| 2A-7 (n=15)       | 4.2              | 1                        | 1.1                             | 45.07                             | 0.44               |
| 2A-8 (n=9)        | 4.2              | 1                        | 1.8                             | 46.84                             | 0.21               |
| 2A-9 (n=8)        | 4.2              | 1                        | 1.8                             | 44.18                             | 0.16               |
| 2A-10 (n=11)      | 4.2              | 1                        | 2.1                             | 48.14                             | 0.32               |
| 2A-11 (n=8)       | 4.2              | 1                        | 2.5                             | 54.95                             | 12.51              |
| 2A-12 (n=13)      | 4.2              | 1                        | 2.5                             | 47.94                             | 0.56               |
| 2A-13 (n=11)      | 4.2              | 1                        | 1                               | 47.1                              | 0.23               |
| 2A-14 (n=12)      | 4.2              | 1                        | 1                               | 48.44                             | 0.50               |
| 2A-15 (n=13)      | 4.2              | 2                        | 0.9                             | 45.78                             | 0.60               |
| 2A-16 (n=7)       | 4.2              | 2                        | 1                               | 43.6                              | 0.27               |
| 2A-17 (n=12)      | 4.2              | 2                        | 1.4                             | 45.25                             | 0.31               |
| 2A-18 (n=13)      | 4.2              | 2                        | 1.5                             | 45.66                             | 0.26               |
| 2A-19 (n=12)      | 4.2              | 2                        | 1.6                             | 48.5                              | 0.30               |
| 2A-20 (n=9)       | 4.2              | 2                        | 1.7                             | 44.99                             | 0.43               |
| 2A-21 (n=11)      | 4.2              | 2                        | 1.8                             | 46.12                             | 0.34               |
| 2A-22 (n=9)       | 4.2              | 2                        | 2.2                             | 48.15                             | 0.30               |
| 2A-23 (n=9)       | 4.2              | 2                        | 2.6                             | 47.3                              | 0.38               |
| 2A-24 (n=10)      | 4.2              | 3                        | 0.86                            | 45.17                             | 0.26               |
| 2A-25 (n=8)       | 4.2              | 3                        | 1                               | 45.44                             | 0.22               |
| 2A-26 (n=9)       | 4.2              | 3                        | 1                               | 44.17                             | 0.42               |
| 2A-27 (n=10)      | 4.2              | 3                        | 1.2                             | 44.83                             | 0.45               |
| 2A-28 (n=9)       | 4.2              | 3                        | 1.4                             | 45.14                             | 0.25               |
| 2A-29 (n=11)      | 4.2              | 3                        | 1.5                             | 46.88                             | 0.22               |
| 2A-30 (n=13)      | 4.2              | 3                        | 1.5                             | 47.19                             | 0.30               |

n = number of bubbles

Table 5.3 Bubble size measurements with apparatus 2B for  
different liquid and gas flow rates  
(  $5 \times 10^{-7} \mu\text{m}^3$  of chamber volume )

| Experiment Number | Orifice Diameter | Liquid Flow Rate (ml/hr) | Gas Flow Rate (ml/sec X 100000) | Bubble Diameter ( $\mu\text{m}$ ) | Standard Deviation |
|-------------------|------------------|--------------------------|---------------------------------|-----------------------------------|--------------------|
| 2B-1 (n=17)       | 4                | 1                        | 1.5                             | 63.8                              | 1.45               |
| 2B-2 (n=17)       | 4                | 2                        | 1.3                             | 62.62                             | 2.71               |
| 2B-3 (n=13)       | 4                | 3                        | 1.2                             | 62.58                             | 4.12               |
| 2B-4 (n=14)       | 4                | 1                        | 1.8                             | 64.14                             | 2.04               |
| 2B-5 (n=14)       | 4                | 2                        | 1.6                             | 63.69                             | 2.69               |
| 2B-6 (n=14)       | 4                | 3                        | 1.5                             | 59.5                              | 11.98              |
| 2B-7 (n=8)        | 4                | 1                        | 4                               | 95.57 +<br>33.16                  | 2.71 + 3.82        |
| 2B-8 (n=7)        | 4                | 2                        | 4                               | 94.74 +<br>18.4                   | 0.54 + 0.83        |
| 2B-9 (n=5)        | 4                | 3                        | 4                               | 65.28                             | 17.11              |

n = number of bubbles

Table 5.4 Bubble size measurements with apparatus 2C for  
Different liquid and gas flow rates  
(  $10 \times 10^{-7} \mu\text{m}^3$  of chamber volume )

| Experiment Number | Orifice Diameter | Liquid Flow Rate (ml/hr) | Gas Flow Rate (ml/sec X 100000) | Bubble Diameter ( $\mu\text{m}$ ) | Standard Deviation |
|-------------------|------------------|--------------------------|---------------------------------|-----------------------------------|--------------------|
| 2C-1 (n=13)       | 4                | 1                        | 1.3                             | 80.13                             | 5.97               |
| 2C-2 (n=12)       | 4                | 1                        | 1.8                             | 67.19                             | 1.05               |
| 2C-3 (n=4)        | 4                | 2                        | 1.9                             | 71.79 +<br>36.69                  | 1.55 + 0.72        |
| 2C-4 (n=12)       | 4                | 2                        | 1.1                             | 80.58                             | 2.2                |
| 2C-5 (n=10)       | 4                | 3                        | 1.1                             | 81.94                             | 3.29               |
| 2C-6 (n=10)       | 4                | 3                        | 2                               | 78.53                             | 2.86               |

n = number of bubbles

For one to have better understanding of the trend in bubble formation, across all the previous Tables, the data was subjected to multiple linear regression and the

influences of parameters (chamber volume, orifice diameter, liquid flow rate, and gas flow rate) to the final bubble size are expressed by the following relationship,

$$D_b = 33.94 + 4.78 \times 10^{-5} V_c + 0.34 D_o - 0.147 \times 10^{-9} Q_L + 0.135 \times 10^{-7} Q_g \quad (5.1)$$

where all the units are in  $\mu m$ ,  $\mu m^3$ , and  $\mu m^3 / \text{sec}$  with  $R^2=0.943$  (amount of variability in bubble diameter that can be explained by the variables). The residuals are plotted in the Figure 5.8.

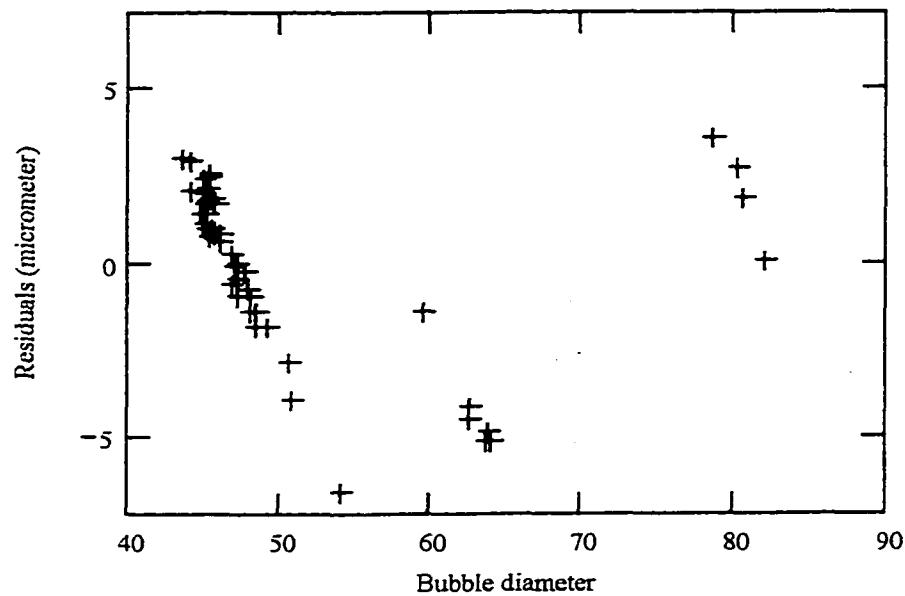


Figure 5.8 Residual plot of regression model

The residual plot in Figure 5.8 shows that most of the experimental data is within  $\pm 4 \mu m$  of the regression model. The sensitivity of bubble diameter is calculated by holding all the parameters constant except one which is increased by one hundred percent, and the result change in output is shown in Table 5.5. Un-uniform residual distribution indicates

that the higher order regression model is required for further investigation. Higher order regression could be adequate but not important for the conclusion of this study and left for future work.

Table 5.5 The sensitivity of bubble diameter to chamber volume, orifice diameter, liquid flow rate, and gas flow rate, based on regression

| parameter       | $V_c$ ( $\mu\text{m}^3$ ) | $D_0$ ( $\mu\text{m}$ ) | $Q_L$ ( $\mu\text{m}^3/\text{sec}$ ) | $Q_i$ ( $\mu\text{m}^3/\text{sec}$ ) |
|-----------------|---------------------------|-------------------------|--------------------------------------|--------------------------------------|
| Sensitivity (%) | 25.4                      | 3                       | - 0.9                                | 0.3                                  |

In Figures 5.9, 5.10, 5.11, and 5.12, the multiple linear regression results are compared with experimental bubble data at detachment from apparatus 1A, 2A, 2B, and 2C.

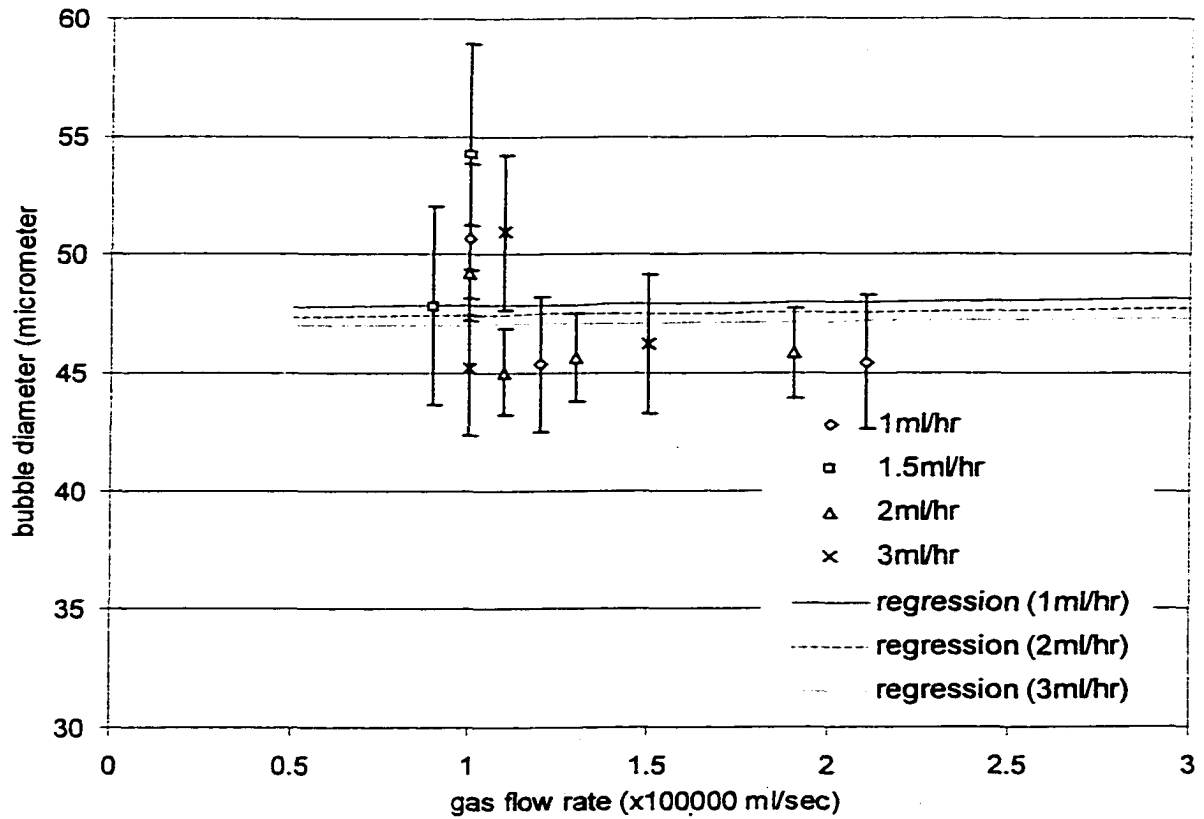


Figure 5.9 Bubble diameter generated from apparatus 1A in different gas and liquid flow rate with multiple regression results

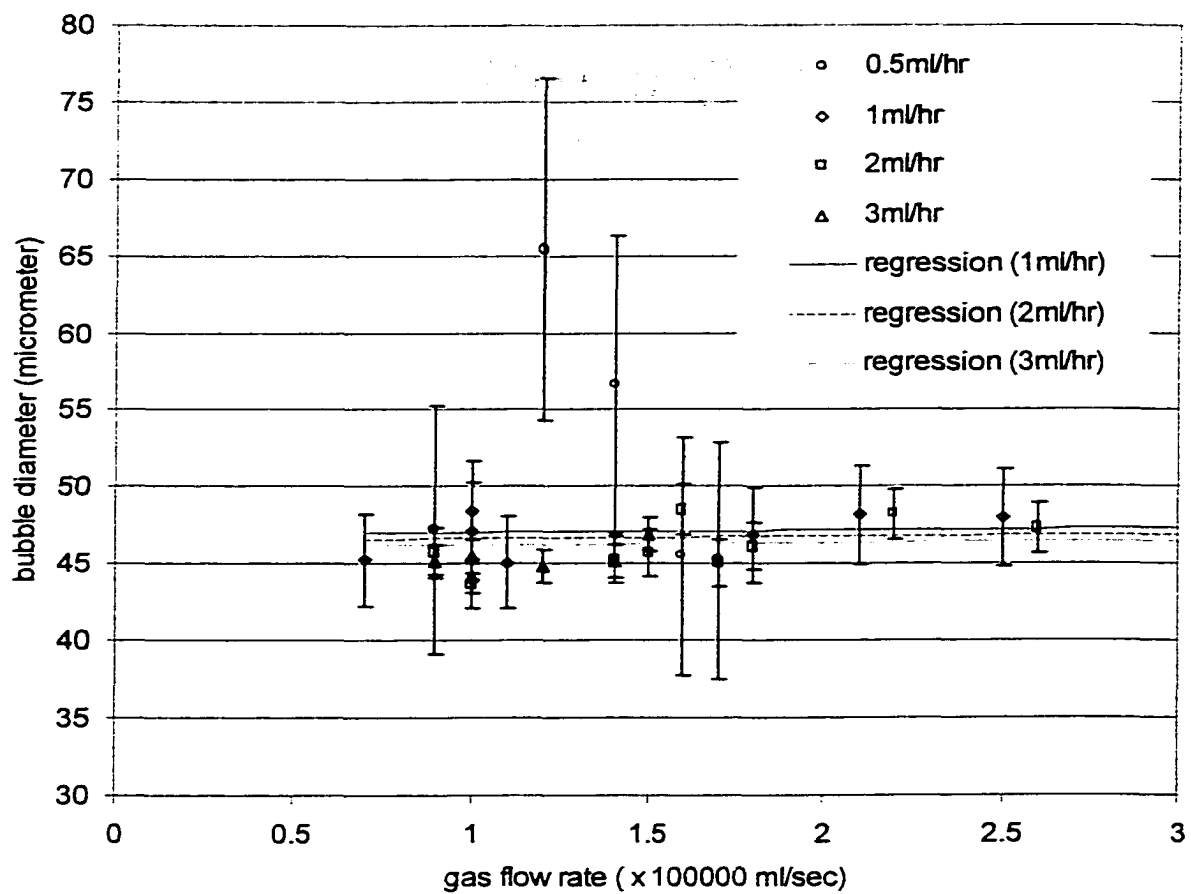


Figure 5.10 Bubble diameter generated from apparatus 2A in different gas and liquid flow rate with multiple regression results

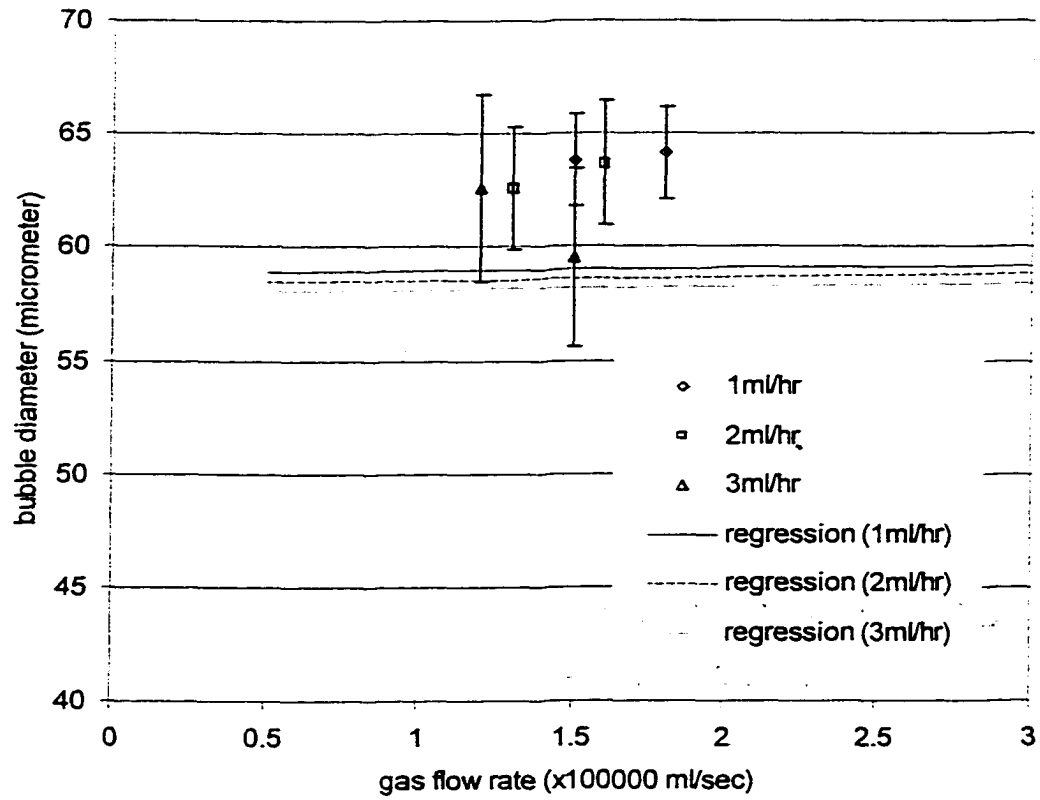


Figure 5.11 Bubble diameter generated from apparatus 2B in different gas and liquid flow rate with multiple regression results

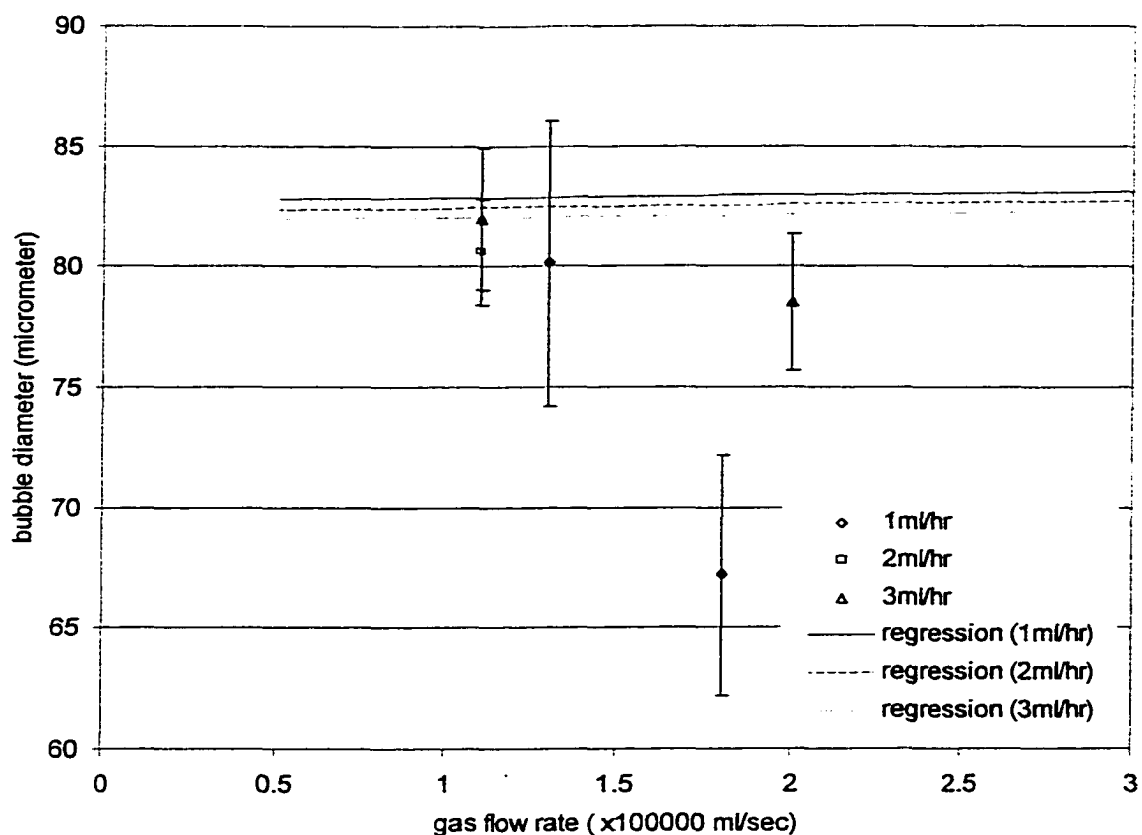


Figure 5.12 Bubble diameter generated from apparatus 2C in different gas and liquid flow rate with multiple regression results

The formed bubbles in apparatus 1A and 2A are relatively uniform in size. However, the bubbles formed in apparatus 2B and 2C are not uniform, and their standard deviation varies from 1.45  $\mu\text{m}$  to 17.11  $\mu\text{m}$  for apparatus 2B and 2.2  $\mu\text{m}$  to 5.97  $\mu\text{m}$  for apparatus 2C. It is apparent from the experimental data that the bubble diameter increases with increasing chamber volume. The regression model also reflects this behavior. Increase in bubble diameter is expected with increasing orifice diameter and gas flow rate. Their contributions to the bubble size, however, are very small. Decrease in bubble diameter is predicted with increasing liquid flow rate. Contribution of these parameters to

the bubble size variation, however, is very small compared with the effect by chamber volume.

### 5.3 Comparison of experimental data with theoretical model

Increase in gas flow through the orifice requires increased chamber pressure to drive the gas. In the quiescent liquid model, Pinczewski (1981) considered varying chamber pressure during single bubble growth. Their simulation showed the variation of chamber pressure during bubble growth was strongly dependant on the gas supply rate in the formation of final bubble size of 0.18 cm.

In the original and modified prediction models, the bubble is set to start forming when its diameter is the same as orifice diameter. This condition requires a same pressure in the chamber regardless of the gas flow rate into the chamber according to the equation (3.35). However, the gas liquid interface is in a dynamic situation, and the dynamic initial condition needs to be applied. In simulation, applying initial conditions that can reflect the increased chamber pressure caused by increased gas flow at the start of simulation through the orifice is needed. This condition is discussed below, requires additional chamber pressure added to the initial condition. This pressure is calculated from equation (3.28). Because the actual gas velocity through the orifice is not known, superficial velocity is estimated for the calculation by dividing gas flow rate into the chamber by orifice cross-sectional area. The estimated additional pressures to the initial pressures in chamber 1A, 2A, 2B, and 2C are in Table 5.6.

Table 5.6 Additional chamber pressures required with different gas flow rates

| Gas flow rate into chamber<br>( X 100000 cm <sup>3</sup> /sec) | Superficial gas velocity<br>(cm/sec) | Additional pressure<br>(dyne/cm <sup>2</sup> ) |
|--|--------------------------------------|--|
| 1  | 62.5                                 | 24218.75                                       |
| 2  | 125                                  | 48437.5  |
| 3  | 187.5                                | 72656.25                                       |

Figure 5.13 shows a simulation of determining bubble diameter. The duration of time until the bubble detaches from the orifice is determined when the force balance equation (3.34) for bubble detachment is satisfied. This Figure shows the bubble growth at the orifice of 4.2  $\mu m$  in diameter with  $2.5 \times 10^{-7} cm^3$  of chamber volume, 0.5 ml/hr liquid flow and  $1 \times 10^{-5} ml / sec$  gas flow rate. The bubble is assumed to be detached when the detaching drag force is equal to the attaching force, and this point is illustrated with a dotted line.



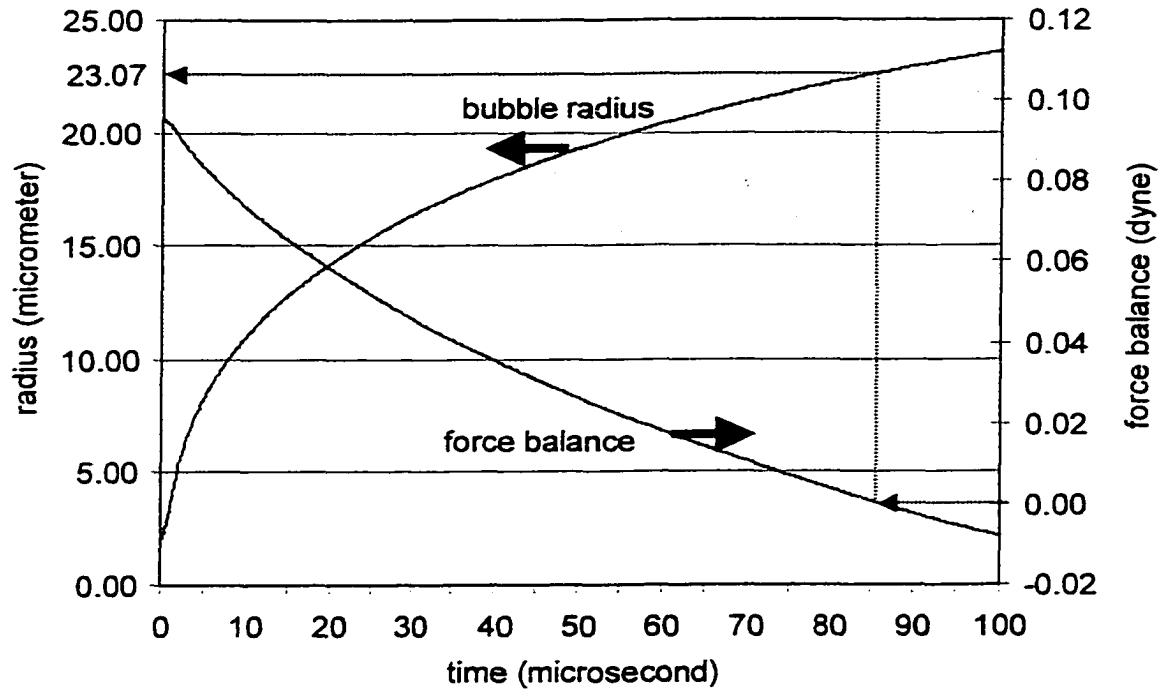


Figure 5.13 Bubble growth and force balance at the orifice of  $4.2 \mu m$  diameter with  $2.5 \times 10^{-7} cm^3$  of chamber volume, 0.5 ml/hr liquid flow and  $1 \times 10^{-5} ml / sec$  gas flow

The bubble is considered as detached when the force balance is equal to zero.

This calculation enables the bubble size and growing time prediction at the corresponding condition. For the case of above example, the bubble detaches at 86.3 microseconds with diameter of  $46.14 \mu m$ . Assuming that the period of time required for a bubble diameter equals to the orifice diameter yields a rough approximation of bubbling frequency of 5000 Hertz.

### 5.3.1 Original prediction model for experimental bubble production

The prediction model uses the equations in section 3.8. The model predictions for the bubble production in apparatus 1A, 2A, 2B, and 2C in various gas, and liquid flow rates are compared with the experimental data and shown in Figures 5.14, 5.15, 5.16, and 5.17, respectively.

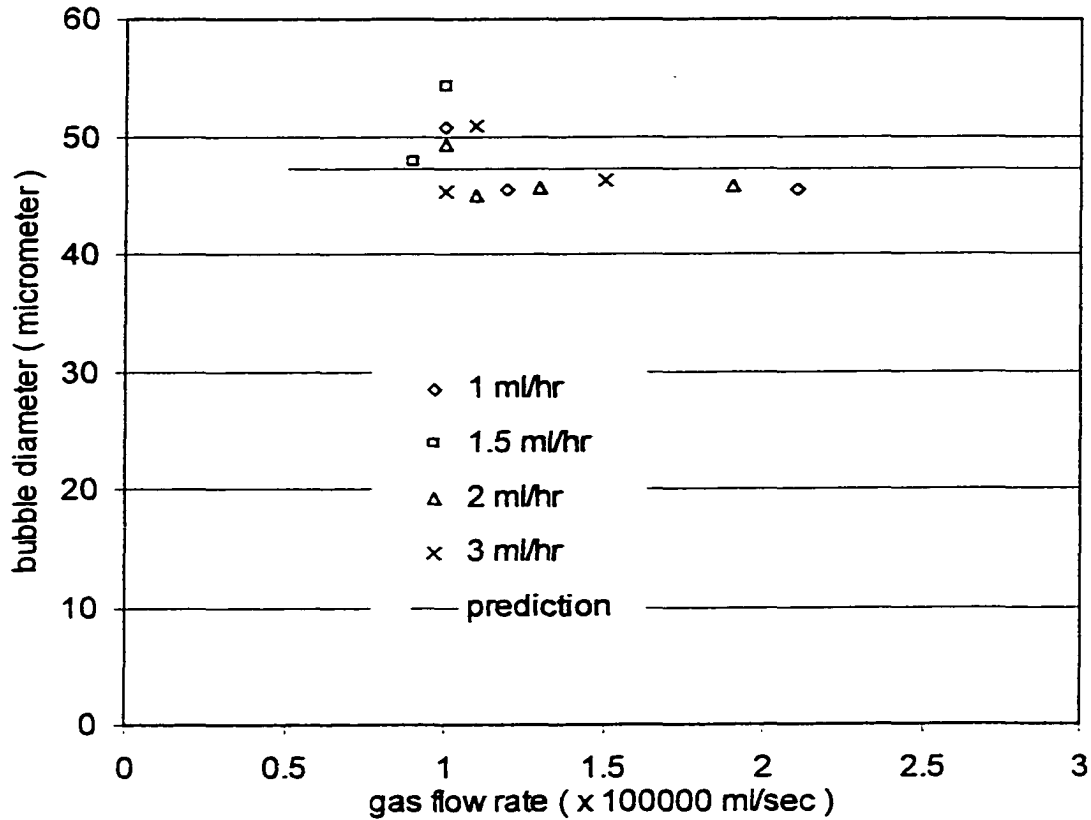


Figure 5.14 Comparison between the experimental data in Table 5.1 and the original prediction model

The predicted bubble diameter at detachment with the orifice of  $6.6 \mu\text{m}$  in diameter and  $2.5 \times 10^{-7} \text{cm}^3$  of chamber volume is  $47.23 \mu\text{m}$ .

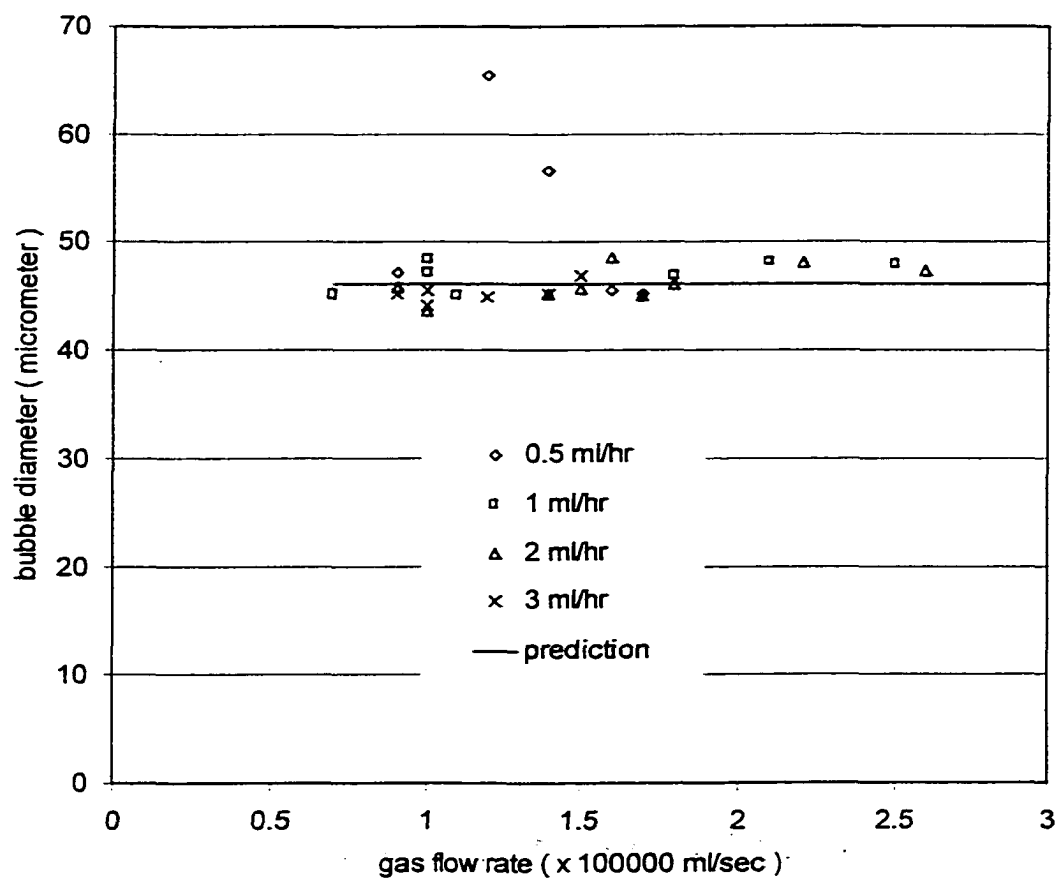


Figure 5.15 Comparison between the experimental data in Table 5.2 and the original prediction model

The predicted bubble diameter at departure with the orifice of  $4.2 \mu\text{m}$  in diameter and  $2.5 \times 10^{-7} \text{cm}^3$  of chamber volume is  $46.14 \mu\text{m}$ .

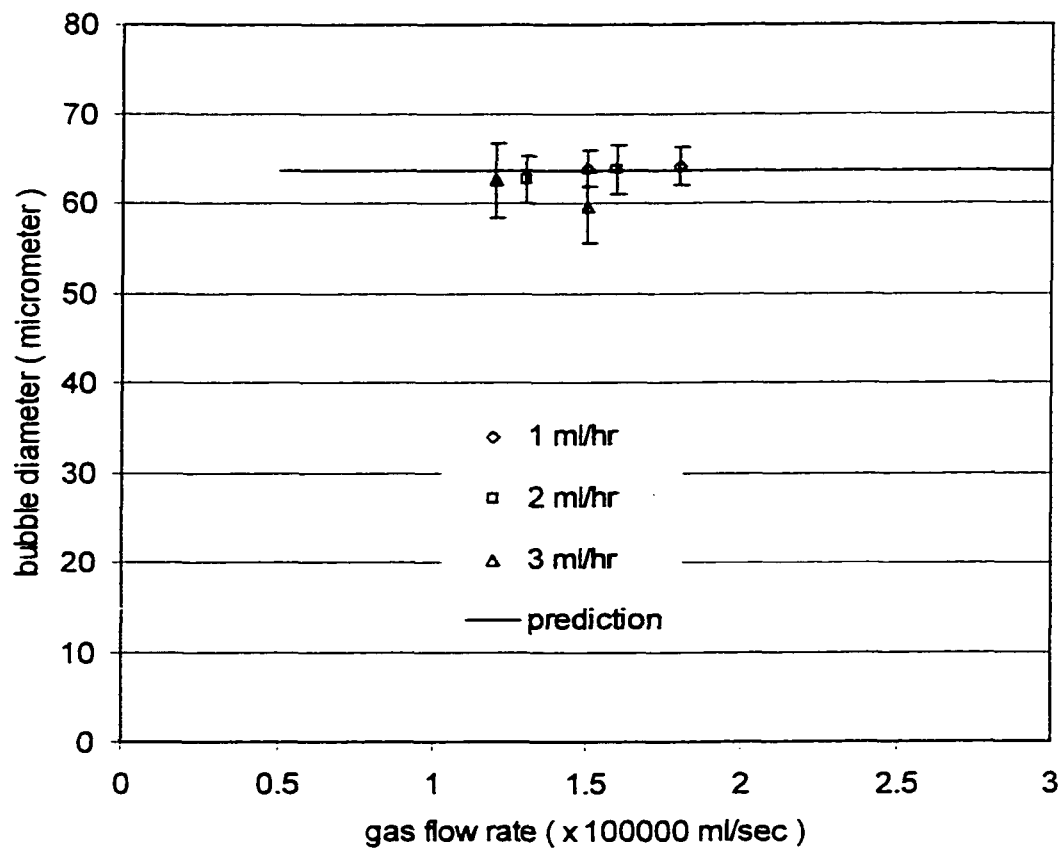


Figure 5.16 Comparison between the experimental data in Table 5.3 and the original prediction model

The predicted bubble diameter at departure with the orifice of  $4.0 \mu\text{m}$  in diameter and  $5 \times 10^{-7} \text{cm}^3$  of chamber volume is  $63.67 \mu\text{m}$ .

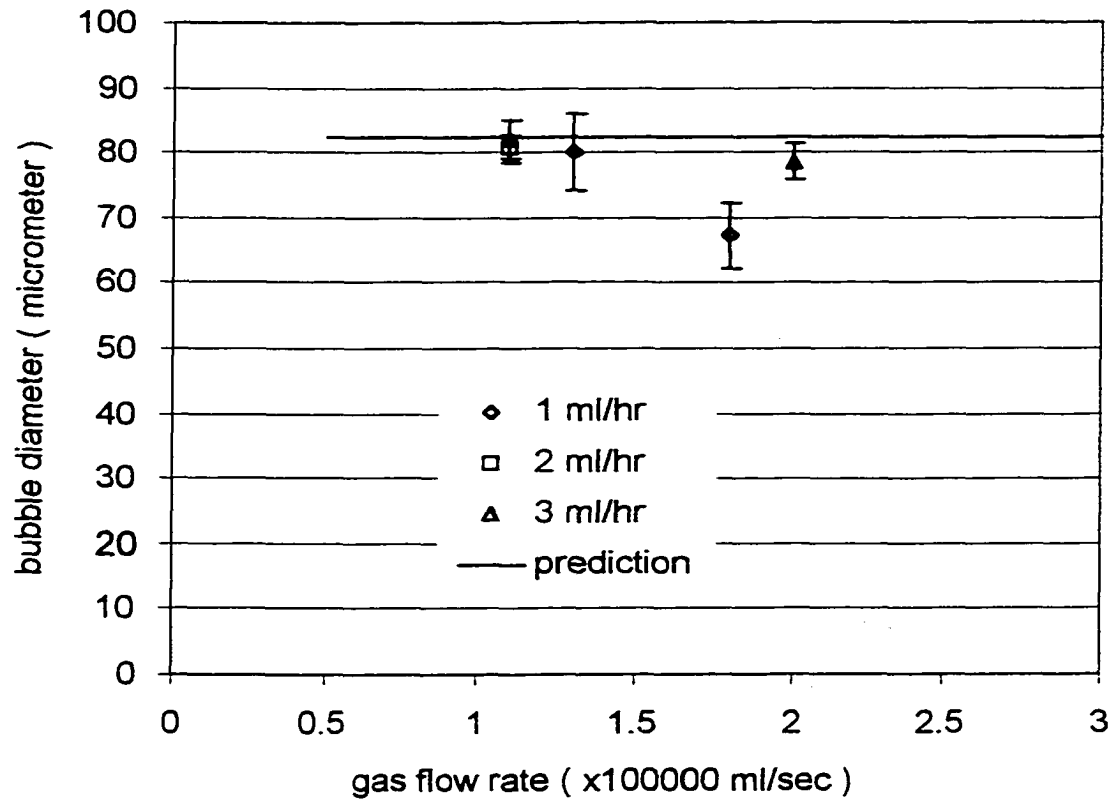


Figure 5.17 Comparison between the experimental data in Table 5.4 and the original prediction model

The predicted bubble diameter at departure with the orifice of  $2.0 \mu m$  in radius and  $10 \times 10^{-7} cm^3$  of chamber volume. Model prediction of bubble diameter =  $82.2 \mu m$

During the simulation, the drag coefficient defined in equation (3.33), which is the analytical form for bubbles or drops rising or freely falling through a continuous phase, is determined empirically because no information is available in the literature on values of the drag coefficient for bubbles in a microchannel. The drag coefficient is also very sensitive to the liquid flow rate, roughness, and shape of the channel. It is replaced

to apply to the condition of restricted liquid flow in the channel used in current study as follows:

$$C_D = \frac{C}{Re^2} \quad (5.1)$$

where  $C$  is constant number in a given system. For each set of experiment of 1A, 2A, 2B, and 2C,  $C$  is set to 3030, 2020, 1010, and 606. The Simulink program for this simulation is shown in appendix C. In this simulation model, effective cross-sectional area of bubble is assumed to be that of a spherical bubble. This model shows no influence of liquid velocity in the channel to the final bubble size.

### 5.3.2 Modified prediction model

The modified prediction model uses the equations in section 3.8, except the modified drag coefficient described in section 3.9 is used instead of determining it empirically. The model predictions for the bubble production in apparatus 1A, 2A, 2B, and 2C in various gas and liquid flow rates are compared with the experimental data and shown in Figure 5.18, 5.19, 5.20, and 5.21 respectively.

In this modified model, the effective diameter of the bubble is set to 85 % of the spherical bubble diameter empirically to simulate the results from experiments with apparatus 1A and 2A. To simulate experiments with 2B and 2C, effective diameters are set as 63 % and 48 % of spherical bubble diameter respectively. The Simulink program for this simulation is in appendix D.

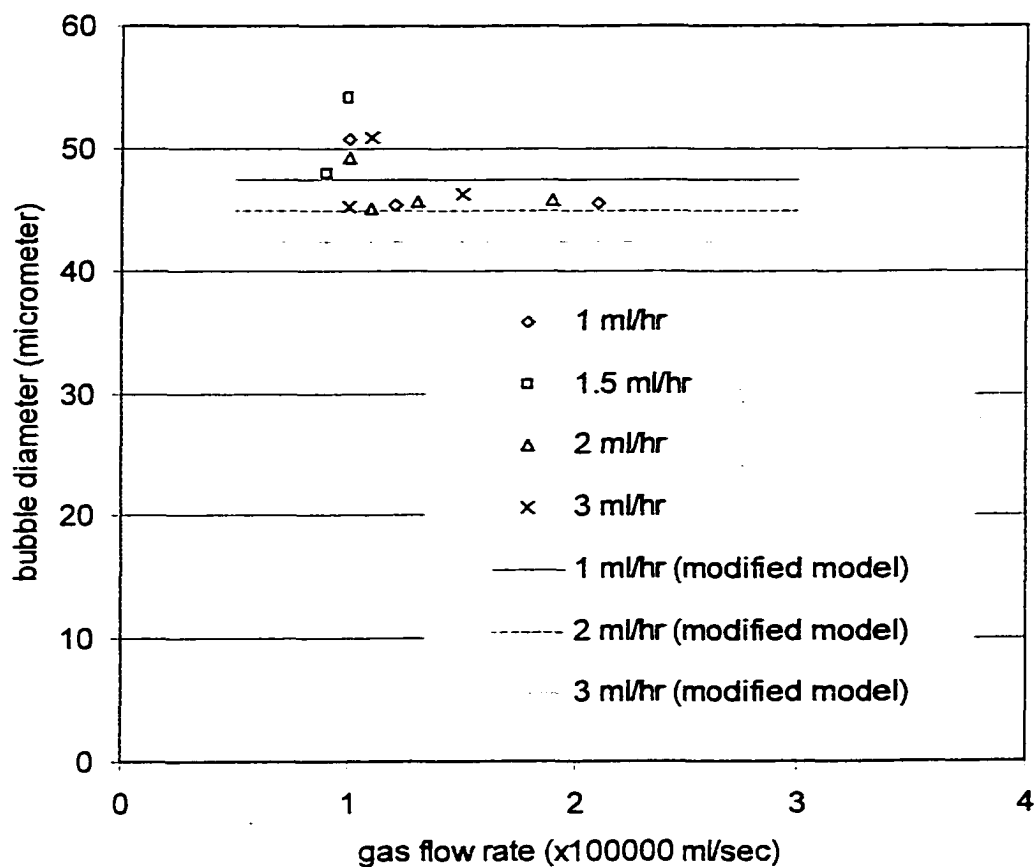


Figure 5.18 Comparison between the experimental data in Table 5.1 and the modified prediction model

The bubble diameters at departure with the orifice of  $6.6 \mu m$  in diameter and  $2.5 \times 10^{-7} cm^3$  of chamber volume are predicted  $47.14 \mu m$ ,  $44.9 \mu m$ , and  $42.32 \mu m$  for liquid flow rate of 1, 2, and 3 ml/hr, respectively

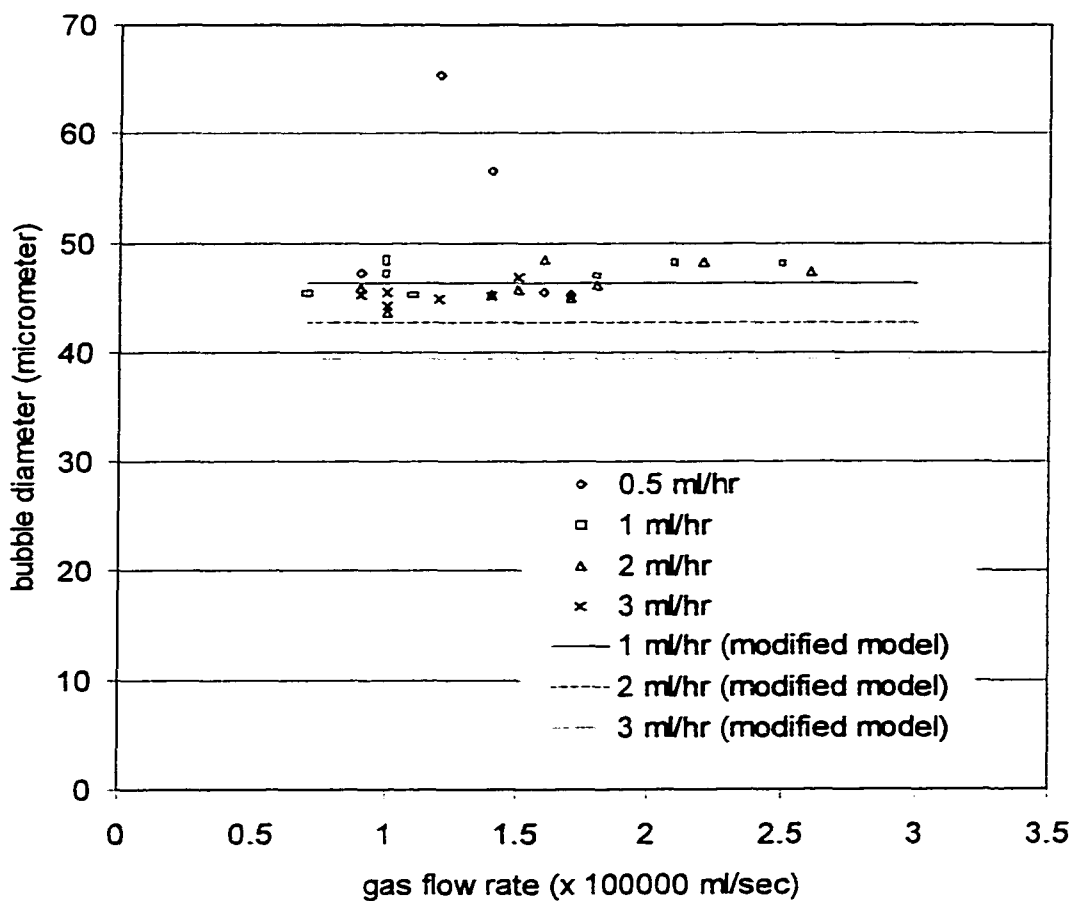


Figure 5.19 Comparison between the experimental data in Table 5.2 and the modified prediction model

The predicted bubble diameters at departure with the orifice of  $4.2 \mu m$  in diameter and  $2.5 \times 10^{-7} \text{cm}^3$  of chamber volume are  $46.32 \mu m$ ,  $42.76 \mu m$ , and  $39.3 \mu m$  for liquid flow rate of 1, 2, and 3 ml/hr, respectively.

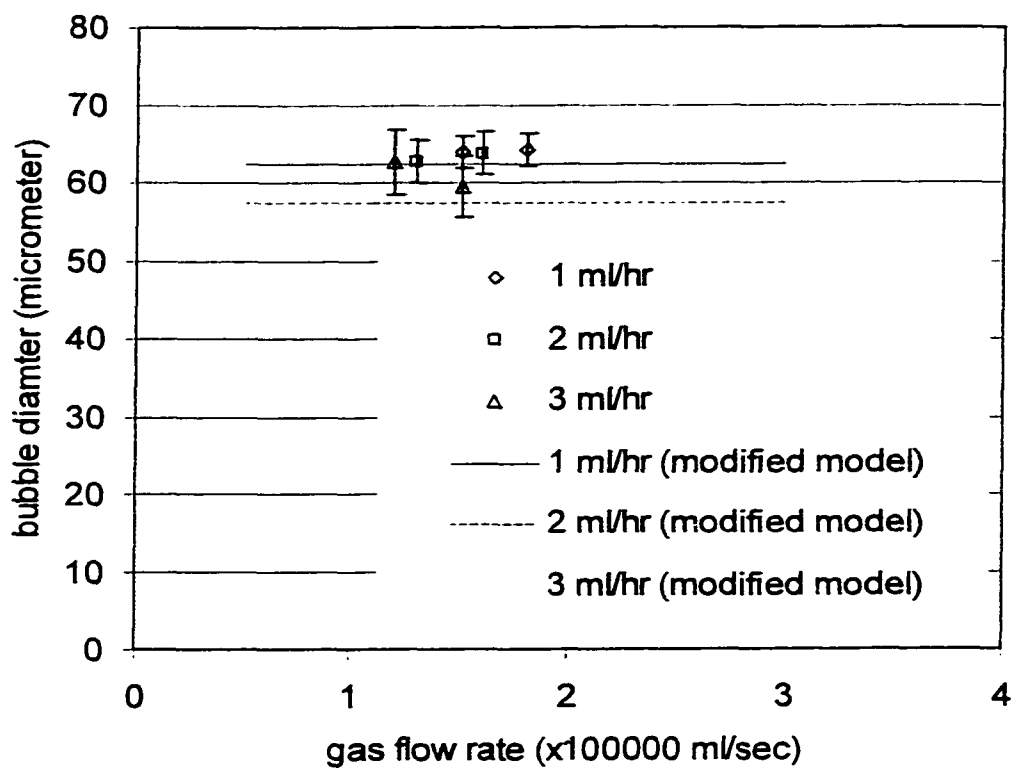


Figure 5.20 Comparison between the experimental data in Table 5.3 and the modified prediction model

The predicted bubble diameters at departure with the orifice of  $2.0 \mu m$  in radius and  $5 \times 10^{-7} cm^3$  of chamber volume are  $62.3 \mu m$ ,  $57.32 \mu m$ , and  $52.54 \mu m$  for liquid flow rate of 1, 2, and 3 ml/hr, respectively.

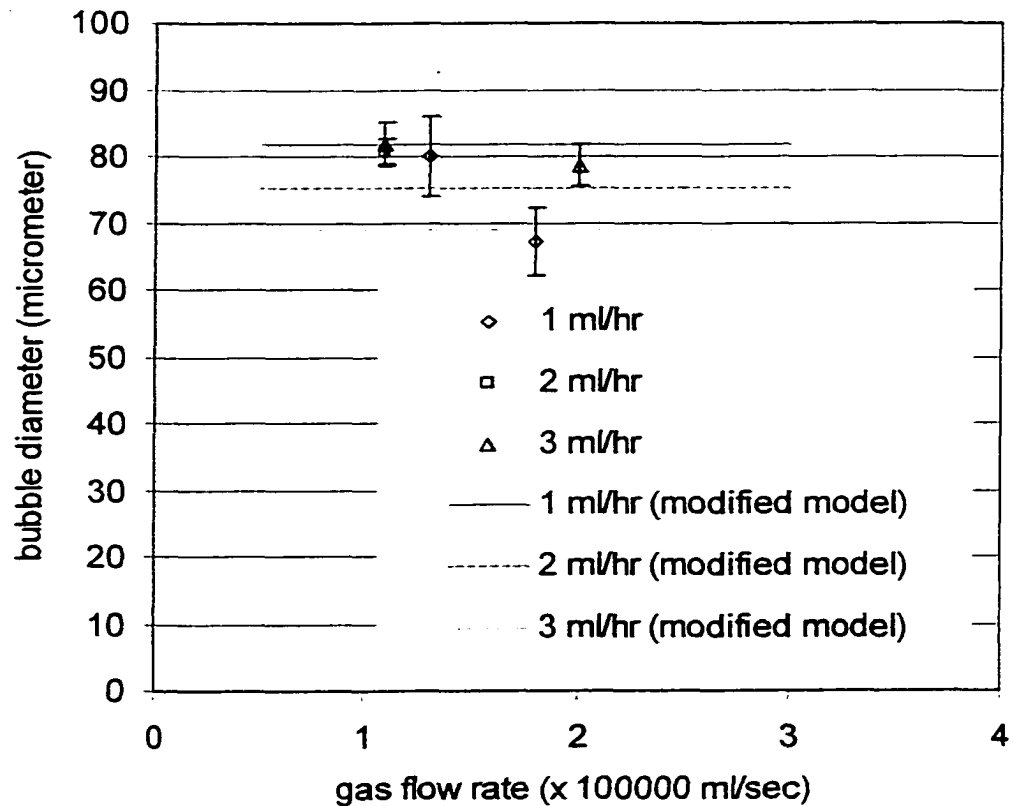


Figure 5.21 Comparison between the experimental data in Table 5.4 and the modified prediction model

The predicted bubble diameters at departure with the orifice of  $2.0 \mu\text{m}$  in radius and  $10 \times 10^{-7} \text{cm}^3$  of chamber volume are  $81.78 \mu\text{m}$ ,  $75.24 \mu\text{m}$ , and  $68.96 \mu\text{m}$  for liquid flow rate of 1, 2, and 3 ml/hr, respectively.

### 5.3.3 Gas momentum change

The simulation model and modified model can also show the momentum change of the gas from the orifice during the bubble formation. The influence of different chamber volumes to the gas momentum is shown in Figure 5.22

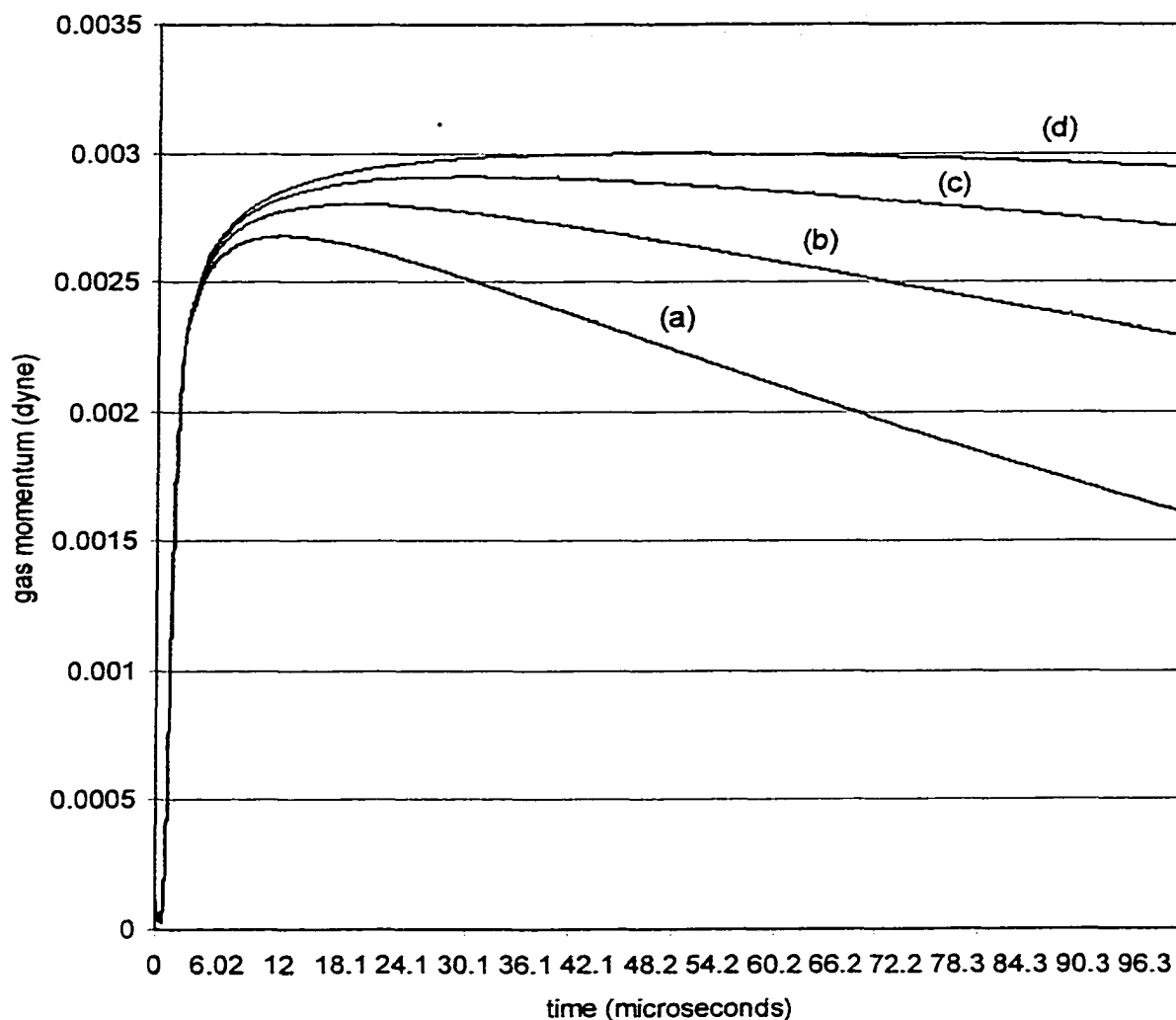


Figure 5.22 Model prediction of gas momentum change at the orifice with different chamber volumes during bubble formation

(orifice diameter =  $4.2 \mu\text{m}$ , chamber volume (a) =  $2.5 \times 10^{-7} \text{ cm}^3$ , (b) =  $5 \times 10^{-7} \text{ cm}^3$ , (c) =  $10 \times 10^{-7} \text{ cm}^3$ , and (d) =  $20 \times 10^{-7} \text{ cm}^3$ , gas flow rate into the chamber =  $1 \times 10^{-5} \text{ ml / sec}$ )

Figure 5.22 shows that the magnitude of gas momentum gets larger as the chamber volume is increased. The momentum change at the orifice in the small chamber volume during bubbling process shows fast decay from the maximum value while the momentum at the orifice in bigger chamber decreases slowly.

Both original and modified simulation models show contribution of the gas momentum relative to the liquid flow rate in the channel. Gas momentum at the orifice is affected by the liquid flow rate that passes across the orifice and the gas flow rate into the chamber. The changes in gas momentum by liquid cross flow and by gas flow rate are shown in Figure 5.23 and Figure 5.24, respectively.

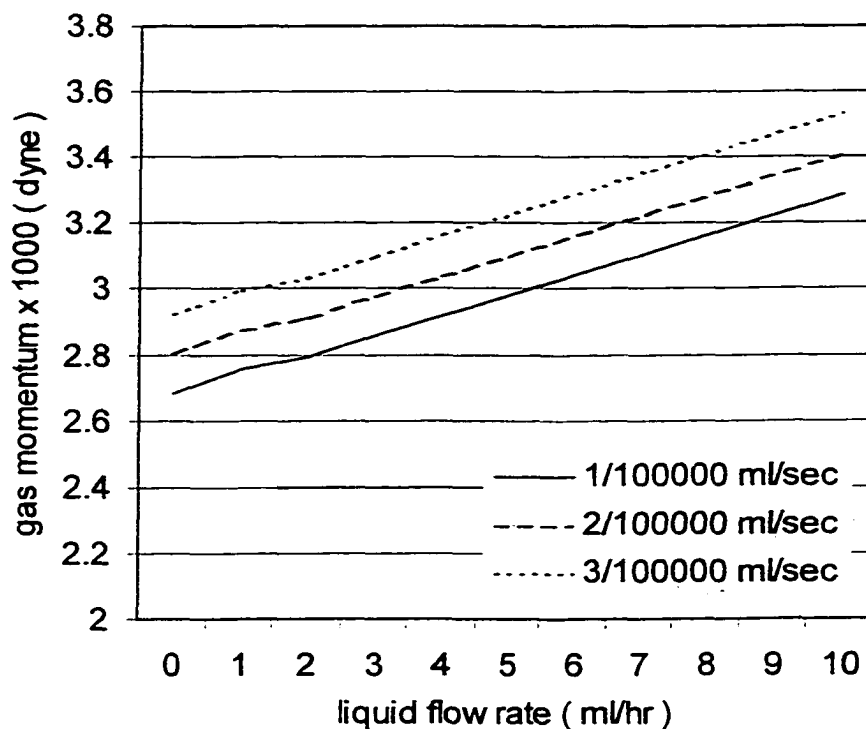


Figure 5.23 Changes in gas momentum at the orifice with different liquid flow rate across the orifice of  $4.2 \mu\text{m}$  in diameter with the chamber volume of  $2.5 \times 10^{-7} \text{ cm}^3$  at three different gas flow rates

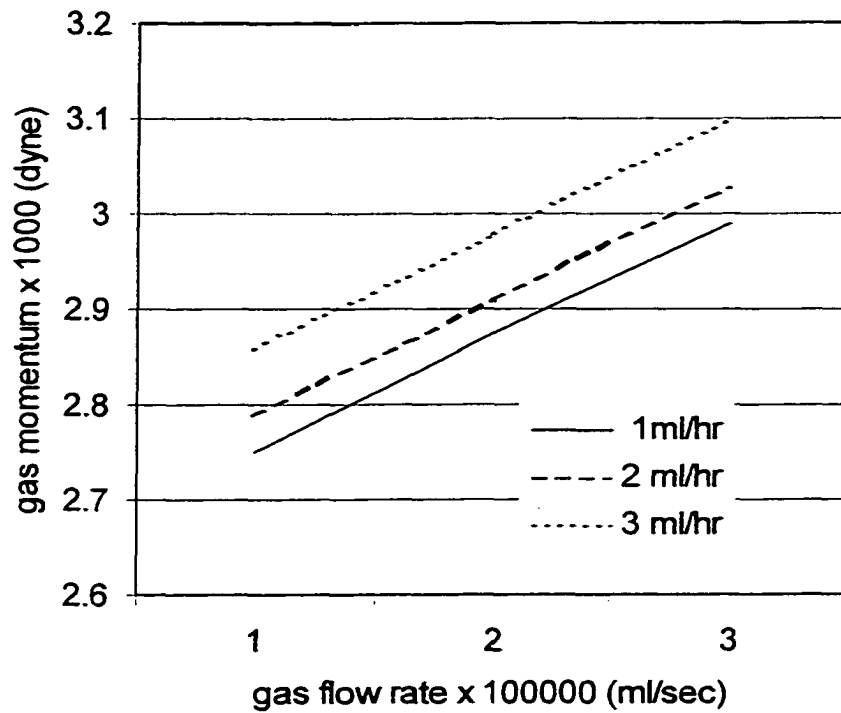


Figure 5.24 Changes in gas momentum at the orifice of  $4.2 \mu\text{m}$  in diameter with different gas flow rate into the chamber volume of  $2.5 \times 10^{-7} \text{ cm}^3$  at three different liquid flow rates across the orifice

Figure 5.23 shows increase in gas momentum as the liquid flow rate increases. Gas momentum is also increased when the gas flow rate into the chamber increases as shown in Figure 5.24. The gas momentum changes during bubble formation suggest the increase in gas momentum as the chamber volume or flow rate in the liquid channel increases.



## CHAPTER 6

### DISCUSSION

The hypothesis (section 1.3) is directed at producing oxygen microbubbles within a *microchannel of liquid cross flow in continuous manner to estimate the potential usage as a blood oxygenator*. To have this bubble made, it is hypothesized that the size of bubble is affected by orifice size, chamber volume beneath the orifice and velocity of crosscurrent liquid flow across the orifice. In this chapter, the influences of factors in the hypothesis are discussed by comparing experimental data and simulation results. This section is organized according to the specific aims in section 1.3.

#### 6.1 Design

The single bubble formation from a submerged orifice has suggested that the bubble formation is strongly influenced by the conditions of the gas supply to the bubble. In the single bubble formation regime, the chamber volume plays an important role in determining bubble size. Smaller orifice diameter is known to produce smaller bubble. The bubble formation under constant and intermediate conditions suggest that the chamber volume should be reduced to produce smaller bubble. The bubble formation in flowing liquid, particularly cocurrent or crosscurrent flow of liquid has proved to reduce the bubble size.

To achieve the main objective of this study, producing microbubbles, orifices and chamber volumes were designed in micrometer range with crosscurrent liquid flow over the bubble forming orifice. Micromanufacturing process with silicon wafer fitted perfect to the objective of this study. The device was made as in schematic in Figure 4.1 and the picture shown in Figure 4.4.

## 6.2 Measurements

Measuring the produced bubbles required microscope with image “grabbing” instruments. Still images of bubbles were captured with 200 times magnification. The calibration error from the measurement is about one micrometer. The images are in Figure 5.1 to Figure 5.6. For capturing the bubble images, the use of strobe light was essential along with very short shutter speed of image capturing device.

## 6.3 Model

The prediction model uses equations (3.5), (3.7 b), (3.14), and (3.27) to predict bubble growth at the orifice. The detachment of bubble is predicted by plug the force equations (3.29), (3.30), (3.31), (3.32) into force balance equation (3.34). The results shown in Figure 5.14 to Figure 5.21 demonstrate that the prediction model and modified prediction model show realistic simulation and prediction of the microbubble generation behavior. There are good correspondence between experimental data and model within single bubble formation regime as shown in Figure 5.14 through Figure 5.21.

The modified prediction model uses many of the same equations as prediction model described above, but is modified by using equation (3.42) instead of equation

(3.33) to define the drag coefficient. In this modified equation of drag coefficient, the deformation of bubble during growth is added in addition to the effect of liquid channel dimension to the bubble detachment. From the data in Table 5.1 to Table 5.4, it is apparent that this modified model predictions are within the experimental data range. Because of wide variation of data, the exact trend of this modified model could not be verified. However, this modified model predicts the possibility of further reduction of bubble diameter by reducing crosscurrent liquid flow channel dimension.

## 6.4 Validation of model trend

### 6.4.1 Orifice diameter

Experimental results from different sizes of orifices with the same chamber volume (apparatus 1A and 2A) indicate little influence of orifice size to the final bubble size. The regression model in equation 5.1 tells that its contribution to the final bubble size is only 3 %. Simulation model shows bubble diameter of 47.23  $\mu\text{m}$  and 46.14  $\mu\text{m}$  from 6.6  $\mu\text{m}$  and 4.2  $\mu\text{m}$  diameter orifice in Figure 5.14 and 5.15 respectively. This prediction yields 6.3 % of sensitivity of orifice to the bubble size. The modified model predicts bubble diameters of 47.14  $\mu\text{m}$  and 46.32  $\mu\text{m}$  from 6.6  $\mu\text{m}$  and 4.2  $\mu\text{m}$  diameter of orifice, which yields sensitivity of 6.2 %.

### 6.4.2 Gas flow rate

The detached bubble size is insensitive to the range of gas flow applied in the current study. From the work by Park and his coworkers (Park et al., 1977), it is noticed that the bubble volume is insensitive at low gas flow rate. In this situation, the bubble

forms in single bubble formation regime where bubbles with diameter of 12 mm and 15.6 mm are independent of gas flow rate. Present experimental results show that the generated bubbles are in this regime. When the gas flow rate above this range is applied, the bubble becomes larger and touches the wall of liquid flowing channel. In this case, detachment behavior of the bubble differs from prediction and the final bubble size becomes unpredictable because the bubble occupies a considerable portion of the liquid flow channel. This phenomenon becomes apparent for the bubbles generated with bigger chamber volume. By examining the sizes and the variations, the bubbles from bigger chamber volumes are not in the single bubble formation regime and imply that they are resulted from liquid plug flow. A different regime of bubble formation may need to be applied for this case. However, these bubbles are beyond the current interest in the prospect of bubbles as a blood oxygenator and are not studied further.

#### 6.4.3 Chamber volume

From the Figure 5.22, it is apparent that the gas momentum at the orifice increases with chamber volume. When the instantaneous rate of gas momentum out of the orifice is high enough, the formation of bubbles become unsteady and uniform bubble can not be produced. Non-uniform bubble formation can be noticed in the experimental bubble formation data in Table 5.2 and show increased bubble size as chamber volume is increased.

From the experimental results, when the bubbles generated from the apparatus with big chamber volume (2C) are detached from the orifice, the gas momentum at that stage ranges about 0.0029 dyne from Figure 5.22. This value is about equal to the bubble

condition from apparatus 2A with gas flow rate of 3 ml/sec and liquid flow rate of 1 ml/hr in Figure 5.24. The detachment condition in this case may not be the same as current prediction model in single bubble formation regime. The bubble size may differ from the prediction, and may be the case for the experiments 2A-11 with large variation in bubble size and all the other bubbles above this size generated from higher rate of gas flow. Therefore, the momentum force has significant effect on uniform bubble formation. In addition, this value is directly related with bubbling frequency and further investigation is needed.

#### 6.4.4 Velocity of cross-flowing liquid

It is reported that the increase in liquid velocity in shear flow decreases the detached bubble size (Tsuge H., Hibino S. and Nojima U., 1981). This result is attributed to an increased drag coefficient by increased liquid velocity across the forming bubble. However, the cross flow velocity was 12.8 cm/sec in 70 mm diameter channel. The change in bubble diameter by increasing cross flow of liquid from 8 cm/sec to 12.8 cm/sec was 0.02 cm, from 0.66 cm to 0.64 cm. In comparison with the present study with liquid velocity of 5.6 cm/sec to 33.6 cm/sec through the confined microchannel of 42  $\mu\text{m}$  in hydraulic diameter, the pressure induced by increased liquid flow in their case is not significant, compare to 41410 dyne/cm<sup>2</sup> for current study, especially with their bubbling site which is open to the square bubble column of 90 mm in width and 360 mm of height.

If dimension of the liquid channel is small, it would be reasonable to assume that the effect of inertia of flowing liquid will have an effect on bubble formation. Lanauze and Harris (1972) considered this effect by adding inertia term due to liquid flow in their pressure balance equation. In the present study, the dimension of liquid channel is small

and comparable with bubble diameter. The effect of moving liquid to the bubble formation in this case is considered by introducing liquid velocity term in equation 3.28. The increased liquid flow rate causes a pressure increase at the bubbling site as well as in liquid channel. This increased pressure causes the gas momentum to increase as illustrated in Figure 5.17. As a result, formed bubble may not have uniformity in size anymore and size cannot be decreased.

Johnson (1982) put a disk on the top of a frit that consisted of porous material with 4 to 5.5  $\mu\text{m}$  of diameter. In their experiment, sea water was used as a cross flowing liquid, and details are described in the review section. It can be said that the pressure at the gap between the frit and a disk at the top stays constant because of the increased gap with liquid flow rate. As the flow rate increased, variation in bubble size is reduced toward the median bubble size of 49  $\mu\text{m}$  in diameter. The reduced bubble size suggests that the increased velocity of cross flow without increased system pressure can help to produce uniform bubble.

If every parameter in the present prediction model is fixed except liquid velocity, the pressure increase due to increased liquid flow is ignored. In this situation, the pressure difference between bubble and channel would be increased as the velocity of liquid cross flow increases. As a result, the pressure difference between chamber and the liquid channel decreases. This decrease in pressure decreases gas momentum and consequently can prevent elongated bubble neck or plug formation and produce uniform bubble. Decrease in maximum gas momentum with increased liquid velocity in this case is shown in Figure 6.1.

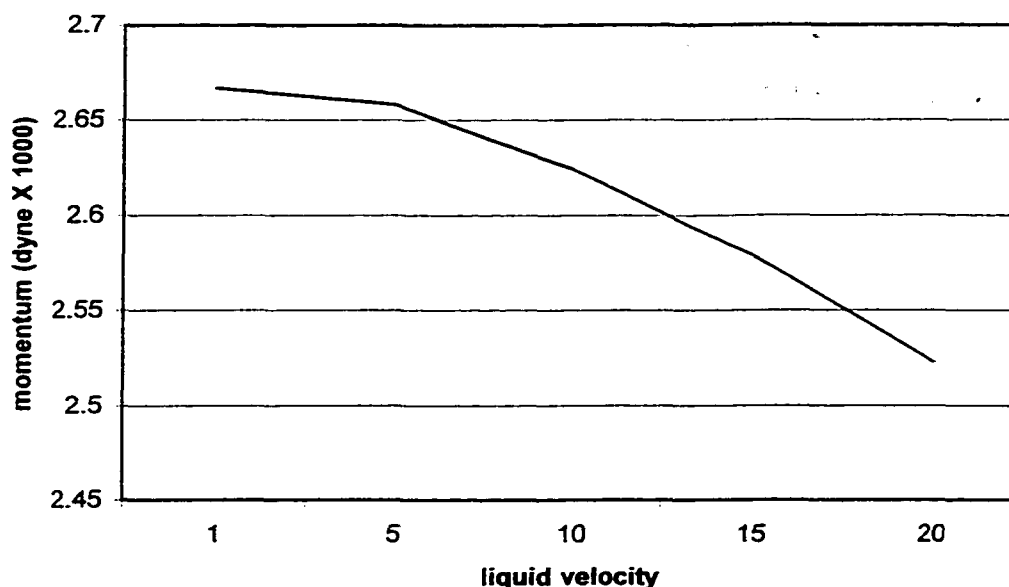


Figure 6.1 Change in maximum gas momentum with different liquid velocity (orifice of  $4.2 \mu\text{m}$  in diameter and  $2.5 \times 10^{-7} \text{ cm}^3$  of chamber volume with discharge coefficient of 0.1)

From this simulation, it can be deduced that the condition of increased liquid velocity with decreased gas momentum may provide the condition for uniform bubble generation.

#### 6.4.5 Discharge coefficient

Gas momentum change is also affected by discharge coefficient of the nozzle. In modeling the mass flow rate through orifice or nozzle, pressure drop across the orifice is measured and a discharge coefficient is multiplied to account the departure from theoretical conditions like roughness, shape, and disturbances in the path. Based on the Hagen-Poiseuille relationship, this coefficient is known as a function of the ratio among the cross-sectional area of channel, and orifice size, and a Reynolds number. In the current bubble prediction model, discharging coefficient value of 0.1 is used for all the

cases. However, during the bubble formation, the gas velocity through the orifice is not constant and the peak gas velocity would be much higher than the averaged gas flow rate through the nozzle. The discharging coefficient for this reason can be adjusted to fit experimental conditions. In the present prediction model, final bubble size is not affected by discharge coefficient. The only parameter affected is bubble growth time in such a way that increased discharge coefficient decreases bubble formation time.

## 6.5 Suggested model for further reduction in bubble size

### 6.5.1 New model

The present study on bubble formation indicates that a large chamber volume makes the final bubble size bigger. In addition, high gas flow rate or high liquid flow rate cause gas momentum increase to a certain level. If that level is high enough, it causes the bubble formation inhomogeneous. Therefore, a model with no chamber volume is suggested for smaller bubble production. Similar detachment condition described in chapter 3 is applied as follows.

$$F_{\sigma} = \sqrt{F_M^2 + F_D^2} \quad (6.1)$$

However, effective velocity is introduced that can account for the liquid velocity that increases as bubble grows from mass balance of the liquid as follows.

$$U_{eff} = \frac{U_L A_L}{A_L - A_b} \quad (6.2)$$

where  $U_{eff}$  is effective velocity of the liquid,  $U_L$  is liquid velocity in the channel,  $A_L$  is cross-sectional area of liquid channel, and  $A_b$  is cross-sectional area of forming bubble. In addition, the drag force given by Stokes's law which has following form is used.

$$F_D = 6\pi R_b \mu U_{eff} \quad (6.3)$$

In addition, it is assumed as a first approximation that the gas in the bubble is incompressible and has the following relation with the gas flow rate out of the nozzle into the bubble.

$$Q_o = V_B / t \quad (6.4)$$

This model is programmed with Simulink by Matlab and listed in appendix E.

### 6.5.2 New model predictions

The bubble size prediction and sensitivity to each parameter from the liquid channel of 42  $\mu\text{m}$  in hydraulic diameter with gas flow rate from  $1 \times 10^{-5}$  ml/sec to  $3 \times 10^{-5}$  ml/sec and liquid velocity from 1 ml/sec to 3 ml/sec is in Figure 6.2 and Table 6.1.

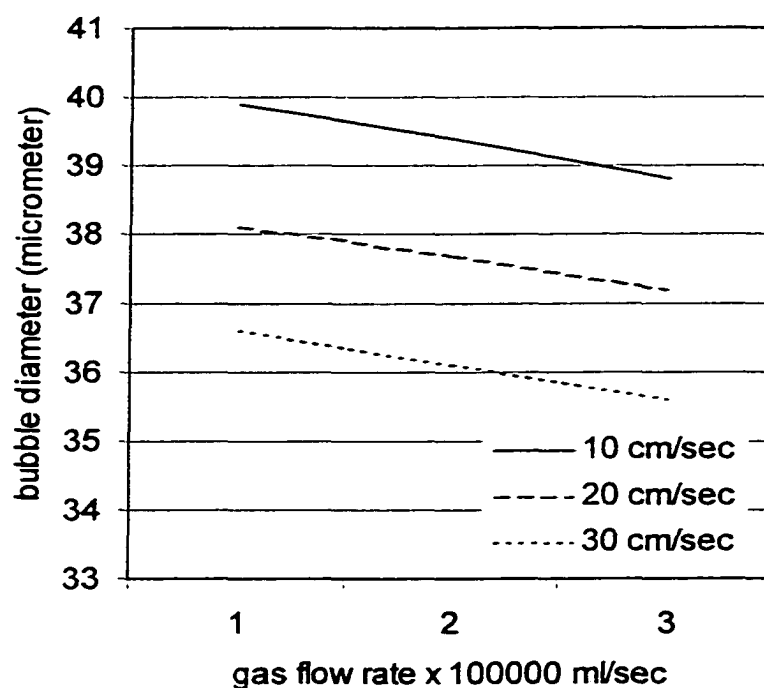


Figure 6.2 Bubble diameter change with different liquid velocities in channel from the 4.2  $\mu\text{m}$  orifice with no chamber volume underneath

Table 6.1 Sensitivity of bubble diameter to the parameters in new model

| Parameter       | Liquid velocity<br>( $U_L$ ) | Gas flow rate<br>( $Q_o$ ) | Orifice diameter<br>( $D_o$ ) | Hydraulic diameter of liquid channel ( $D_H$ ) |
|-----------------|------------------------------|----------------------------|-------------------------------|--|
| Sensitivity (%) | -4.46                        | -1.2                       | 19.5                          | 99.7   |

This model suggests further decrease in bubble diameter if the chamber volume is eliminated from design. This model also suggests that the decrease in the liquid channel dimension can reduce the final bubble size. Reduction of liquid hydraulic diameter in half results in final bubble size of 20  $\mu\text{m}$  in diameter.

### 6.5.3 A practical device

Since the main purpose of this study is generating oxygen microbubbles that can be used as a blood oxygenator, the capacity of this microbubble generator as an artificial blood oxygenator is discussed. For a 70 kg male at rest,  $1.67 \times 10^{-4}$  moles of oxygen are required per second (Guyton, 1991). If the oxygen microbubbles with the diameter of 16  $\mu\text{m}$  are used for oxygen transport media to blood, the required number of bubbles can be calculated by the equation as follows (Ashok, 1994):

$$N_{bub} = M_{req} R_{con} T \left[ \frac{4\pi}{3} (P_{atm} R^3 + 2\sigma R^2) \right]^{-1} \quad (6.5)$$

where  $R_{con}$  is gas constant, T is temperature,  $P_{atm}$  is atmospheric pressure,  $\sigma$  is plasma surface tension at body temperature, and R is bubble diameter. For this calculation, the quantities of parameters used are  $R = 8.314 \text{ J/mol K}$ ,  $T = 310 \text{ K}$ ,  $\sigma = 6.99 \times 10^{-2} \text{ N/m}$ , and  $P_{atm} = 10132500 \text{ pascal}$  (Altman 1961, Guyton 1991, Sears et al., 1988). The result of this calculation indicates that 20 million bubbles with 16  $\mu\text{m}$  in diameter are required per second to meet the basal oxygen consumption rate. Since the bubbling frequency is 5 to 10 kHz, only 2000 to 4000 orifices are needed.

## CHAPTER 7

### CONCLUSIONS AND RECOMMENDATIONS

In this thesis the physical mechanisms involved in bubble growth and detachment, and critical parameters determining bubble size in a crosscurrent flow of liquid at bubble generation site are studied. The governing parameters of bubble size as related to the potential use of oxygen bubbles as a blood oxygenator are also discussed and applied.

Three theoretical models (original prediction model, modified prediction model, and new prediction model) have been formulated for simulating the characteristics of single bubble formation from an orifice in the crosscurrent liquid flowing channel. The spherical bubble formation behavior as functions of gas flow rate, liquid velocity, orifice diameter, and chamber volume below the orifice are studied. Original prediction model simulations showed good agreement with experimental data. Gas momentum forces depend on chamber volume, liquid crosscurrent velocity, and gas flow rate into the chamber. It is concluded that the chamber volume should be reduced to zero to have smaller bubble production. A model based on this idea suggests that with zero chamber volume, the effect of orifice diameter to the bubble size becomes much more significant. The projection from the zero chamber volume model suggests that the orifice diameter and liquid channel diameter need to be reduced to about 1  $\mu\text{m}$  and 20  $\mu\text{m}$ , respectively

with gas flow rate of  $2 \times 10^{-5}$  ml / sec and liquid velocity of 30 cm / sec in order to produce oxygen bubbles of 15.6  $\mu\text{m}$ , which is smaller than the approximate diameter of capillary.

From the prediction of the zero chamber volume model, a gas flow rate of  $2 \times 10^{-5}$  ml / sec through a 1  $\mu\text{m}$  diameter nozzle into liquid crosscurrent flow in a 20  $\mu\text{m}$  diameter channel with 30 cm / sec velocity produce bubbles with 15.6  $\mu\text{m}$  in diameter with 10K Hz of frequency. Therefore, to satisfy the basal oxygen requirement, 2000 bubbling nozzles are needed.

When trenches of 20  $\mu\text{m}$  width and 1 cm length are etched on the surface of a silicon wafer with a 20  $\mu\text{m}$  of gap between them, 1000 trenches occupy 4 cm width. If 1  $\mu\text{m}$  diameter orifices are built through the wafer in each trench, a 4 cm by 1 cm piece of wafer can hold 1000 bubble generating channels. After anodic bonding with a glass plate of 1 mm thickness, the height of this piece would be 1.5 mm. Stacking two sets of these pieces would create 2000 channels from which the basal consumption rate of oxygen in the body is produced. Its dimension would be 4 cm in width, 1 cm in length, and 0.3 cm in thickness.

1000  
1000

## APPENDIX A

### PRESSURE FLUCTUATION IN THE CHAMBER

From unsteady state energy balance,

$$\frac{d}{dt}(V_c \rho_c U_c) = (\dot{m}_i - \dot{m}_o) \left( U_c + \frac{P_c}{\rho_c} \right) + \dot{Q} - \dot{W}$$

In adiabatic condition,  $\dot{Q}=0$  and  $\dot{W}=0$  because the chamber volume is fixed. Now, expand the above equation as follows.

$$U_c \frac{d}{dt}(V_c \rho_c) + V_c \rho_c \frac{dU_c}{dt} = (\dot{m}_i - \dot{m}_o) \left( U_c + \frac{P_c}{\rho_c} \right)$$

The mass balance can be expressed as

$$V_c \frac{d\rho_c}{dt} = \dot{m}_i - \dot{m}_o = (\dot{Q}_i - \dot{Q}_o) \rho_c$$

and plug this equation into the energy balance equation to yield

$$V_c \rho_c \frac{dU_c}{dt} = (\dot{Q}_i - \dot{Q}_o) P_c$$

Now apply the ideal gas relations to the above equation. First, the left hand side of the equation is expressed as

$$\begin{aligned} V_c \rho_c \frac{dU_c}{dt} &= V_c \rho_c C_v \frac{dT}{dt} \\ &= V_c \rho_c \frac{R}{M(k-1)} \frac{d}{dt} \left( \frac{P_c M}{R \rho_c} \right) \\ &= V_c \rho_c \frac{1}{(k-1)} \frac{d}{dt} \left( \frac{P_c}{\rho_c} \right) \\ &= V_c \rho_c \frac{1}{k-1} \left[ \frac{1}{\rho_c} \frac{dP_c}{dt} + P_c \frac{d}{dt} \left( \frac{1}{\rho_c} \right) \right] \\ &= V_c \rho_c \frac{1}{k-1} \left[ \frac{1}{\rho_c} \frac{dP_c}{dt} - \frac{P_c}{\rho_c^2} \frac{d\rho_c}{dt} \right] \\ &= \frac{1}{k-1} \left[ V_c \frac{dP_c}{dt} - P_c (\dot{Q}_i - \dot{Q}_o) \right] \end{aligned}$$

Equate this result with the right hand side of the energy balance equation to have

$$V_c \frac{dP_c}{d\bar{a}} = kP_c(Q_i - Q_o)$$

## APPENDIX B

### EQUATION FOR BUBBLE GROWTH

Apply first law of thermodynamics to the bubble yields

$$\frac{d}{dt}(V_b \rho_b U_b) = \dot{m}_o \left( U_b + \frac{P_b}{\rho_b} \right) + Q - W$$

Assume the bubble behaves adiabatically. Then the rate of external work by expansion is given by

$$W = P_b \frac{dV_b}{dt}$$

From the ideal gas relations

$$\begin{aligned} \frac{dU_b}{dt} &= C_v \frac{dT}{dt} \\ &= \frac{1}{k-1} \frac{R}{M} \frac{dT}{dt} \\ &= \frac{1}{k-1} \frac{R}{M} \frac{d}{dt} \left( \frac{P_b M}{R \rho_b} \right) \\ &= \frac{1}{k-1} \left( \frac{1}{\rho_b} \frac{dP_b}{dt} - \frac{P_b}{\rho_b^2} \frac{d\rho_b}{dt} \right) \end{aligned}$$

Then the following expression exists

$$V_b \rho_b \frac{dU_b}{dt} = \frac{1}{k-1} \left( V_b \frac{dP_b}{dt} - \frac{V_b P_b}{\rho_b} \frac{d\rho_b}{dt} \right)$$

Replace  $\frac{d\rho_b}{dt}$  term of above equation by using a mass balance equation expressed as

$$\frac{d}{dt}(V_b \rho_b) = V_b \frac{d\rho_b}{dt} + \rho_b \frac{dV_b}{dt} = \rho_c Q_o$$

to yield

$$V_b \rho_b \frac{dU_b}{dt} = \frac{1}{k-1} \left( V_b \frac{dP_b}{dt} - \frac{\rho_c Q_o P_b}{\rho_b} + P_b \frac{dV_b}{dt} \right)$$

Expand the first equation of thermodynamics and plug above expression yields

$$\frac{1}{k-1} \left( V_b \frac{dP_b}{dt} - \frac{\rho_c Q_o P_b}{\rho_b} + P_b \frac{dV_b}{dt} \right) = \frac{P_b \rho_c Q_o}{\rho_b} - P_b \frac{dV_b}{dt}$$

In addition

$$\frac{\rho_c}{\rho_b} = \frac{P_c T_b}{P_b T_c}$$

and assume  $\frac{T_b}{T_c} \cong 1$ , then apply to the above equation to have

$$V_b \frac{dP_b}{dt} + k P_b \frac{dV_b}{dt} = k P_c Q_o$$

## APPENDIX C

### SIMULINK PROGRAM FOR ORIGINAL MODEL

1. The original model is a nonlinear system with the following state equations:

$$\dot{x}_1 = -x_1 + x_2^2$$
$$\dot{x}_2 = -x_2 + x_1 x_2$$
$$\dot{x}_3 = -x_3 + x_1 x_2^2$$

2. The output of the system is given by:

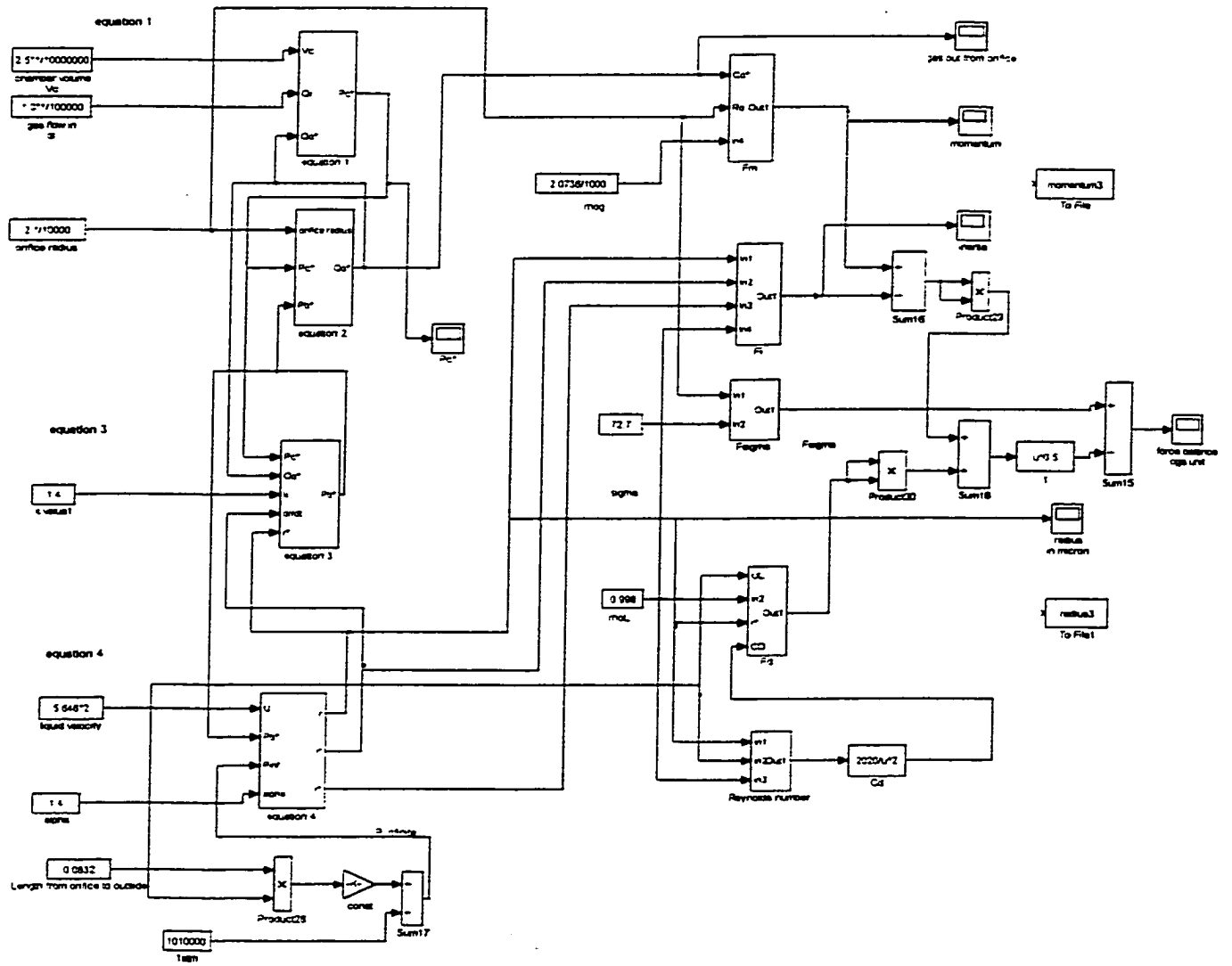
$$y = x_1 + x_2 + x_3$$

3. The initial conditions are:

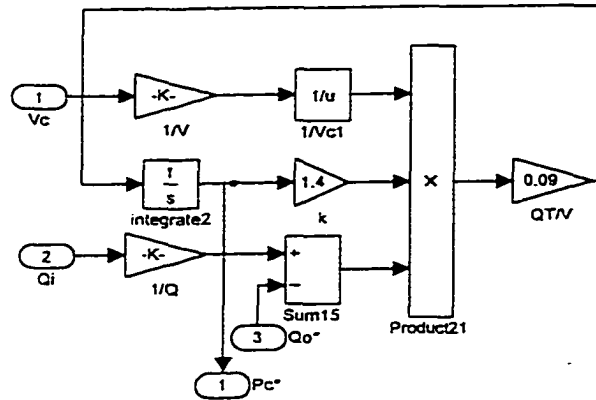
$$x_1(0) = 1, \quad x_2(0) = 0, \quad x_3(0) = 0$$

4. The system is simulated for a time interval of 10 seconds.

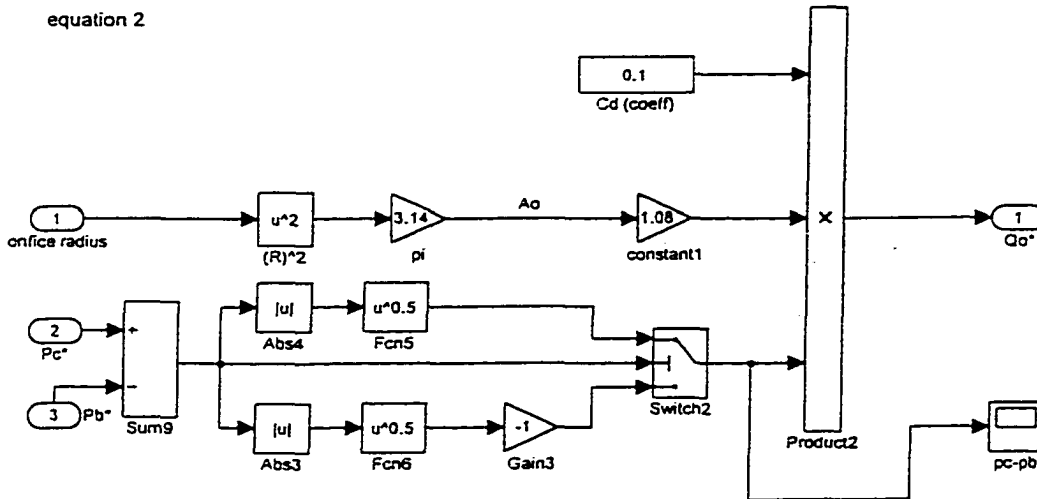
1 Simulink program for original model



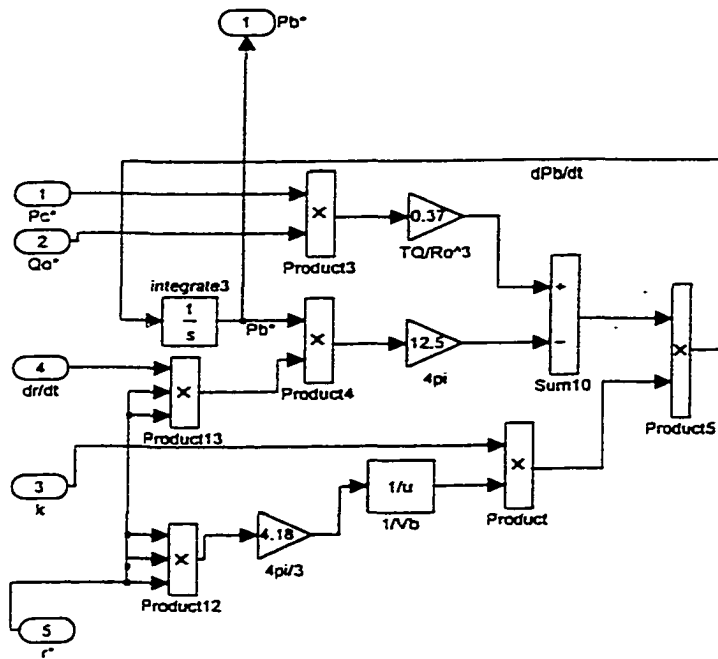
2 Simulink program for equation 1 in original model



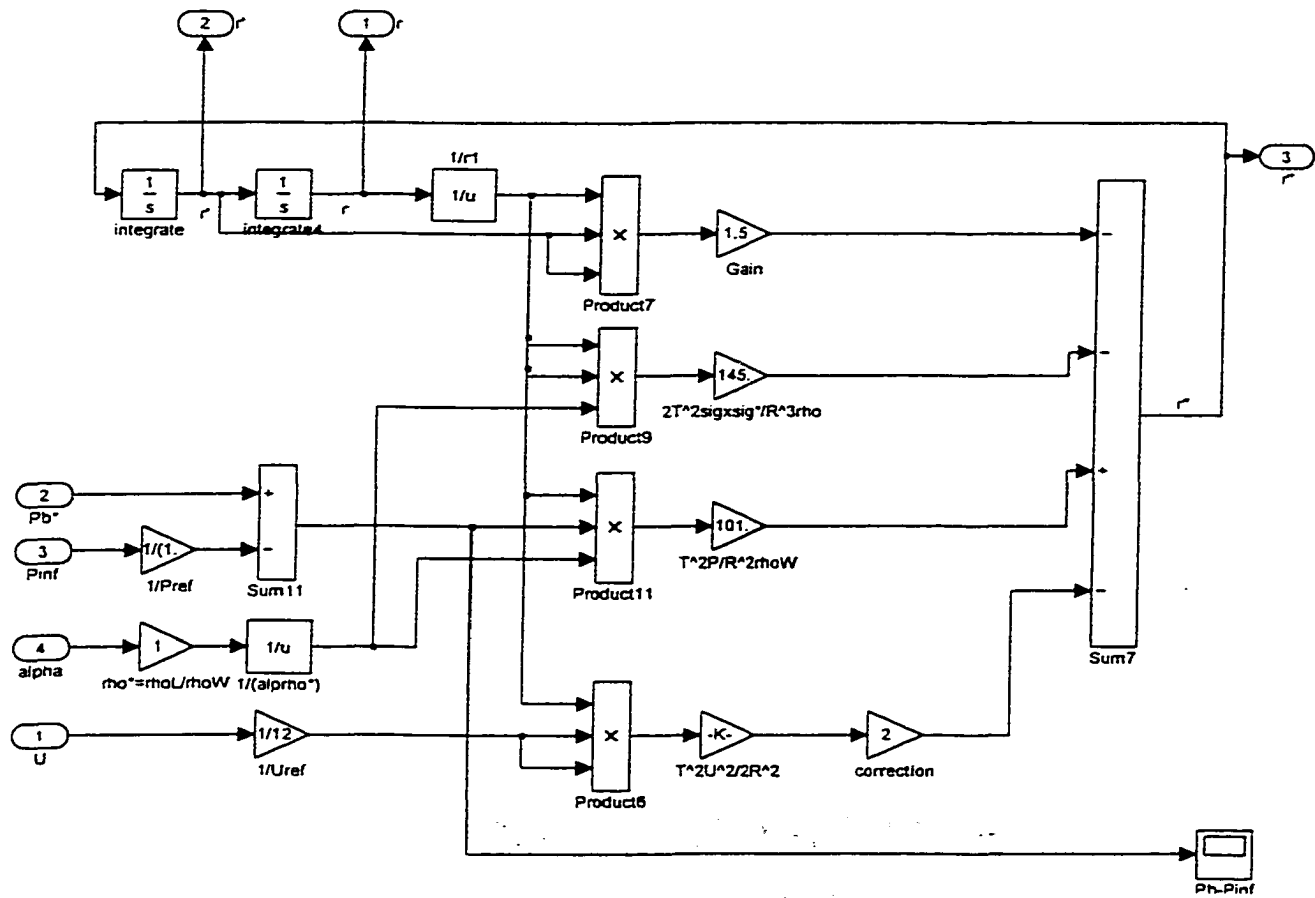
3 Simulink program for equation 2 in original model



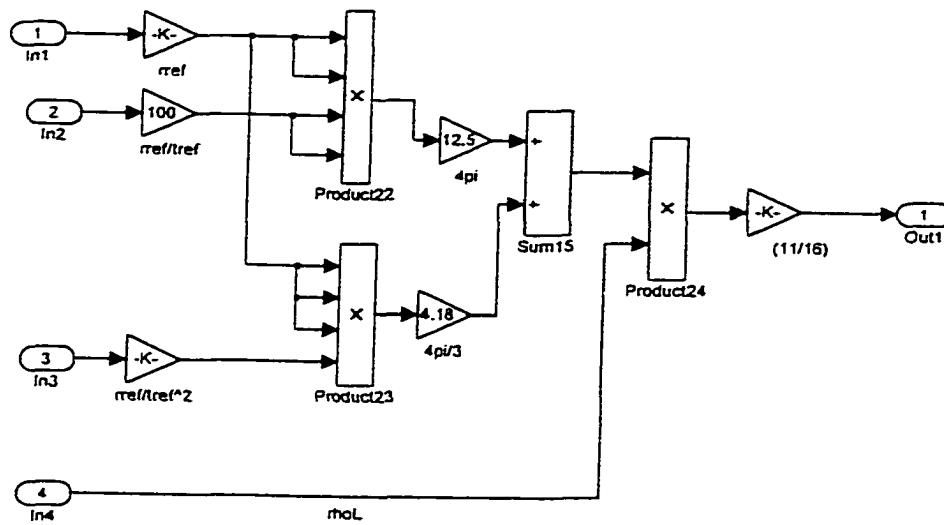
## 4 Simulink program for equation 3 in original model



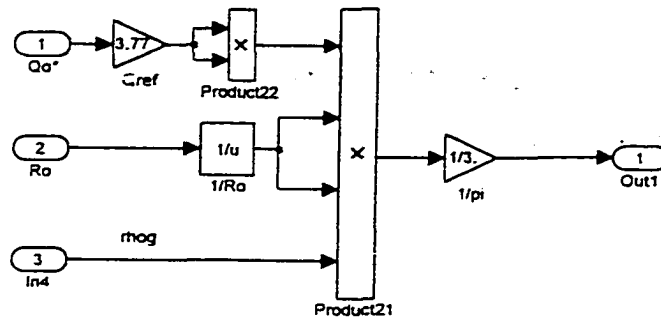
5 Simulink program for equation 4 in original model



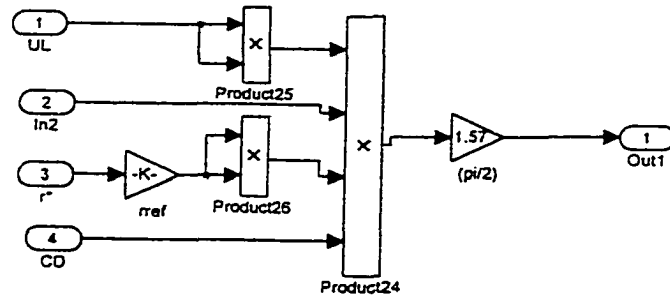
## 6 Simulink program for inertia force in original model



## 7 Simulink program for momentum force in original model



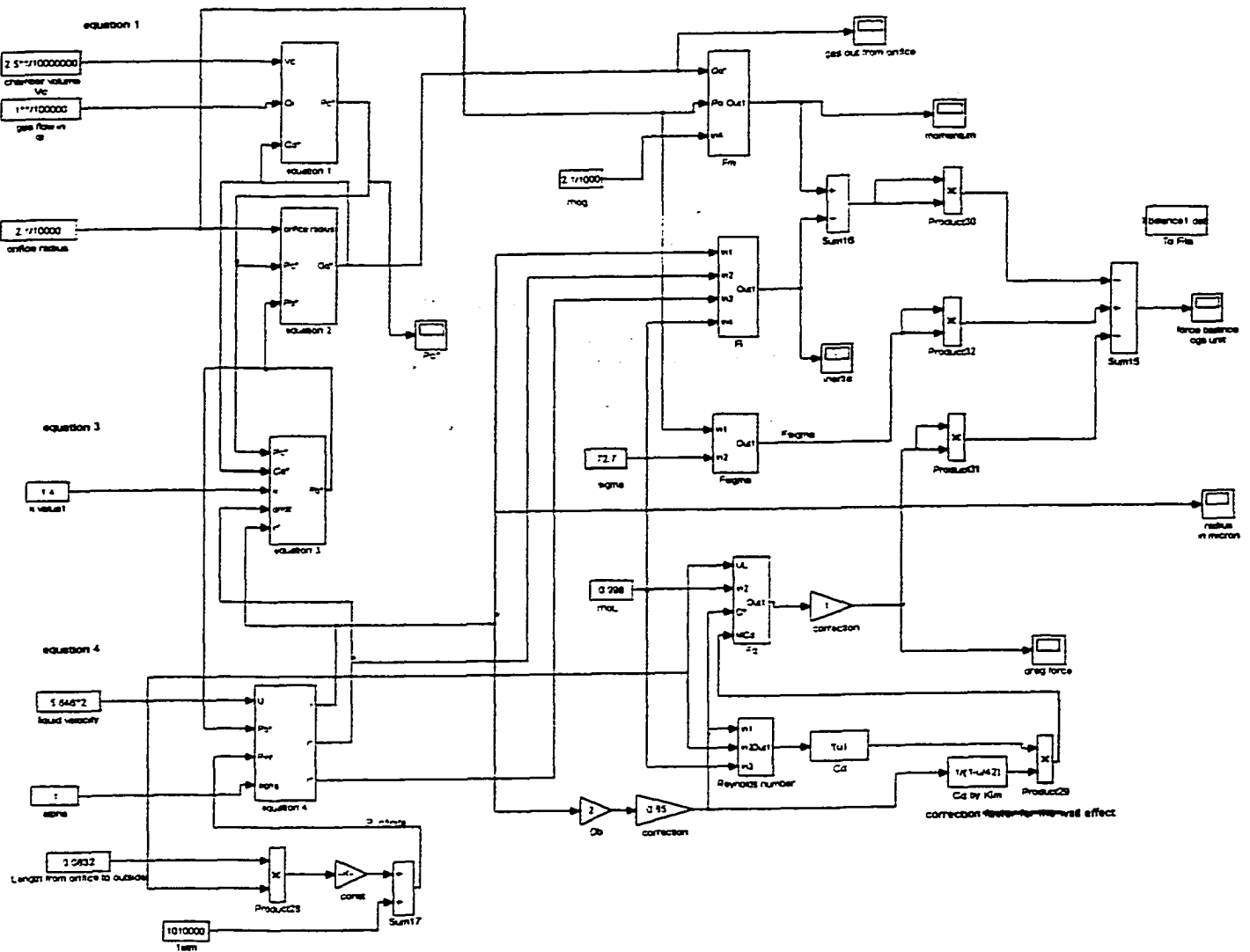
## 8 Simulink program for drag force in original model



## APPENDIX D

### SIMULINK PROGRAM FOR MODIFIED MODEL

Simulink program for the modified model shares the same program except diameter of the bubble and the drag coefficient. The effective diameter of a bubble and the modified drag coefficient are used in this modified model.



## APPENDIX E

### SIMULINK PROGRAM FOR NEW MODEL



## APPENDIX F

## NOMENCLATURE

|           |  |
|-----------|--|
| $A$       | cross sectional area of liquid channel |
| $A_c$     | cross sectional area of chamber        |
| $A_{eff}$ | effective cross sectional area         |
| $A_o$     | cross sectional area of orifice        |
| $A_p$     | projection area                        |
| $A_{ref}$ | reference cross sectional area         |
| $C$       | orifice constant                       |
| $C_{ch}$  | chamber capacitance                    |
| $C_D$     | drag coefficient                       |
| $C_{MD}$  | modified drag coefficient              |
| $d$       | diameter of initial bubble             |
| $d_N$     | nozzle diameter                        |
| $D$       | inner diameter of nozzle               |
| $D_b$     | diameter of bubble                     |
| $D_{eb}$  | effective bubble diameter              |
| $D_h$     | hydraulic diameter                     |
| $D_i$     | tube inside diameter                   |
| $D_o$     | nozzle outside diameter                |
| $E_o$     | pressure just before bubble forms      |
| $E_1$     | pressure at source                     |
| $E_2$     | pressure due to submergence            |
| $F_B$     | buoyancy force in flowing liquid phase |

|             |   |
|-------------|---|
| $F_{BO}$    | buoyancy force in quiescent phase                     |
| $F_{bm}$    | drag force due to bubble motion                       |
| $F_D$       | drag force  |
| $F_I$       | inertia force   |
| $F_M$       | momentum force  |
| $F_\sigma$  | surface tension force                                 |
| $g$         | gravitational acceleration                            |
| $K$         | orifice constant                                      |
| $k$         | polytropic constant                                   |
| $L_n$       | length of bubble neck                                 |
| $L$         | length of the channel from orifice to the channel end |
| $M$         | virtual mass of bubble                                |
| $\dot{m}_i$ | mass flow rate of gas into the channel                |
| $\dot{m}_o$ | mass flow rate of gas out through the nozzle          |
| $P_{ref}$   | reference pressure                                    |
| $\bar{P}$   | pressure inside bubble                                |
| $P_{atm}$   | atmospheric pressure                                  |
| $P_b$       | pressure inside the bubble                            |
| $P_c$       | pressure in the chamber                               |
| $P(R)$      | pressure at the bubble surface                        |
| $P_\infty$  | pressure in the liquid channel                        |
| $P_o$       | poiseuille number                                     |

|           |   |
|-----------|---|
| $Q$       | gas flow rate into the bubble                           |
| $Q_{ref}$ | reference gas flow rate                                 |
| $Q_i$     | gas flow rate into the chamber                          |
| $Q_o$     | gas flow rate through nozzle                            |
| $Q_L$     | constant volume flow rate of liquid                     |
| $R$       | radius of bubble  |
| $R_{con}$ | gas constant  |
| $R_D$     | resistance from orifice and bubble                      |
| $R_o$     | radius of nozzle  |
| $R_{ref}$ | reference radius  |
| $R_v$     | resistance at valve                                     |
| Re        | Raynolds number   |
| S         | distance of center of bubble from nozzle                |
| $T_{ref}$ | reference time  |
| $T_c$     | temperature in the chamber                              |
| $T_i$     | temperature of gas flows into the chamber               |
| $t$       | time  |
| $t_e$     | time of expansion                                       |
| $U_{ref}$ | reference liquid velocity                               |
| $U_b$     | internal energy per unit mass of the gas in the bubble  |
| $U_c$     | internal energy per unit mass of the gas in the chamber |
| $U_L$     | liquid mean flow velocity                               |

|           |   |
|-----------|---|
| $u$       | gas velocity through nozzle   |
| $V_{ref}$ | reference volume  |
| $V_b$     | volume of bubble  |
| $V_c$     | volume of chamber   |
| $V_E$     | volume of bubble at expansion stage                                   |
| $V_F$     | final bubble volume   |
| $v$       | velocity of center of bubble  |
| $v'$      | velocity of center of bubble plus velocity of center due to expansion |
| $v_e$     | velocity of expansion   |
| $v_r$     | radial velocity of bubble growth                                      |
| $We$      | Weber number  |
| $\mu_L$   | viscosity of water  |
| $\rho_b$  | density of gas in the bubble  |
| $\rho_c$  | density of gas in the chamber   |
| $\rho_g$  | density of gas  |
| $\rho_L$  | density of liquid   |
| $\rho_w$  | density of water  |
| $\sigma$  | surface tension of bubble   |
| $\Phi$    | velocity potential  |

## BIBLIOGRAPHY

Albaugh, Kevin B., Rasmussen, Don H., "Rate processes during anodic bonding", *Journal of the American Ceramic Society*, Vol. 75, No. 10, 2644, 1992

Altman, P.L., "Blood and other body fluids", edited by Dittmer, D.S., Washington D.C., Federation of American Societies for Experimental Biology, 1961

Ashok Krishnon, "Intravascular microbubble blood oxygenator: principles and limitations", Master of Science thesis, Louisiana Tech University, 1994

Bhunja A., Pais Salvatore C., Kamotani Yasuhiro, and Kim Iee-Hwan, "Bubble Formation in a Coflow Configuration in Normal and Reduced Gravity.", *AiChE Journal*, Vol. 44, No. 7, 1998

Bird, R. Byron, Stewart, Warren E., Lightfoot, Edwin N., *Transport Phenomena*, Wiley, New York, 1960

Blanchard, D. C., Syzdek, L. D., "Production of air bubbles of a specified size", *Chemical Engineering Science*, Vol. 32, 1112 – 1114, 1977

Butler, B. D., Katz, J., "Vascular pressures and passage of gas emboli through the pulmonary circulation", *Undersea Biomedical Research*, Vol. 15, 203 – 209, 1988

Chuang, S. C. and Goldschmidt, V. W., "Bubble Formation Due to a Submerged Capillary Tube in Quiescent and Coflowing Streams", *Journal of Basic Engineering*, 705 – 711, December, 1970

Conrad, S. A., Eggerstedt, J. M., and Romero, M. D. , "Prolonged Intracorporeal Support of Gas Exchange with an Intravenacaval Oxygenator", *Chest*, Vol. 103, 158 – 161, 1993



Davidson, J. F. and Schuler, B. O. G., "Bubble formation at an Orifice in an Inviscid Liquid", Transactions of Instrumentation of Chemical Engineers, Vol. 38, 335 – 342, 1960

Fazzalari, F. L., Bartlett, R. H., Bonnell, M. R., and Montoya, J. P., "An intrapleural lung prosthesis: rationale, design, and testing", Artificial Organs, Vol. 18, 801 – 805, 1994

Flockhart, S. M., Dhariwal, R. S., "Experimental and Numerical Investigation Into the Flow Characteristics of Channels Etched in <100> Silicon", Journal of Fluids Engineering, Vol. 120, 291 – 295, 1998

Galletti P. M. and Brecher G. M., Heart-Lung Bypass, Grune and Stratton, New York, 1962

Ghosh, Anup K. and Ulbrecht, J. J., "Bubble Formation from a Sparger in Polymer Solutions II. Moving Liquid", Chemical Engineering Science, Vol. 44, No. 4, 969 – 977, 1989

Gorman, D. F., Browning, D. M., "Cerebral vasoreactivity and arterial gas embolism" Undersea Biomedical Research, Vol. 13, 317 – 335, 1986

Guyton, Textbook of MEDICAL PHYSIOLOGY, eighth edition, Saunders, 1991

Ito, R., Hirata, Y., Inoue, K., and Kitagawa, Y., "Formation of a liquid drop at a single nozzle in a uniform stream", International Chemical Engineering, Vol. 20, No. 4, 616 – 620, 1980

Johnson, B. D., Gershey, R. M., and Cooke, R. C., "A Theoretical Model for Bubble Formation at a Frit Surface in a Shear Field", Separation Science and Technology, Vol. 8, 1027 – 1039, 1982

Kawase, Y. and Ulbrecht, J. J., "Formation of Drops and Bubbles in Flowing Liquids", Industrial Engineering in Chemical Process Design and Development, Vol. 20, 636 – 640, 1981

Khurana, A. K. and Kumar, R., "Studies in bubble formation-III", Chemical Engineering Science, Vol. 24, 1711 – 1723, 1969

Kim, Ieehwan, Kamotani, Yasuhiro, and Ostrach, Simon, "Modeling Bubble and Drop Formation in Flowing Liquids in Microgravity", AIChE Journal, Vol. 40, No. 1, 19 – 28, 1994

La Nauze, R. L. and Harris, I. J., "On a model for the formation of gas bubbles at a single submerged orifice under constant pressure conditions", Chemical Engineering Science, Vol. 27, 2102 – 2105, 1972

Madou, Marleen, Fundamentals of Microfabrication, edited by Madou Marleen, CRC Press, 145, 1997

Marmur, A. and Rubin, E., "Equilibrium shapes and quasi-static formation of bubbles at submerged orifice", Chemical Engineering Science, Vol. 28, 1455 – 1464, 1973

Marshall, S. H. and Chudacek, M. W., "A MODEL FOR BUBBLE FORMATION FROM AN ORIFICE WITH LIQUID CROSS-FLOW", Vol. 48, No. 11, 2049 – 2059, 1993

McCann, J. and Prince, R. G. H., "Bubble formation and weeping at a submerged orifice", Chemical Engineering Science, Vol. 24, 801 – 814, 1969

Park, Y., Tyler, A. L. and de Nevers, N., "THE CHAMBER ORIFICE INTERACTION IN THE FORM OF BUBBLES", Chemical Engineering Science, Vol. 32, 907 – 916, 1977

Ramakrishnan, S., Kumar, R., and Kuloor, N. R., "Studies in bubble formation-I Bubble formation under constant flow conditions", Chemical Engineering Science, Vol. 24, 731 – 747, 1969

Sada, E., Yasunishi, A., Katoh, S. and Nishioka, M., "Bubble Formation in Flowing Liquid", The Canadian Journal of Chemical Engineering, Vol. 56, 669 – 672, 1978

Terasaka, K., Hieda, Y., and Tsuge, H., "SO<sub>2</sub> Bubble Formation at an Orifice Submerged in Water", *Journal of Chemical Engineering of Japan*, Vol. 32, No. 4, 472 – 479, 1999

Terasaka, K. and Tsuge, H., "BUBBLE FORMATION UNDER CONSTANT-FLOW CONDITIONS", *Chemical Engineering Science*, Vol. 48, 3417 – 3422, 1993

Tsuge, H., Hibino, S., and Nojima, U., "Volume of a bubble formed at a single submerged orifice in a flowing liquid", *International Chemical Engineering*, Vol. 21, No. 4, 630 - 636, 1981

Tsuge, Hideki, Terasaka, Koichi, Koshida, Wataru, and Matsue, Hirokazu, "Bubble formation at submerged nozzles for small gas flow rate under low gravity", *Chemical Engineering Science*, Vol. 52, No. 20, 3415 – 3420, 1997

Unkel, P. J., "THE STUDY OF OXYGEN TRANSPORT FROM MICRO-BUBBLES IN 0.9% SALINE", Master Thesis in Louisiana Tech University, November, 1991

Weinberger, S. E., *Principles of Pulmonary Medicine*. Philadelphia, Saunders, 1992

White, F. M., *Viscous Fluid Flow*, Second Edition, McGraw-Hill, 1991

Yoo, Dong-Hyun, Terasaka, Koichi, and Tsuge, Hideki, "Behavior of Bubble Formation at Elevated Pressure", *Journal of Chemical Engineering of Japan*, Vol. 31, No. 1, 76 – 82, 1998

Zapol Warren M., "Bolotrauma and the Intravenous Oxygenator in Patients with Adult Respiratory Distress Syndrome", *Anesthesiology*, Vol. 77, 847 – 849, 1992